UNIVERSITÉ DE GRENOBLE

THÈSE

Pour obtenir le grade de

DOCTEUR DE L'UNIVERSITÉ DE GRENOBLE

Spécialité : **Océan, Atmosphère, Hydrologie**

Arrêté ministériel : 7 août 2006

Présentée par

Nan YU

Thèse dirigée par **Guy DELRIEU** et **Brice BOUDEVILLAIN**

préparée au sein du **Laboratoire d'étude des Transferts en Hydrologie et Environnement (LTHE)**
dans **l'École Doctorale «Terre, Univers, Environnement»**

Précipitations méditerranéennes intenses - caractérisation microphysique et dynamique dans l'atmosphère et impacts au sol

Thèse soutenue publiquement le **2 mai 2012**,
devant le jury composé de :

M. Laurent BARTHES
Maître de Conférences, Université de Versailles-Saint-Quentin-en-Yvelines, France (Rapporteur)
M. Alexis BERNE
Professeur assistant, EPFL, Switzerland (Rapporteur)
M. Jean-Dominique CREUTIN
Directeur de Recherche, CNRS, France (Président)
M. Remko UIJLENHOET
Professeur, Université de Wageningen, Pays-Bas (Membre)
M. Guy DELRIEU
Directeur de Recherche, CNRS, France (Membre)
M. Brice BOUDEVILLAIN
Physicien-adjoint, CNAP, France (Membre)

Université Joseph Fourier / Université Pierre Mendès France / Université Stendhal / Université de Savoie / Grenoble INP

Intense Mediterranean precipitation

- Microphysical and dynamic characteristics of rainfall in the atmosphere and its impacts on soil surface erosion

A Thesis

presented to

The Earth, Space and Environmental Sciences Doctoral School

by

Nan YU

In Partial Fulfillment

Of the Requirements for the Degree

Doctor of Philosophy in Ocean, Atmosphere and Hydrology Science

UNIVERSITY OF JOSEPH FOURIER (GRENOBLE 1)

May 2012

Intense Mediterranean precipitation

- Microphysical and dynamic characteristics of rainfall in the atmosphere and its impacts on soil surface erosion

Approved:

Jean-Dominique CREUTIN, Chairman

Laurent BARTHES

Alexis BERNE

Remko UIJLENHOET

Guy DELRIEU, Advisor

Brice BOUDEVILLAIN, Co-Advisor

Date Approved: 2 May 2012

Résumé

Cette étude propose une unification des formulations mono- et multi-moments de la distribution granulométrique des pluies (DSD pour « drop size distribution ») proposées dans la littérature dans le cadre des techniques de mise à l'échelle (scaling). On considère dans un premier temps que la DSD normalisée par la concentration en gouttes (Nt, moment d'ordre 0 de la DSD) peut s'écrire comme une fonction de densité de probabilité (*ddp*) du diamètre normalisé par un diamètre caractéristique (*Dc*). Cette ddp, notée *g(x)* avec *x=D/Dc*, aussi appelé distribution générale, semble être bien représentée par une loi gamma à deux paramètres. Le choix d'un diamètre caractéristique particulier, le rapport des moments d'ordre 4 et 3, conduit à une relation d'auto-consistance entre les paramètres de la fonction *g(x).* Deux méthodes différentes, fondées sur 3 moments particuliers de la DSD (*M0, M3* et *M4*) ou bien sur des moments multiples (de *M0* à *M6*) sont proposées pour l'estimation des paramètres et ensuite évaluées sur 3 ans d'observations de DSD recueillies à Alès dans le cadre de l'Observatoire Hydrométéorologique Méditerranéen Cévennes-Vivarais (OHMCV). Les résultats révèlent que: 1) les deux méthodes d'estimation des paramètres ont des performances équivalentes; 2) malgré la normalisation, une grande variabilité de la DSD est toujours observée dans le jeu de données mis à l'échelle. Ce dernier point semble résulter de la diversité des processus micro-physiques qui conditionnent la forme de la DSD.

Cette formulation est ensuite adaptée pour une mise à l'échelle avec un ou deux moments de la DSD en introduisant des modèles en loi puissance entre des moments dits de référence (par exemple l'intensité de la pluie *R* et / ou le facteur de réflectivité radar *Z*) et les moments expliqués (concentration en gouttes *Nt*, diamètre caractéristique *Dc*). Par rapport aux formulations antérieures présentées dans la littérature, notre approche tient compte explicitement des préfacteurs des modèles en loi puissance pour produire une distribution uniforme et sans dimension, quel(s) que soit le(s) moment(s) de référence pris en considération. De manière analogue à la première partie du travail, deux méthodes fondées sur 1) l'établissement de modèles en loi de puissance ou 2) l'utilisation de moments multiples (de *M0* à *M6*), sont proposées pour estimer des paramètres climatologiques des DSD mises à l'échelle par un ou deux DSD moment(s). Dans les deux cas, il est tenu compte des relations d'auto-consistance résultant du fait que la DSD dépend du ou des moments(s) de référence qui est(sont) fonction lui(eux)-même(s) de la DSD. Les

résultats montrent que: 1) la méthode d'estimation a un impact significatif pour la formulation de mise à l'échelle par un seul moment; 2) le choix du moment de référence dépend des objectifs d'étude: par exemple, le modèle mis à l'échelle par des moments d'ordre élevé produit une bonne performance pour les grosses gouttes mais pas pour les petites; 3) l'utilisation de deux moments au lieu d'un seul améliore significativement la performance du modèle pour représenter les DSD.

Le modèle de mise à l'échelle de la DSD est ensuite appliqué pour analyser la variabilité inter- événementielle selon trois paramètres (*Nt*, *Dc* et μ, ce dernier paramètre μ décrivant la forme de la fonction gamma). Différentes séquences de pluie ont été identifiées de façon subjective pour l'événement pluvieux intense des 21-22 octobre 2008 par des changements brusques des moments et/ou paramètres dans les séries temporelles correspondantes. Ces phases de pluie sont liées à des processus météorologiques différents. Une relation préliminaire est établie entre les observations radar et la variation des paramètres des DSD au sol telle que mesurée par le disdromètre. Les formulations de mise à l'échelle sont également appliquées pour des estimations des densités de flux d'énergie cinétique des précipitations à partir de l'intensité de la pluie et / ou de la réflectivité radar. Les résultats confirment que l'utilisation de deux moments (*R* et *Z*) améliore significativement les performances de ces modèles, malgré les caractéristiques d'échantillonnage très différentes des radars et des pluviomètres. Cette application ouvre des perspectives intéressantes pour la spatialisation de l'énergie cinétique des pluies dans le cadre des études sur le pouvoir érosif des pluies.

摘要

本篇论文综合了过去文献中的尺度分析法，为“一矩量”和“双矩量”雨滴谱分布模拟提出了一个通用模型。首先，我们将雨滴谱的雨滴个数除于它的**总雨滴数**，然后雨滴直径除于这个雨滴谱的**特征直径**（在本文中，特征直径被定义为第四和第三雨滴谱矩量之商）。这样我们就能得到一个尺度化的雨滴谱。我们发现包含两个参数的伽马概率分布模型可以被用来很好地模拟这个尺度化的雨滴谱，而且这两个参数并不相互独立。因此，我们只需要估计其中一个参数，然后通过自回归关系式便能得出另一个参数的数值。在本文中，我们提出了两种不同的参数估计方法。第一种方法使用了三个雨滴谱矩量（第零，第三和第四矩量），第二种方法使用了所有雨滴谱矩量（从第零到第六矩量）。为了验证我们的雨滴谱尺度化模型和相关的参数估计方法，在 Cévennes-Vivarais 地中海气象水文观测实验中观测到的，大约三年的雨滴谱数据被用来检验模型。我们得到以下结果：1）两种参数估计方法给出的模型结果非常近似；2）经过**总雨滴数**和雨滴谱**特征直径尺**度化后的雨滴谱，仍然具有很大的变异性。

本文的第二部分阐述了如何将雨滴尺度化模型推广到任意 “一矩量”和“双矩量”雨滴谱模型。为此，我们使用了幂函数关系式将已知的矩量和**总雨滴数**，**特征直径**联系起来。比较过去文献中提出的独立的雨滴谱矩量模型，我们的“一矩量”和“双矩量”模型都建立在相同的，无量纲的尺度化雨滴谱上，并考虑到了幂函数关系中的系数项。因此，无论我们选择任何矩量来模拟雨滴谱，我们都可以使用这个通用的尺度化雨滴模型。为了得到一个气候性的 “一矩量” 和 “双矩量” 雨滴谱模型，我们提出了两种参数估计方法来估计模型中的参数。第一种方法建立在幂函数关系式的回归分析上，第二种使用了所有的矩量观测值（从第零到第六矩量）。结果表明，1）在 “一矩量” 雨滴谱模型中，上述两种估计方法得出的模型有很大的不同； 2）雨滴谱矩量的选择很大程度上取决于我们研究的目的，例如， 高次的矩量模型对大雨滴数量模拟效果较好，但对小雨滴数量模拟比较差； 3）“双矩量”雨滴谱模型比“一矩量” 模型能更好的模拟真实的雨滴谱分布。

在应用方面，我们利用尺度化雨滴谱模型来分析短时间尺度内的降雨变化。我们发现根据**总雨滴数**，雨滴谱的**特征直径**和**伽马密度函数中的参数**，可以将一场降雨划分为不同的时段。同时我们初步讨论了以上降雨变量和雷达观测数据之间的关系。

另外，我们利用在第二部分得到的气候矩量雨滴谱模型，根据实际雷达和/或雨

量计的观测结果来重建雨滴谱，并且估计雨滴的动能密度流。结果表明，尽管雷达和雨量计的采样尺度非常之不同，但联合采用雷达和雨量计的观测值对雨滴谱重建和雨滴的动能密流度估计均优于单独使用雷达或雨量计的估计结果。

Abstract

This study offers a unified formulation for the single- and multi-moment raindrop size distributions (DSD), which were proposed in the framework of scaling analysis in the literature. The key point is to consider the DSD scaled by drop concentration (N_t, 0^{th} order DSD moment), as a probability density function (*pdf*) of raindrop diameter scaled by a characteristic diameter (D/D_c). The D_c is defined as the ratio of the 4^{th} to the 3^{rd} DSD moment. A two-parameter gamma *pdf* model, with a self-consistency relationship, is found to be suitable for representing the scaling DSD formulation. For the purpose of parameter estimation, two different methods, based on three DSD moments (0^{th}, 3^{rd} and 4^{th} moments) and multiple DSD moments (from 0^{th} to 6^{th} moments), are proposed and then evaluated through the 3-year DSD observations, collected at Alès within the activities of the Cévennes-Vivarais Mediterranean Hydrometeorological Observatory (CVMHO). The results reveal that: 1) the scaled DSD model parameterized by three moments (0^{th}, 3^{rd} and 4^{th} moments) possesses a similar performance compared to that constructed by multiple DSD moments; 2) regardless the application of scaling technique, large variation is still exhibited in the climatological scaled DSD dataset.

The scaled DSD formulation is, in a second step, adapted to the one- and two-moment scaling DSD formulations by introducing single and dual power-law models between the reference moments (e.g. rain rate R and/or radar reflectivity factor Z) and the explained moments (total concentration N_t, characteristic diameter M_4/M_3). Compared with previous DSD formulations presented in the literature, the presented approach explicitly accounts for the prefactors of the power-law models to produce a uniform and dimensionless scaled distribution, whatever the reference moment(s)

considered. In the same manner, two methods based on 1) single or dual power-law models and 2) multiple DSD moments (from 0^{th} to 6^{th} moments), are proposed to estimate the climatological parameters in the one- and two-moment scaling DSD formulations. The results show that: 1) the estimation method has a significant impact on the climatological DSD formulation scaled by one moment; 2) the choice of the reference moment to scale DSD depends on the objectives of the research: e.g. the DSD model scaled by high order moment produces a good performance for large drops at the cost of a poor performance for the small ones; 3) using two scaling moments improves significantly the model performance to represent the natural DSD, compared to the one-moment DSD formulation.

In terms of applications of scaling DSD model, the analysis of the inter-event variability is performed on the basis of the scaling formulation containing three parameters (N_t, D_c and μ describing the shape of the gamma function). Different rain phases can be identified by the sudden shifts of moments and parameters in time series. It is found that these rain phases are well linked to different weather processes. And a preliminary relationship is established between the radar observations and DSD parameters.

The climatological scaling DSD formulations are also used for the DSD reconstitutions and for rainfall kinetic energy flux density estimations by rain intensity and/or radar reflectivity factor. The results confirm that the application of two scaling moments (R and Z) improves significantly the performance of these models, regardless the different sampling characteristics between radar and raingauge.

To ...

My parents, who have offered me unconditional love and support since the beginning of my studies

Acknowledgements

Il m'est permis, au début de ce manuscrit, de remercier toutes les personnes m'ayant aidé pendant ces trois années. Qu'elles y trouvent ici toute l'expression de ma profonde gratitude.

Je tiens tout d'abord à remercier Guy Delrieu, Directeur de recherche au CNRS, qui m'a encadré tout au long de cette thèse et qui m'a fait partager ses avis d'expert sur le radar météorologique. Sans son expérience, ses conseils si riches et toujours si précis, sans sa gentillesse et sa disponibilité, cette thèse n'aurait pas vu le jour.

Mes remerciements vont conjointement à mon co-directeur de thèse Brice Boudevillain, pour avoir dirigé mes recherches aimablement et avec patience. Ses suggestions et aides précieuses sont indispensables pour l'aboutissement de ce travail.

Mes très sincères remerciements vont aussi à Laurent Barthès et Alexis Berne qui ont accepté la tâche de rapporteur de cette thèse. Je veux aussi remercier Jean-Dominique Creutin et Remko Uijlenhoet pour avoir accepté d'examiner ce travail et participer au Jury.

J'adresse tous mes remerciements à Thierry Lebel et à Sandrine Anquetin pour avoir accepté de m'accueillir dans l'équipe HMCI au sein de laboratoire LTHE. Je remercie aussi le ministère de l'enseignement supérieur et de la recherche qui a financé cette thèse en m'accordant un poste d'allocataire de recherche.

Il m'est également impossible d'oublier mes chers collègues de l'Université de Wageningen : Remko Uijlenhoet et Pieter Hazenberg. Tous les résultats présentés dans ce travail sont les fruits d'une collaboration avec eux.

Je tiens aussi à remercier tous les membres de l'équipe HMCI pour leur soutien scientifique mais aussi pour avoir réussi à créer une super ambiance au sein du laboratoire. Une spéciale dédicace à Cédric Legout et Thomas Grangeon dont les connaissances sur l'érosion de la pluie au m'ont été indispensables dans cette étude. Je souhaite évidement remercier les personnes extérieures: Olivier Caumont et Olivier Bousquet de Météo France qui ont répondu à mes questions scientifiques très rapidement; Pierre-Alain Ayral de l'Ecole des Mines d'Alès qui a assuré la maintenance du disdromètre.

Enfin merci à mes parents pour tout ce que je leur dois, et toutes les personnes que je n'ai pas citées ici. Merci bien pour vos soutiens désintéressés.

Contents

List of Figures

LIST OF FIGURES

List of Tables

GLOSSARY

ARAMIS	Application Radar à la Météorologie Infra-Synoptique
AROME	Application de la Recherche à l'Opérationnel à Méso-Échelle
CV	Coefficient of variation
CVMHO	Cévennes-Vivarais Mediterranean Hydro-meteorological Observatory
DSD	Raindrop size distribution
D_c	Characteristic diameter in mm
D_0	Mean diameter in mm
D_m	Mass-weighted mean diameter in mm
D	Drop diameter in mm
EUROSEM	European soil erosion model
$g(x)$	General scaling raindrop distribution
IPEX	Intermountain Precipitation Experiment
Kdp	Specific differential phase in deg/km
KE	Raindrop kinetic energy flux in $Jm^{-2}h^{-1}$
LTHE	Laboratoire d'étude des Transferts en Hydrologie et Environnement
LWC	Liquid water content in gm^{-3}
M_k	k^{th} order DSD moment in $mm^k m^{-3}$
MAP	Mesoscale Alpine Program
MEDDTL	Ministère de l'Ecologie, du Développement durable, des Transports et du Logement
N_t	Raindrop concentration in m^{-3}
$N(D)$	Distribution of the drop number as a function of diameter in $mm^{-1}m^{-3}$
PCA	Principal component analysis
PC_i	i^{th} principal component
pdf	Probability density function
r	Coefficient correlation
R	rain rate in mmh^{-1}
SDPRM	Sous-Direction de la Prévention des Risques Majeurs
S	Total surface area of raindrops in mm^2m^{-3}
TRMM	Tropical Rainfall Measuring Mission
TOGA COARE	Tropical Ocean Global Atmosphere Coupled Ocean-Atmosphere Response Experiment
V	Total volume of raindrops in mm^3m^{-3}
v	Drops vertical velocity in ms^{-1}
WEPP	Water erosion prediction project
Z	Reflectivity factor in mm^6m^{-3}
Zdr	Differential reflectivity in dB
ρ	Density of water in kgm^{-3}
ρ_{hv}	Polarmetric correlation coefficient
Λ	Radar wavelengths in cm

Chapter 1

Introduction

Water is one of the most precious natural resources for the development of human society. But sometimes, the excessive water causes also serious damages to humanity and civilization. Rain, which deposits most of the fresh water on the Earth's surface, has been studied since the dawn of humanity. However, the complexity of micro-structure of rainfall is still a challenge to improve our understanding and prediction of hydrological disasters. This thesis deals with the heavy rainfall, or more precisely, the microphysical and dynamic characteristics of intense rainfall in the Cévennes-Vivarais region, which is located in the southeast of France. The general scientific context and motivation of this study are presented in this first chapter.

1.1 The Cévennes-Vivarais region

1.1.1 Description of the Cévennes-Vivarais region

The word Cévennes refers to a range of successive mountains which run from southwest (Montagne Noire) to northeast (Monts du Vivarais) in the south of France. These mountains are a part of the Massif Central and covers parts of the French administrative departments of Ardèche, Lozère, Haute-Loire, Gard, Hérault. The highest point is Mont Lozère (1702 m). Another notable peak in this region is the Mont Aigoual (1567 m) where the French Rivers Authority and Forestry Commission built a meteorological observatory in 1887.

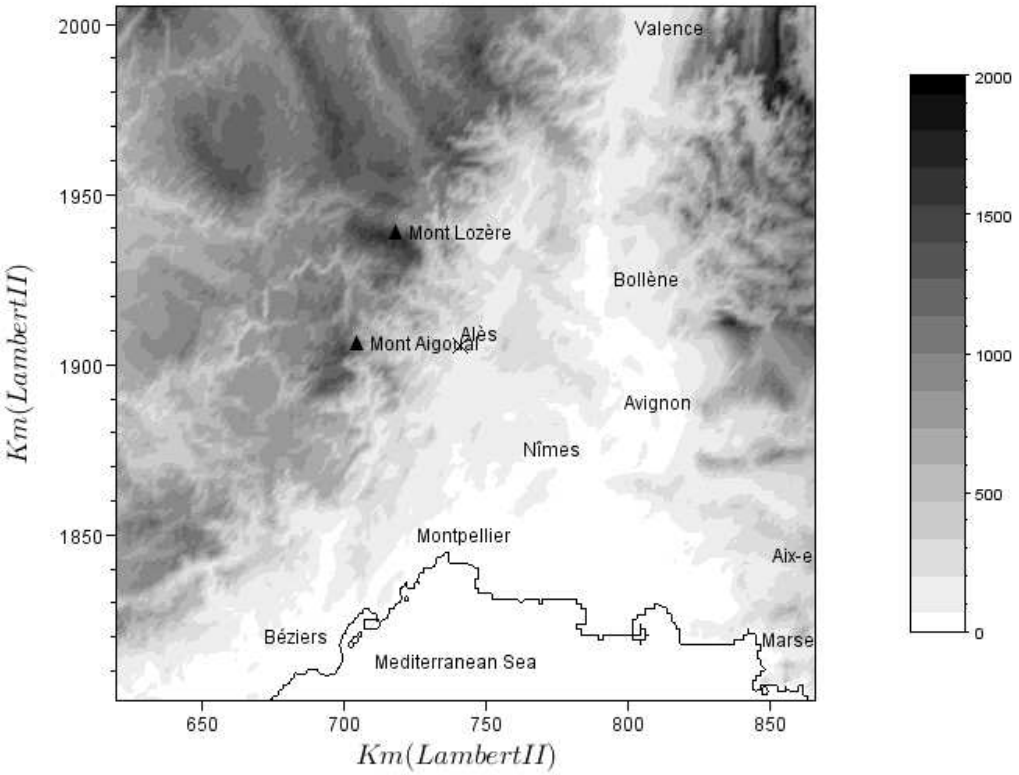

Figure 1.1: Topographic map of the Cévennes-Vivarais region in Southern France. - The figure shows the topography of the Cévennes-Vivarais region in the Lambert-2 projection.

The Cévennes-Vivarais region defined in our study is showed in Fig.1.1. It includes some steep mountains with narrow valleys. The altitude can vary from sea level up to 1500 m over roughly 30 km. Godart et al. (2009) identified this region into three sectors: a lower terrace (altitude below 200 m); a hilly sector (altitude between 200 and 500 m) and a mountainous sector (altitude above 500 m).

The location of the Cévennes-Vivarais region and its orographic feature are extremely favorable for heavy rainfall events. Especially in autumn, the temperature of the Mediterranean Sea is still high, while the cold air masses originating in high latitudes begin to move toward low latitudes. The transfer of heat and moisture from the Mediterranean Sea colliding with northern cold air creates favorable conditions for heavy precipitation (Nuissier et al., 2008). The orography which lifts the airflow plays an important role to generate and trigger the convective cells as well. All these conditions lead to heavy Mediterranean rainfall (Smith, 1979) occurring regularly in the Cévennes-Vivarais region, which also gives its name, in French, to the meteorological and orographic effect for the intense precipitation, called "épisodes cévenols".

1.1.2 Flooding vulnerability

According to the climatological rainfall database of Météo-France (Fig.1.2.), the Cévennes-Vivarais is one of the regions most affected by heavy rainfall events in France. The heavy amount of precipitation, with the steep topography, leads often to flash floods over small watershed. The rapid rise of the water level in rivers, with little or no advanced warning, causes major damages to human lives and property. The Ministry of Ecology, Sustainable Development, Transport and Housing (MEDDTL) reported 135 natural disasters that occurred in France between 1900 and 2010. There were 70 events associated with flood disasters, among which 41 occurred in the south of France. Detailed information for eight serious flood disasters is selected in Table.1.1.

One of the most severe floods in the Cévennes-Vivarais region occurred on 8 and 9 September 2002. An intense thunderstorm dumped more than 300 mm rain in the department Gard during 48 hours. The maximum daily rainfall recorded by the rain-gauge reached to 687 mm. 24 people were killed during the disaster and the economic damage was estimated at 1.2 billion € (Huet et al., 2003).

For the purpose of a better understanding of the intense Mediterranean precipitation, the current thesis on ≪microphysical and dynamic characteristics of rainfall in the

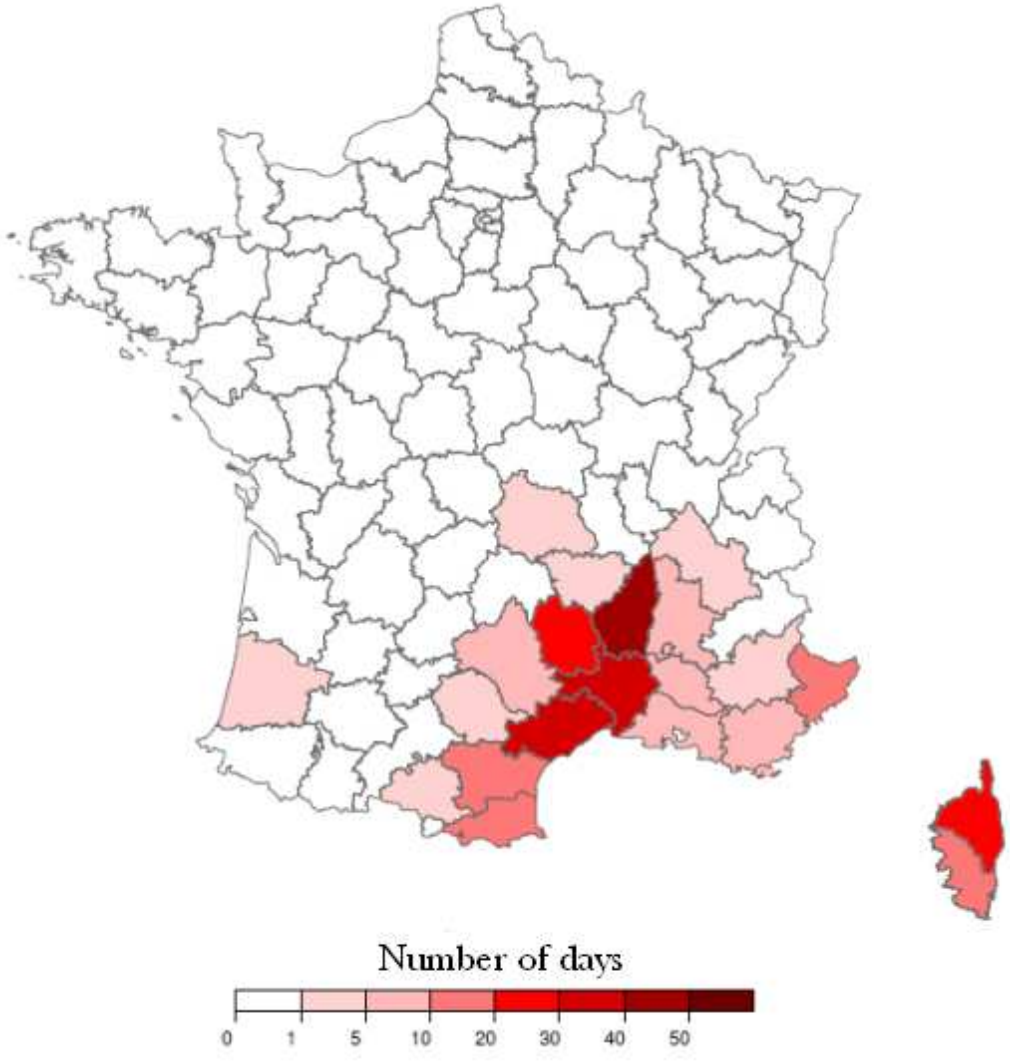

Figure 1.2: Number of heavy rain days during the recent 30 years (1979-2008) for each French department. - The heavy rainy days is defined by the daily precipitation higher than 200 mm. Météo-France (2009) http://pluiesextremes.meteo.fr

Date	Department	Meteorological comments	Socio-economic impacts
20 and 21 September 1890	Gard, Lozère	828 mm rain measured during 24 hours at the foot of Mont Aigoual	28 bridges damaged in Ardèche, about 50 deaths
28 and 29 September 1900	Gard, Hérault	950 mm rain measured during 10 hours at the foot of Mont Aigoual	No reference
Autumn 1958	Gard, Hérault, Ardèche, Vaucluse	2 successive events. Each event produced 200 to 300 mm rain during 24 hours	35 deaths in Gard
1 to 5 November 1963	Ardèche, Lozère, Gard	832 mm rain observed at Mont-Aigoual	1 death
6 to 8 November 1982	Languedoc-Roussillon, PACA et Corse	300 to 400 mm in Gard, more than 500 mm in Cévennes region	13 deaths, 0.3 billion € of damages
3 October 1988	Gard	420 mm rain observed at Nîmes	10 deaths, 0.5 billion € of damages
21 September 1992	Gard, Hérault, Ardèche, Drôme	300 mm rain observed in Gard	47 deaths, 0.5 billion € of damages
8 and 9 September 2002	Gard, Hérault, Vaucluse, Lozère	More than 300 mm rain measured in Gard	419 "communes" are affected by the flood, causing 24 deaths and 1.2 billion € of damages

Table 1.1: Recent flooding disasters occurred in Cévennes-Vivarais region. - (SDPRM 2007, http://www.prim.net/).

atmosphere and its impacts on soil surface erosion≫ was proposed by LTHE (Laboratoire d'étude des Transferts en Hydrologie et Environnement) at the end of 2008. This document is aimed to present the main research and findings of this study.

1.2 Microstructure of rain

1.2.1 Raindrop size distribution (DSD)

Above the Earth's surface, the concentration of atmospheric water vapor into drops makes it heavy enough to fall under gravity. The amount of rainfall has a dramatic effect on agriculture and water resources management. The first known records of rainfalls were kept by the Ancient Greeks about 500 Before Christ. These records were then used as a basis for land taxes. Today, the quantity of rainfall becomes a standard meteorological observation defined by the World Meteorological Organization.

However, the quantity of water fallen from the sky is not enough to describe total characteristics of rain. A detailed measurement should be focused on each raindrop. For the same quantity of rainfall, the rain can be composed of a large number of raindrops with small averaged drop size, or a few raindrops with large drop size. In order to obtain a detailed measurement, the raindrop size distribution (DSD) is proposed to quantify precisely the microstructure of rainfall. We denote the DSD by $N(D)$ $[mm^{-1}m^{-3}]$ which represents the number of raindrops per unit volume per unit size interval (D to $D + \Delta D$).

The measurement of $N(D)$ is important in meteorological research for two main reasons: 1) spatial and temporal variability of DSD reflects the physics of rain evolution processes; 2) the macroscopic rainfall quantities, such as rain rate (R), liquid water content (LWC) and radar reflectivity factor (Z) are directly related to the DSD. A fundamental variable in our study, named the DSD moment, is defined as,

$$M_k = \int_0^\infty N(D) D^k dD, \tag{1.1}$$

where M_k represents the k^{th} order of the DSD moment. Each macroscopic rainfall quantity (observation) is proportional to a particular DSD moment. The expressions of common macroscopic rainfall quantities based on the DSD are listed in Table.1.2.

Macroscopic rain property	**Symbol**	**Unit**	**Relationship**
Raindrop concentration	N_t	m^{-3}	M_0
Total surface area of raindrops	S	mm^2m^{-3}	πM_2
Total volume of raindrops	V	mm^3m^{-3}	$\pi M_3/6$
Liquid water content	LWC	gm^{-3}	$10^{-3}\pi M_3/6$
Radar reflectivity	Z	mm^6m^{-3}	M_6
Kinetic energy flux	KE	$Jm^{-2}h^{-1}$	$5.09 \times 10^{-2}M_5$
Rain rate	R	mmh^{-1}	$7.12 \times 10^{-3}M_{3.67}$

Table 1.2: Expressions of macroscopic rainfall quantities based on the DSD.

Note that the assumed relationship (Atlas and Ulbrich, 1977) between raindrop terminal fall speed (v in ms^{-1}) and raindrop diameter (D in mm)

$$v = 3.78D^{0.67} \tag{1.2}$$

is taken into account to derive the expressions of kinetic energy flux (KE) and rain rate (R). It is worth to mention that the raindrop fall velocity plays an important role in determining the disdrometer resolution volumes and the conversion of the rainfall flux variables, such as R and KE, into the state variables, such as $N(D)$ and Z (Salles and Creutin, 2003). It is generally assumed that the raindrops have reached their terminal velocities when they hit the ground. Previous theoretical and experimental studies showed that the terminal velocity can be expressed as a function of the drop diameter. Power-law and exponential model have been proposed to represent physically-based $v(D)$ models e.g. (Beard, 1976) or data-fitted models (Atlas and Ulbrich, 1977; Best, 1950; Gossard et al., 1992; Gunn and Kinzer, 1949). In addition, Erpul et al. (2002) showed that the vertical wind speed has significant effects on the raindrops velocity (updrafts, downdrafts). This would be a motivation for using measured velocities instead of a velocity model depending on the diameter. However, several authors (Jaffrain and Berne, 2011; Tokay et al., 2003) claimed that the DSD measurement device we have been using in this study (the Parsivel disdrometer) does not provide accurate velocity measurements; their results are consistent with our observations. In the present study,

we therefore use the well-known power-law model proposed by Atlas and Ulbrich (1977), which has been already considered in many previous studies, to calculate the terminal velocity of raindrops.

1.2.2 Parameterization of the DSD

The raindrop size distribution is a fundamental property to understand the rainfall because its variation reflects the physics of rain formation processes. In order to describe this distribution by several parameters, several authors have proposed in the past different mathematical expressions to parameterize the DSD. Marshall and Palmer (1948) proposed an exponential DSD model expressed in the form of

$$N(D) = N_0 exp(-\lambda D) \tag{1.3}$$

with two parameters N_0 and λ. Based on the experimental observations, the parameter N_0 was fixed and equal to 8000 $mm^{-1}m^{-3}$ and λ $[mm^{-1}]$ was linked to the rainfall intensity R $[mmh^{-1}]$ by $\lambda = 41R^{-0.21}$. Later, Waldvogel (1974) observed so-called "N_0 jumps" during some rain events and suggested that the variation in N_0 was related to the type of rainfall (convective and stratiform). Thanks to the development of instrumental technology, more accurate DSD measurements revealed that the exponential DSD model overestimated the number of small drops. Joss and Gori (1978); Liu (1993) found that the exponential model is merely a statistical average of many "instantaneous" size distributions. To better describe the DSD, a 3-parameter gamma DSD model was proposed by Ulbrich (1983) as

$$N(D) = N_0 D^{\mu} exp(-\lambda D), \tag{1.4}$$

where N_0 $[mm^{-1-\mu}m^{-3}]$, μ [-] and λ $[mm^{-1}]$ are the intercept, shape and slope parameters, respectively. This model allows additional flexibility for the DSD fit with respect to the exponential model, which is a special case of the gamma model with μ=0. Recent observations (Atlas et al., 2000; Tokay and Short, 1996) confirmed that the gamma function is a good approximation for the representing of natural DSD.

Although the gamma model generally provides good fits of observed DSDs, one of its drawbacks is associated with the units of N_0 which depends on the parameter μ. In addition, the three parameters of gamma function have no physical meanings: several authors have studied the relationships between pairs of parameters to reduce the

number of free parameters, e.g. Ulbrich (1983) displayed a linear relationship between $ln(N_0)$ and μ; Brandes et al. (2003); Chu and Su (2008); Zhang et al. (2003) carried out an investigations of a 2^{nd} order polynomial relationship between μ and λ. However, the physical meaning and the domain of validity of such relationships have been questioned by several authors (Chandrasekar and Bringi, 1987; Moisseev and Chandrasekar, 2007; Smith, 2009).

An alternative way to model DSDs is based on the concept of normalization. To our knowledge, Sekhon and Srivastava (1970) were the first authors proposing to normalize the exponential distribution and Willis (1984) further developed this concept for a gamma DSD model. The normalization concept refers to the scaling analysis which describes DSDs as a combination of one or several DSD moment(s) and a scaled distribution $g(x)$ of a normalized diameter x. This scaled distribution $g(x)$ is often named the "general distribution" in the literature, as it is supposed with less variability compared to the moment(s). The aim of the scaling analysis is to normalize the variability of the DSD by the moment(s). Consequently the general distribution ($g(x)$) remains stable, or at least, independent to the scaled moment(s). Sempere Torres et al. (1994) proposed a one-moment normalization procedure, with:

$$N(D) = M_i^{\alpha_i} g(x) \quad with \quad x = DM_i^{-\beta_i}, \tag{1.5}$$

where α_i and β_i are two parameters and M_i is the i^{th} moment of the DSD. Sempere Torres et al. (1994) argued that most of the previously published DSD models could be considered as particular cases of such a formulation. However, Sempere Torres et al. (1998) found that the variability of the general distribution remains significant and seems to depend on the type of rain (convective or stratiform) and the geographic location as well. To better constrain the general distribution, various authors introduced a second moment into the normalization procedure. For instance, Illingworth and Blackman (2002) and Testud et al. (2001) developed normalization formulations with respect to liquid water content (LWC) and a mean volume diameter defined as the ratio of the 4^{th} to the 3^{rd} moments of the DSD. A further clarification was proposed by Lee et al. (2004), who reviewed previous works and formulate an approach to normalize DSDs by any pair of two moments M_i and M_j as:

$$N(D) = M_i^{(j+1)/(j-i)} M_j^{(i+1)/(i-j)} g(x) \quad with \quad x = DM_i^{1/(j-i)} M_j^{-1/(j-i)}. \tag{1.6}$$

It is noteworthy that the exponents in this 2-moment formulation are strictly defined by the order i and j of the chosen scaling moments.

Both $g(x)$ functions in (1.5) and (1.6) are called the general distribution. But one may note that the prefactor $M_i^{\alpha_i}$ and the argument $DM_i^{-\beta_i}$ of the $g(x)$ function in (1.5) have unpractical units of $[L]^{\alpha(i-3)}$ and $[L]^{1+\beta(i-3)}$, respectively (L stands for a length scale). Even if (1.6) is more satisfactory from the point of view of units, its numerical values indeed depend on the order of the scaled moments. This leads to different and "non-universal" general distributions which depend on the order of the scaled moment(s) and prevents the comparison of the $g(x)$ functions established by different moments in the one- or two-moment normalization frameworks. Therefore some work still needs to be done to cope with these problems and to harmonize the single- and two-moment normalization frameworks.

1.2.3 Evolution of the DSD and microphysics processes

A better understanding of the DSD, or the parameters in the DSD formulation, is essential to gain the knowledge of physical processes of rainfall. The characteristic of a drop size distribution depend on many factors, e.g. meteorological conditions, orographic condition and various microphysical processes. In this subsection, we will present an overview of influences of physics and environmental conditions on the DSD.

Precipitation is generally considered to be of two clearly distinguishable types–stratiform and convective (Houze, 1993). The major difference between them is the vertical air velocity. Within convective rain clouds, the vertical air velocity has the same order of magnitude as the horizontal air velocity, as compared to the stratiform clouds which are composed of broader layers of slowly rising air. Convective clouds are often associated with severe, short-duration weather phenomena, such as thunderstorm, heavy rain, snow shower and hail, whereas the light, widespread rain is generally produced by stratiform clouds.

Stratiform raindrops are principally generated by the melting snowflakes, the graupel and the rimed particles in the melting layer. A layer of enhanced radar reflectivity near the 0 °C melting layer (hereafter referred to as the bright band) within stratiform clouds is usually observed by weather radar (Browne and Robinson, 1952; Hooper and Kippax, 1950). This bright band is associated with the ice particles or snow flakes

enclosed by liquid water producing high reflectivity echoes. From a microphysical perspective, a strong bright band reflects melting of large, low density and dry snowflakes into relatively larger raindrops whereas a weak bright band reflects melting of tiny, compact graupel or rimed snow particles (Fabry and Zawadzki, 1995).

Regarding convective rainfall, the heavy precipitation is typically produced by two mechanisms: 1) the riming of ice crystals falling back through the super cooled water in the updraft and 2) the collection of cloud water by raindrops. The second process is dominant during the early stages of convection development while the first one is more important during the later convective development stage (Li et al., 2002). Several studies showed that riming in the updraft region is the main process determining the form of the DSD in convective clouds, and aggregation is the most important process in stratiform DSD formation (Atlas and Ulbrich, 2000; Gamache, 1990).

Each microphysical process has a different influence on the DSD measured on the surface of the Earth. Waldvogel (1974) modeled the DSD by the exponential distribution (1.3) and discovered that the sudden decrease of N_0 indicates the transition of rainfall type from convective to stratiform. Other studies (Martner et al., 2008; Tokay and Short, 1996) confirmed that the stratiform rainfall is characterized, for a given rainrate, by less small drops and more large drops, as compared to the convective rain. This property may be explained by the aggregation process producing large drops within or under the melting layer in stratiform clouds, while the heavy riming process generates small raindrops in convective clouds (Waldvogel et al., 1993). However, one should pay attention to the fact that such argument is derived from the comparison of convective and stratiform rain at a similar rain rate. Some large drops which exceed 2 to 3 mm in diameter are also observed in tropical intense thunderstorms (Willis, 1984; Willis and Tattelman, 1989). For weak precipitation, Johnson et al. (1986) and Beard et al. (1986) showed the existence of large raindrops as well. They supposed that the large drops are generated by i) the large aerosol particles acting as nuclei (Johnson, 1982) and ii) the re-circulation of the small raindrops from the edge of the downdrafts into updrafts with large numbers of cloud drops (Rauber et al., 1991).

The investigation of squall-lines has been highlighted by several studies because they contain the stratiform and convective rain clouds at the same time. Maki et al. (2001) investigated tropical continental squall-lines based on a gamma DSD model (1.4)

and found that the convex upward shape of DSD for the convective rain and more exponential for the stratiform rainfall. Another squall-line system in northern Mississippi was studied by Uijlenhoet et al. (2003b) who showed that the leading convective line is characterized by large raindrop concentrations, large mean raindrop sizes and wide raindrop size distributions as compared to the following stratiform squall-line region.

Besides the convective and stratiform precipitation, the orographic precipitation is a third type of rainfall generated by a forced upward movement of air confronting by mountains. Ideally, a drizzle with large drops concentrations will be dominant at top of the precipitated cloud. The drizzle continues to coalesce with other drizzle and cloud drops into raindrops along the fall distance from the cloud top. For the shallow orographic clouds, the main variation in the DSD is associated to the evolution of the drops concentration, while the change of the mean drops size is bounded by the limited vertical fall distance along which they can grow (Rosenfeld and Ulbrich, 2003). It should be noted that the orographic rainfall is not totally independent to the convective and stratiform classification. The terms of stratiform orographic precipitation was used by Pradier et al. (2004). And Smith (1979) suggested the orographic effects on the airflow can generate the very active convective cells. Recent observation programs, such as the Intermountain Precipitation Experiment (IPEX; Schultz et al. (2002)) and the Mesoscale Alpine Program (MAP; Bougeault and Coauthors (2001)), were carried out in order to understand the microphysical growth processes of precipitation. With Doppler and polarimetic radar, Pujol et al. (2005) highlighted the contribution of the ice phase to heavy precipitation during a particular orographic rain event in the Alps (MAP IOP3). Therefore, it seems difficult to summarize a general DSD feature for the orographic precipitations due to the presence of various different microphysical processes and local surface properties (mountain elevation, slope, vegetation, lakes etc.)

A further way to categorize rain clouds is done by distinguishing their maritime or continental origin. The maritime rain is usually associated with the warm rain processes, for which the accretion and coalescence are dominant, whereas the continental rain originate mainly in ice processes. Rosenfeld and Lensky (1998) used the observation data during TRMM (Tropical Rainfall Measuring Mission) to retrieve the different microstructure between the maritime and continental rains. They found that two types of DSD are well separated with continental clouds producing greater concentrations of

large drops and small concentrations of small drops, compared to maritime rainfalls. Rosenfeld and Ulbrich (2003) explain the large drops in the continental rainfall by the presence of the ice hydrometeors which can grow indefinitely without breakup in the cold rain process.

Although numerous studies dealing with the rainfall classification and DSD have been carried out, it seems difficult to conclude about unique and general DSD characteristics for a particular type of rainfall (convective, stratiform, orographic etc...). Chapon et al. (2008) showed the abrupt changes and the stability for several hours of the scaled DSD within one rain event (Fig.1.3), and highlighted the importance of the intra-event DSD variability.

In the same manner, Lee and Zawadzki (2005) analyzed the DSD variability at different scales (climatological, daily, within one day, between physical processes and within a physical process). Their work showed that the DSD variability is more the result of complex dynamic, thermodynamic and microphysical processes within rainfall systems, which can hardly be reduced to a simple convective-stratiform classification. Hence the character of the DSD should be better associated to each particular microphysical process, rather than to the type of rain.

Rosenfeld and Ulbrich (2003) illustrated each microphysical process with its influence on the gamma DSD (1.4 1.5) in schematic diagrams. The following discussion is a summary of their works.

- Coalescence (Fig.1.4 a)
  decreases the numbers of small drops and total number concentration
  increases the numbers of large drops and averaged diameter
  increases the shape parameter μ as a function of the coalescence process

- Break-up (Fig.1.4 b) decreases the numbers of large drops and averaged diameter
  increases the numbers of small drops and the total number concentration decreases
  slightly the shape parameter μ

- Coalescence and break-up combined (Fig.1.4 c) break-up for large drops, coalescence for small drops both processes acting together increase μ substantially

- Accretion (Fig.1.4 d) increases the sizes of all particles without increasing their numbers

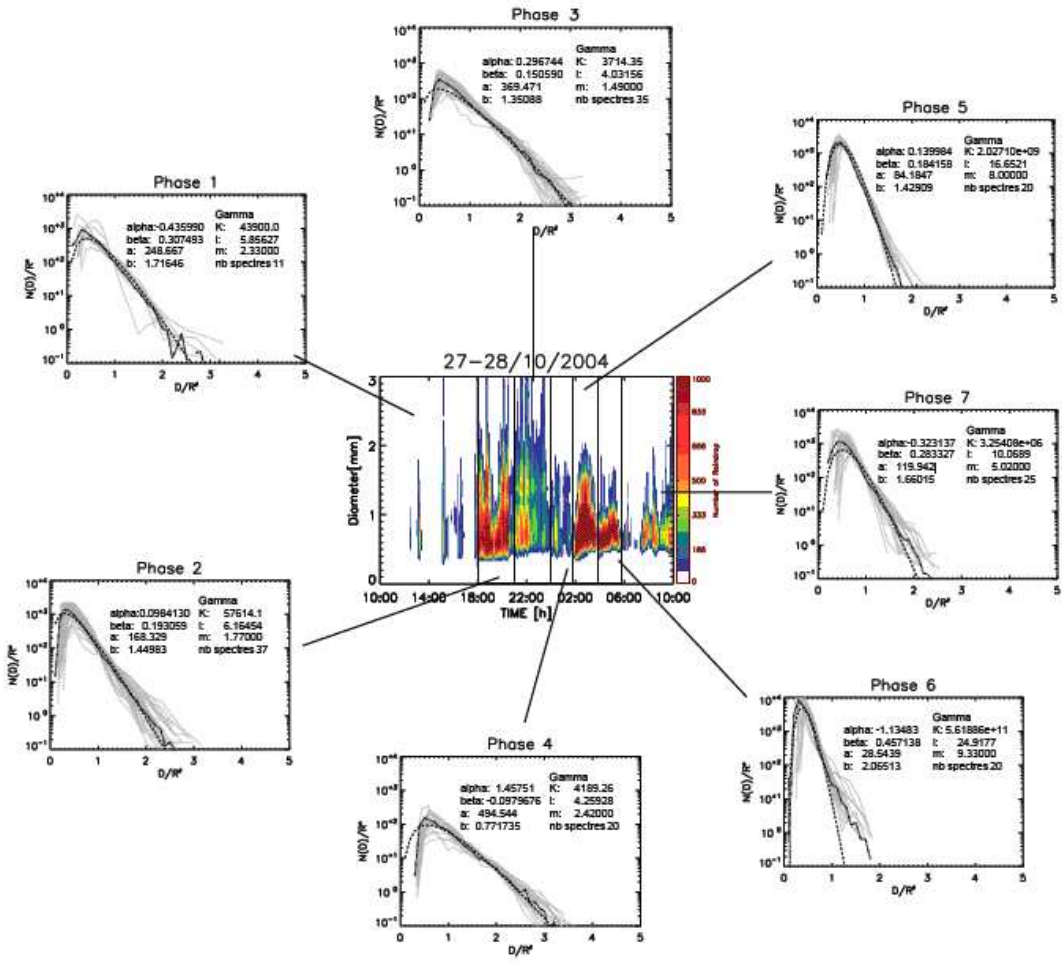

Figure 1.3: Intra-variability of the DSD within one rain event. - The figure illustrates the evolution of the DSD associated with scaled distribution within 7 rain phases (Chapon et al., 2008).

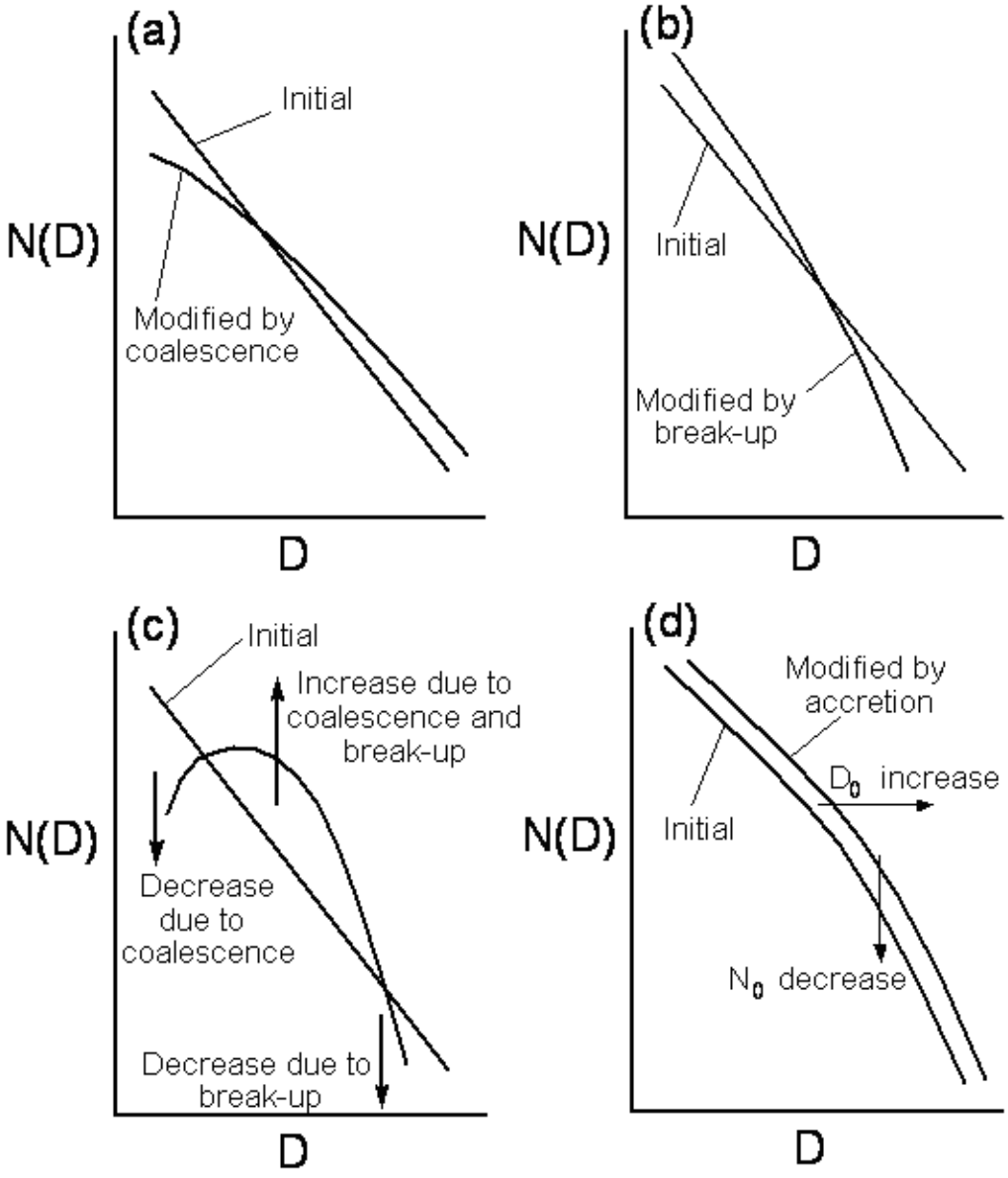

Figure 1.4: Schematic diagrams illustrating the effects on the raindrop size distribution 1. - The diagram illustrates the (a) raindrop coalescence, (b) raindrop break-up, (c) coalescence and break-up acting simultaneously and (d) accretion of cloud droplets (Rosenfeld and Ulbrich, 2003).

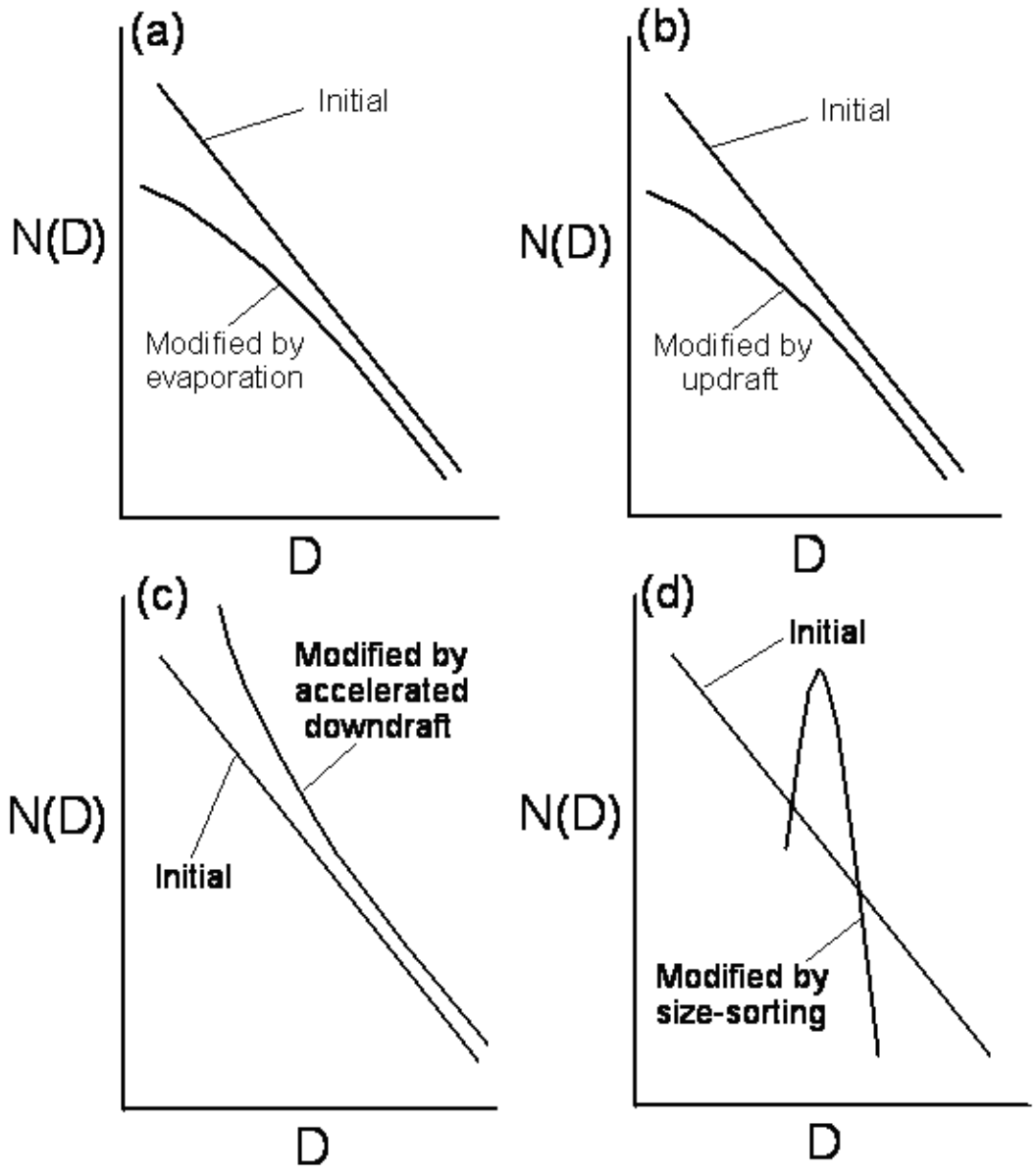

Figure 1.5: Schematic diagrams illustrating the effects on the raindrop size distribution 2. - The diagram illustrates the (a) evaporation, (b) updraft, (c) accelerated downdraft and (d) size-sorting (Rosenfeld and Ulbrich, 2003).

- Evaporation (Fig.1.5 a) decrease the number of small drops, increase the shape parameter μ
- Updraft (Fig.1.5 b) eliminates the smallest drops at the lower levels produces similar effects to the evaporation on the DSD
- Downdraft (Fig.1.5 c) yields complex influence on the DSD, as an example showed in (Fig.1.5 c).
- Size-sorting (Fig.1.5 d) makes the DSD narrower and decrease the total concentration of drops.

Each microphysical process leaves a particular signal in the DSD on the assumption that everything else is held constant. However, one should note that, in reality, the variability of the DSD is controlled by the combination of several processes together, which makes it difficult to understand the spatial-temporal behavior of the DSD.

1.2.4 Relationships among the DSD moments

Since the first application of radar in the meteorological field, intense scientific efforts have focused on rainfall estimation. Meteorological radar reflectivity factor (Z) provides potentially widespread rainfall data (R) with high temporal and spatial resolution, which is essential for meteorological and hydrological research. The radar reflectivity factor (Z) and rain intensity (R) obey a power-law relationship, often called Z-R relationship

$$Z = aR^b \tag{1.7}$$

In fact, the Z-R relationship is a particular case of the moment relationship which links the i^{th} to the j^{th} DSD moment. Depending on the DSD formulation, different moment relationship can be established. For example, based on the exponential DSD model (1.3), two general moment relationships are derived by eliminating N_0 or λ, respectively, as:

$$M_i = \frac{\Gamma(i+1)}{\Gamma(j+1)}\lambda^{j-i}M_j = 140.35\frac{\Gamma(i+1)}{\Gamma(4.67)}\lambda^{3.67-i}R \tag{1.8}$$

$$M_i = \frac{N_0\Gamma(i+1)}{[N_0\Gamma(j+1)]^{(i+1)/(j+1)}}M_j^{\frac{i+1}{j+1}} = \frac{N_0\Gamma(7)}{[N_0\Gamma(4.67)]^{(i+1)/4.67}}(140.35R)^{\frac{i+1}{4.67}} \tag{1.9}$$

The distinction between the linear moment relationship (1.8) and the power-law relationship (1.10) is a result of the dependence between the moment M_j and the parameters in DSD model (1.3). Marshall and Palmer (1948) discovered a strong power-law relationship ($\lambda = 4.1R^{-0.21}$) between the rain intensity (R) and the parameter λ. Considering their propositions: $\lambda = 4.1R^{-0.21}$ or $N_0 = 8000mm^{-1}m^{-3}$, we obtain two Z-R relationships as

$$Z = 255R^{1.5}, \tag{1.10}$$

$$Z = 237R^{1.5}. \tag{1.11}$$

One may note that, in these two cases, the exponents of the Z-R relationship are equal to 1.5. Only the prefactor is linked to the variation in the DSD. The gamma DSD model (1.4) provides further flexibility for the DSD adjustment at the cost of an additional form parameter μ which can be used to explain the variability of the exponent in the Z-R relationships. The moment relationships based on the modified gamma model was investigated by Steiner et al. (2004). In the same manner as the exponential model, the different dependence of the parameters yields different form of Z-R relationships. They distinguished three typical rainfall situations: 1) a linear Z-R relationship for the number controlled situation which suggests that the mean drop size (D_0) and distribution shape (μ) remain constant and the variation in the raindrop size distribution is due to variations in drop number density (N_t); 2) a power-law Z–R relationship with exponent b=1.63 for the so-called "size controlled situation" which is the consequence of a constant drop number concentration (N_t) and distribution shape (μ), while the variability of the drop spectrum is accommodated through variations in mean drop size (D_0); 3) a power-law Z–R relation where the exponent depends on the drop size distribution shape parameter (μ), and the prefactor is determined by μ and N_0 together.

The number controlled situation is usually occurring within the steady or equilibrium rainfall generated from the opposing forces of coalescence and break-up for rain rates higher than 50 mmh^{-1} (Zawadzki and De Agostinho Antonio, 1988). Most rainfall situations, however, exhibit a variability of drop spectra that correspond to a mix of variations in drop size and number density, from which produce intermediate power-law Z–R relationships between the number controlled and size controlled situation.

Many studies focused on the Z-R relationship have been carried out over the years. Various Z-R relationships are proposed for the different particular rain type applications or meteorological context. We summarize and compared these Z-R relationships in Table.1.3 and 1.4.

The first remark on these Z-R relationships is an inverse dependence of the prefactor on exponent, that is, large a corresponds to small b. Regarding the variation in a and b, there have been many attempts to relate the Z-R laws to the meteorological conditions. However, as we mentioned in the previous subsection, there is a great lack of consistency in the drop size distribution for meteorological classification (convective or stratifrom, continental or maritime). Even when the convective conditions appear to be similar within a rain event, the drop size distributions can be widely different from one phase to another. Nevertheless, based on long-term DSD observations during Tropical Oceans Global Atmosphere Coupled Ocean-Atmosphere Response Experiment (TOGA COARE), large prefactor (200 to 370) and moderate exponent are generally associated with stratiform rain system, while a small prefactor (120 to 175) is found for the convective rainfalls. This feature may be explained by the different characteristics of rain microstucture with stratiform rain possessing more large drops compared to convective rainfall. An exception is found for some thunderstorms, where the number controlled situation occurs with large prefactor and exponent equal to 1 .The operational Z-R relationships used in NOAA highlight the geographic locations playing also an important role in determining perfactors and exponents. However, it is worth noting the limitation of Z-R relationship comparison, because the Z-R laws listed in Table.1.3 and 1.4 have been established with different techniques and models, eventually with a variety of sensors, which make them hardly comparable in fact.

The scaling DSD formulations provide a possibility to explain the variation in Z-R relationship. Integrating the one- (1.5) or two-moment (1.6) scaling DSD formulations, one obtains two general moment relationships:

$$M_k = M_i^{\alpha+\beta(k+1)} \int_0^\infty x^k g(x) dx, \tag{1.12}$$

$$M_k = M_i^{(j-k)/(j-i)} M_j^{(k-i)/(j-i)} \int_0^\infty x^k g(x) dx, . \tag{1.13}$$

The expression (1.12) suggests that the prefector of Z-R relationship is controlled by the form of the general distribution $g(x)$ while the exponent is controlled by the scaling

Z-R relation	Condition	Reference
$Z = 830R^{1.5}$	Continental thunderstorms observed at Swiss Locarno	Joss and Waldvogel (1970)
$Z = 316R^{1.36}$	Moderate and continental thunderstorms observed at Oklahoma	Petrocchi and Banis (1980)
$Z = 261R^{1.43}$	Coastal, moderate maritime thunderstorms observed at PurtoRico	Ulbrich (1999)
$Z = 85R^{1.5}$	Summer thunderstorm measured in Locarno-Monti, Switzerland	Waldvogel (1974)
$Z = 350R^{1.5}$	Summer widespread rain measured in Locarno-Monti, Switzerland	Waldvogel (1974)
$Z = 139R^{1.43}$	Equatorial maritime convective systems	Tokay and Short (1996)
$Z = 367R^{1.30}$	Equatorial maritime stratiform systems	Tokay and Short (1996)
$Z = 148R^{1.55}$	Convective rain TRMM	Schumacher and Houze (2003)
$Z = 276R^{1.49}$	Stratiform rain TRMM	Schumacher and Houze (2003)
$Z = 44R^{1.91}$	Coastal no bright band rain observed in winter in northern California	Martner et al. (2008)
$Z = 168R^{1.58}$	Coastal bright band rain observed in winter in northern California	Martner et al. (2008)
$Z = 600R^{1.19}$	Tropical Convective rainfall phase	Sharma et al. (2009)
$Z = 248R^{1.41}$	Tropical Transition rainfall phase	Sharma et al. (2009)
$Z = 567R^{1.10}$	Tropical Stratiform rainfall phase	Sharma et al. (2009)
$Z = 369R^{1.35}$	Mediterranean Convective rainfall phase	Chapon et al. (2008)
$Z = 494R^{0.77}$	Mediterranean Transition rainfall phase	Chapon et al. (2008)
$Z = 84R^{1.43}$	Mediterranean Stratiform rainfall phase	Chapon et al. (2008)

Table 1.3: Different Z-R relationships presented in the literature 1.

Z-R relation	Condition	Reference
$Z = 240R^{1.48}$	Mount Fuji, at height of 1300 m	Fujiwara and Yanase (1968)
$Z = 88R^{1.28}$	Mount Fuji, at height of 2100 m	Fujiwara and Yanase (1968)
$Z = 48R^{1.11}$	Mount Fuji, at height of 3400 m	Fujiwara and Yanase (1968)
$Z = 200R^{1.5}$	USA, General stratiform rain	NOAA (Morin et al., 2003)
$Z = 130R^{2.0}$	Winter stratiform/orographic rain for the east of continental divide of USA	NOAA (Morin et al., 2003)
$Z = 75R^{2.0}$	Winter stratiform/orographic rain for the west of continental divide of USA	NOAA (Morin et al., 2003)
$Z = 300R^{1.4}$	Summer deep convection	NOAA (Morin et al., 2003)
$Z = 250R^{1.2}$	Topical convective systems	NOAA (Morin et al., 2003)
$Z = 600R$	Equilibrium DSD – number controlled rainfall	Hu and Srivastava (1995)

Table 1.4: Different Z-R relationships presented in the literature 2.

parameters (α and β). Uijlenhoet et al. (2003a) investigated the DSD corresponding to rain rate exceeding 100 mmh^{-1} based on the one-moment scaling formulation. They found that the extreme rain tends to be associated with number-controlled rain condition, under which the drop size scaling parameter β is equal to 0, and the number scaling parameter α is equal to 1 through the self-consistency relationship. Consequently a linear Z-R relationship was proposed to characterize this rainfall.

A curious character of the two-moment scaling framework can be seen in the moment relationship (1.13) in which the exponents of the double power-law relationship are determined by the chosen orders of moments. Therefore, only the prefactor depends on the general distribution $g(x)$. Recent studies (Illingworth and Blackman, 2002; Testud et al., 2001) showed the advantage in moment estimation based on double power-law relationship (1.13), compared to the simple moment relation (1.12). However, the variation in the general distribution remains to be investigated to determine the prefactor.

Besides the floods caused by the heavy rain fall, soil erosion due to rain is also a major issue in the fields of agriculture and water management. The determination of the rain kinetic energy (KE) by the remote sensing technique is also an interesting aspect in hydro-meteorological studies. In fact, both the Z-R and KE-Z relations can be derived from the DSD formulation. The variation in the moment relation is strongly associated with the variability of the DSD, or in other words, with the microphysical processes occurring in the rain cloud. Hence, the DSD formulation plays the role of the bridge linking the moment relation to the rain physics. That is the reason why a better knowledge of the DSD formulation is essential to improve the understanding of the rainfall microphysical processes and the moment estimates (such as the KE and R estimations).

1.3 Meteorological observations of intense precipitation

1.3.1 Cévennes-Vivarais Mediterranean Hydro-meteorological Observatory

The Cévennes-Vivarais Mediterranean Hydro-meteorological Observatory (CVMHO) is dedicated to long-term observation and modeling of hydrometeorological extremes in the Mediterranean region. This project was set up in 2000 and since then, many

researchers with different background (meteorologists, hydrologists, etc.) have been collaborating together to cope with a better understanding of extreme rain and flash floods events occurred in the Cévennes-Vivarais region. The observatory focuses on a $160 \times 200\ km^2$ window (Fig.1.6), in which the observation system includes (i) three operational weather radars belonging to the Météo-France ARAMIS network; (ii) 400 daily rain gauges and 160 hourly rain gauges provided by three organizations (Météo-France, Service de Prévision des Crues du Grand Delta, Electricité de France); (iii) 45 water level and discharge stations; (iv) 2 laser optical "Parsivel" disdrometers (Delrieu et al., 2005). The low-cost disdrometer "Parsivel" became commercially available in 2005, and is widely used since them to measure the DSD in hydrometeorological research (Chapon et al., 2008; Gultepe and Milbrandt, 2010; Yuter et al., 2006). It detects the different precipitations by a flat, horizontal laser beam, with a sampling area equal to 54 cm^2. For each 10 seconds, the measured hydrometeos are described by a 32 x 32 matrix (32 drop-size and 32 velocity bins). The CVMHO is also supported by the Météo-France meteorological datasets (such as radio soundings, analyses of the operational models). An online system (www.ohmcv.fr) for data extraction and visualization was designed and supported by LTHE (Boudevillain et al., 2011).

1.3.2 Description of the meteorological dataset

The whole meteorological dataset used in this study is collected from the CVMHO. Most discussion concerned with the rain microstructure is based on the observations of the Parsivel disdrometer installed at Alès in 2004. This laser optical disdrometer measures continuously the DSDs at 10-second interval since 2006. And the DSD observations from the September 2006 to the December 2008 are available for this study. Next to the disdrometer (2 m), a tipping-bucket rain gauge was set up to check the disdrometer measurement. In order to remove the fake raindrops, the disdrometer data were filtered based on the theoretical relationship between measured fall velocity and the diameter of raindrops with a tolerance of 60% (Jaffrain and Berne, 2011). The 10-second interval DSD data are then integrated into 1-min and 5-min time intervals. The 1-min data are used to investigate the DSD variability at a fine temporal scale and the 5-min data are used to coincide with the weather radar observations. All 1-minute DSD spectra with rain intensities less than 1 $mm\ h^{-1}$, and 5-minute DSD spectra with rain intensities

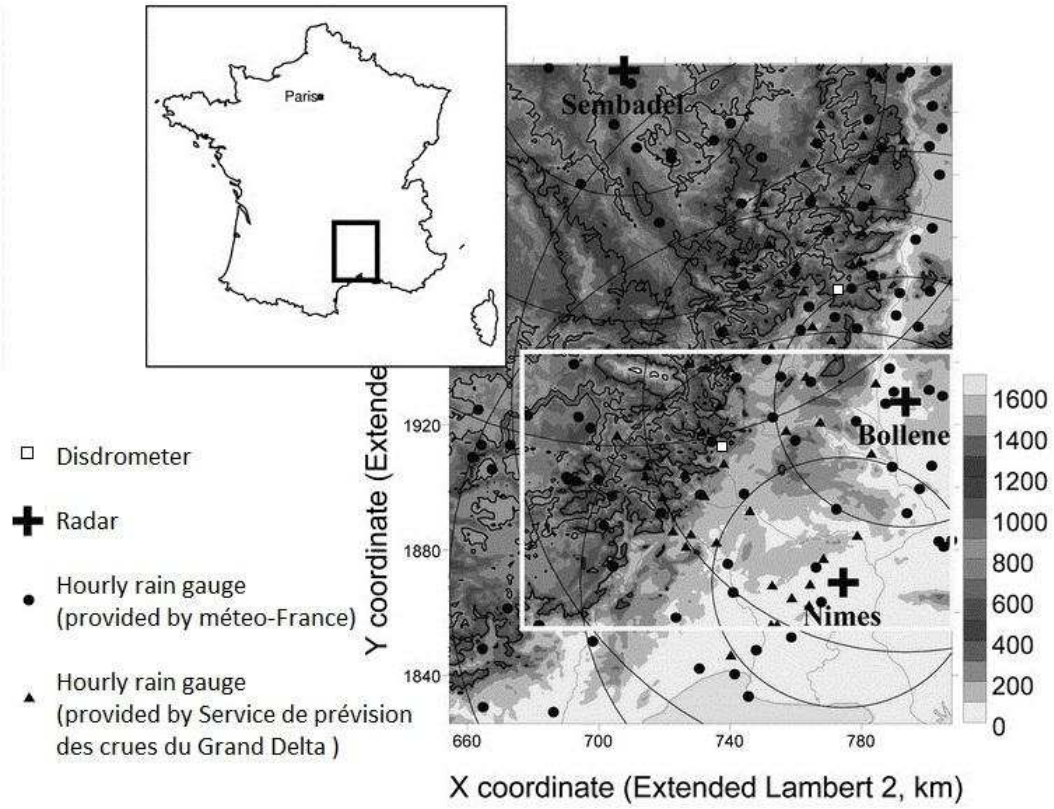

Figure 1.6: Location of the CVMHO Cévennes–Vivarais window in France. - The shaded map presents the terrain elevation data and the main Cévennes rivers. The light gray box delineates the region affected by the 8–9 Sep 2002 rain event. (Delrieu et al., 2005)

less than 0.5 $mm\ h^{-1}$ are removed from the samples to avoid the influence of the uncompleted DSD spectrum.

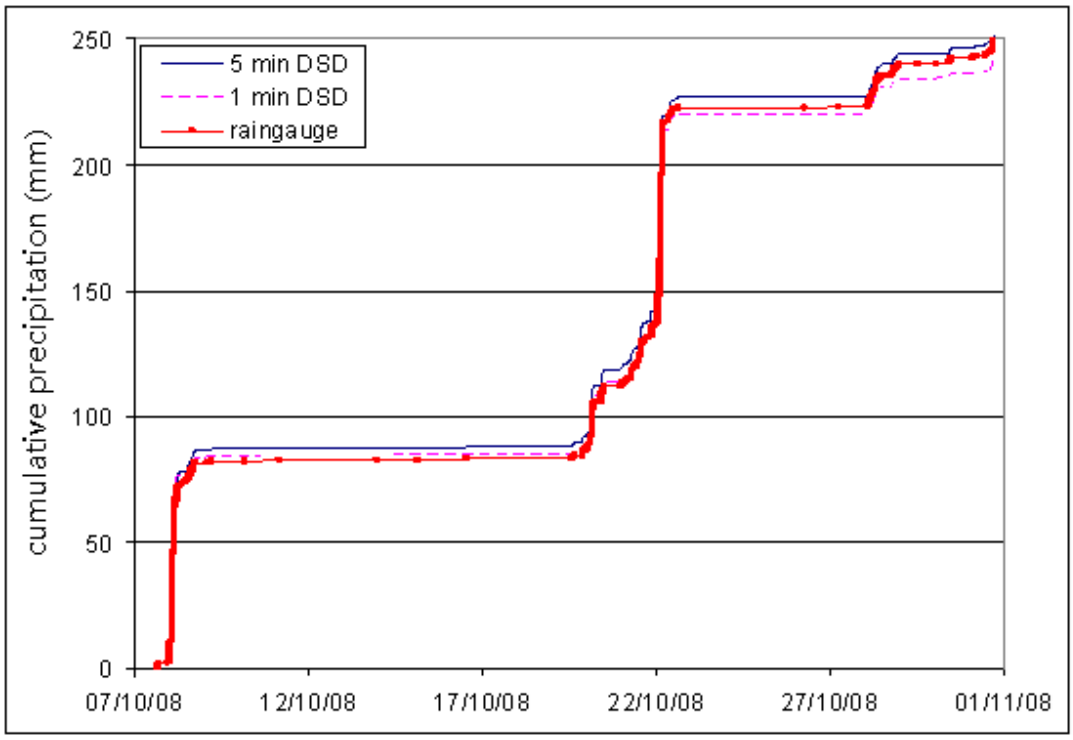

Figure 1.7: Cumulative precipitation measured by raingauge and disdrometer during October 2008. - The comparison shows good agreements of cumulative rainfall measured between the raingauge and disdrometer.

As an example, the disdrometer and rain gauge data measured during October 2008 are selected to illustrate the quality of the DSD data (Fig.1.7). The rain gauge recorded 248.6 mm of rainfall, which is in good agreement with 241.4 mm and 252.7 mm of rain derived from the 1-min and 5-min DSD dataset, respectively. The difference between these two DSD datasets is principally caused by the higher cutoff rain value (1 mmh^{-1}) for the 1-min dataset.

It should be mentioned that the measurement error of small drops can not be revealed by this comparison. As we will illustrate in Section 2.2.5, the small drops ($D < 0.5\ mm$) contribute a small part of rain rate. Thus, the variability of small raindrops concentration is nearly ignored in the comparison based on rain intensity. Although this measurement error may not be essential for investigations of Z-R relationships, a robust

measurement of small drops is still important to understand the rainfall microphysical processes.

1.3.3 Recent remote-sensing technologies

In 2008, a dual-polarization S-band weather radar was set up at Nîmes. The preliminary observations will be used, in a qualitative manner, to discuss the evolution of the DSD time series. The basic polarimetric radar products available in this study include: the copolar-correlation (ρ_{hv}), the differential reflectivity (Zdr) and the specific differential phase (Kdp).

The copolar-correlation (ρ_{hv}) is defined as the measure of how similarly the horizontally and vertically polarized signals are behaving within a pulse volume. This correlation (ρ_{hv}) is unit less and its value can be from -1 to 1. When different types of hydrometeors are present within a pulse volume, the ρhv will decrease toward 0. In practice, the non-meteorological and meteorological echoes are clearly discriminated by the ρ_{hv} with a threshold of about 0.8. The non-uniform meteorological echoes such as hail and melting snow produce ρ_{hv} values between 0.8 and 0.97. And for the fairly uniform meteorological echoes such as rain and snow, the horizontal and vertical pulses change in similar manners resulting in ρ_{hv} greater than 0.97.

Differential reflectivity (Zdr) is defined as the difference between the horizontal and vertical reflectivity factors (1.14). In most cases, its value can range from -7.9 to +7.9 in units of dB. Since Zdr is a ratio of powers, it is immune to the radar calibration.

$$Zdr = 10 \log_{10}(Z_h/Z_v). \tag{1.14}$$

The physical interpretation of Zdr is related to the ratio of horizontal to vertical axis of hydrometeors. If the mean drop shape is spherical, such as for drizzle and small hail, Zdr will be close to 0 dB. And if the mean hydrometeor is horizontally oriented, such as for rain or melting hail, Zdr will be positive because the horizontal reflectivity factor will be greater than the vertical reflectivity. Conversely, Zdr will be negative for the vertical oriented hydrometeors, such as the vertically oriented ice crystals. Zdr possesses a potential advantage for raindrop observation thanks to the strong relationship between raindrop diameter and shape. Smaller raindrops tend to be spherical and larger drops tend to be oblate. This relationship leads to another relationship between the Zdr value and the mean raindrop size within a pulse volume.

For example, Wakimoto and Bringi (1988) showed the typical Zdr values for various raindrops (Table.1.5).

Major axis diameter (mm)	$Zdr(dB)$
Smaller than 0.3 mm	0.0 dB
1.35 mm	1.3 dB
1.75 mm	1.9 dB
2.65 mm	2.8 dB
2.90 mm	3.3 dB
3.68 mm	4.1 dB
4.00 mm	4.5 dB

Table 1.5: Relationships between the major axis diameter of raindrop and the Zdr values.

Bringi and Chandrasekar (2001) indicated that Zdr values are linked to the mass-weighted mean diameter (D_m) for S-band radar, with

$$D_m = 1.619 Zdr^{0.485}, \tag{1.15}$$

where the mass-weighted mean diameter D_m is the ratio of the 4^{th} DSD moment to the 3^{rd} DSD moment, defined as,

$$D_m = \frac{\int_0^\infty N(D) D^4 dD}{\int_0^\infty N(D) D^3 dD}. \tag{1.16}$$

In terms of phase measurement, the propagation of the horizontal and vertical pulses is also affected by the asymmetry of hydrometeors. Due to the different shapes of hydrometeors, the attenuation of horizontal and vertical pulses yield a phase shift. Unlike Zdr, this phase shift is not only affected by the hydrometeors form, but also related to the hydrometeor concentration. The more hydrometeors present in a pulse volume, the more differential phase shifting will occur. One should note also the phase shifting is accumulated through the propagation distance. In order to remove the distance impact, the specific differential phase (Kdp) shift is used in the literature, which is defined as the range derivative of the differential phase shift with the unit deg/km. Its possible values range from -2 to 7 deg/km. A relationship between Kdp and rainfall variables was proposed by Bringi and Chandrasekar (2001), as

$$Kdp \approx C(180/\Lambda)10^{-3} LWC(0.062 D_m) \tag{1.17}$$

where C ≈3.75 is dimensionless. Λ and LWC is radar wavelength and rainwater content, respectively. The specific differential phase, the differential reflectivity and the reflectivity factor provide 3 independent observations of microstructure of rainfall. Recent studies have already showed the advantages of these observations for retrieving the DSD parameters (Bringi et al., 2002; Kim et al., 2010).

1.4 Objectives of this thesis

It has been demonstrated that all physical properties of rain are linked to the microstructure of rainfall. A better understanding of the variation in the raindrop size distribution is essential to investigate the rainfall physical processes and the DSD moment relationships. Although many individual contributions (single- or two-moment(s) scaling DSD formulations) have been made since the beginning of the radar-meteorological research, a general framework for the harmonization of these contributions is still lacking. It is the aim of this thesis to provide a unified DSD formulation synthesizing the single- and multi-moment scaling formulations, in the context of Mediterranean intense rainfall. A framework for parameter estimation procedure is proposed associated to the DSD formulation.

Once the robust formulation is established, we are able 1) to investigate the intra-event DSD variability to understand the microstructure of the Mediterranean intense rainfall; 2) to derive the DSD moments relationships for the rain variables estimations (such as the Z-R, KE-Z relationships) based on different DSD formulations.

To achieve the goals of this thesis, in Chapter 2, considering a well-defined "general distribution" $g(x)$ as the probability density function (*pdf*) of the raindrop diameter scaled by a characteristic diameter (D_c), a scaling DSD formulation is proposed to parameterize the natural raindrop size distribution. Different parameterization aspects, such as the estimation methods, the truncation effects, are studied to produce a robust model for each individual DSD spectrum, based on the 3-year observations of the disdrometer.

The formulation is then adapted to the one- and two-moment scaling parameterization, in Chapter 3, by introducing single and dual power-law models between the reference (or predictor) moment(s) and the explained moments (total concentration,

characteristic diameter). Compared with previous formulations presented in the literature, this approach explicitly accounts for the prefactor of the power-law models to yield a homogeneous and dimensionless general distribution $g(x)$ whatever the predictor moment(s) considered. A series of the DSD spectra are required to establish the power-model between the reference moment(s) and the explained moments so it is impossible to parameterize each DSD spectrum under this context. The associated parameter estimation procedures are proposed; the rain rate (R) and the radar reflectivity factor (Z) are applied separately and jointly to show examples of the one- and two-moment scaling formulations, respectively.

Three applications of the scaling formulation are then illustrated in Chapter 4. The first application is concerned by the investigation on intra-event DSD variability for a typical Mediterranean rain event by the multiple polarimetric and Doppler radar (reflectivity factor, differential reflectivity, specific differential phase, Doppler velocity) and in-situ observations (disdrometer and meteorological observations). A preliminary discussion about the DSD variation reflected by remote observations is provided. Next, the reconstitution of the DSD by remote and in-situ observation is performed based on the climatological scaling formulation. The third application will be devoted to study how to estimate the rain fall kinetic energy from the observed DSD moments, such as Z and R.

Finally, the main findings of this study are concluded in Chapter 5, with a broad perspective for future DSD research. The entire manuscript is organized from theoretical concepts to practical applications. The next chapter will introduce the basis of the scaling technique in the DSD parameterization framework.

Chapter 2

Scaling technique and DSD formulation

The raindrop size distribution (DSD) is the key to understand the physical rainfall processes and to improve the estimates of moments and the relationships between moments, such as the Z-R relationship. Instead of dealing directly with the raindrops counts in each diameter-size class, the analytical formulation provides a convenient solution to describe the whole spectrum by some parameters. In this chapter, a scaled DSD formulation based on the probability density function will be presented. The objective is to propose a general scaled DSD model, with physical meaningful parameters, making full use of the self-consistency relationships.

2.1 Degrees of freedom in the DSD

2.1.1 Number of free parameters in DSD formulations

Basically, the exponential and gamma DSD formulations described in Section 1.2.2 express the DSD as a mathematical function of the drop diameter (D). The approximation of the DSD by these functions means the drop number in each diameter-size interval cannot be totally independent. The number of small drops is, in some manner, linked to that of the large drops. In fact, a totally random drop size distribution is impossible to be represented by an analytical function. The exponential and gamma DSD formulations reflect the inherent constraint on the rain drop counts in different diameter-size intervals. And thanks to this constraint, the variation in the DSD spectrum is able to be analytically described by several (one to three) parameters.

The scaling technique provides another way to parameterize the DSD. In its most general acceptance, this approach doesn't assume any analytical function on the DSD spectrum. The variation in the DSD spectra is supposed to be only determined by the DSD moment(s). Therefore, one can scale the DSD by different moment(s) to obtain a constant and inherent distribution (the so-called general distribution), which is independent to the DSD moments. In fact, The scaling technique is, under the same objective as the parametrization by analytical expression, to reduce the variability of DSDs into evolutions of several moments. One can imagine that a parameterization of a totally random DSD spectrum with n diameter-size intervals, needs n parameters in the analytical expression, or n DSD moments in the scaling processes. Hence, the number of free parameters required in the analytical expression, is in some manners, related to the number of moments needed in the scaling process.

How many free parameters or moments are required in the DSD parameterization is a core question. The exponential DSD formulation describes the variation in DSDs by two parameters (N_0 and λ), while the gamma function adds the third shape parameter (μ). Studies indicate that the three parameters in the gamma function are not totally independent. Hence, the number of the required free parameters in the DSD analytical expression is expected to be between 2 and 3. Regarding the scaling technique, the successful representation of the DSD by a two-moment normalization (Lee et al., 2004) suggests that two moments are probably enough to represent the whole DSD spectrum. However, the same problem is that these two moments are not totally independent

either. In order to determine the degrees of freedom of the DSD, a robust statistic method, the principal component analysis (PCA) is applied in the beginning section of this chapter.

2.1.2 Principal component analysis on the DSD moments

Salles (1995) applied the principal component analysis (PCA) on the raindrop size distribution investigation. He found that the first 3 principal components explain 90% of total DSD variability. However, the direct implementation of the PCA on the DSD has some major shortcomings. For example, it is well recognized that the relationship between $N(D1)$ and $N(D2)$ ($D1 \neq D2$) is non-linear, while the PCA is more convenient in the analysis for linear systems. Thus a better PCA implementation should be on the logarithmic-transformed DSDs. But such a transformation is inappropriate for some uncompleted DSD spectra (some diameter-size intervals have no raindrop).

As regard to the DSD moments, Haddad et al. (1997) parameterized the DSD by rain intensity (R), mass-weighted mean drop diameter (D_c) and a shape parameter (s'). The advantage of their parameterization is that the three parameters (R, D_c and s') are statistically independent. However, a slight correlation is exhibited for rain exceeding 12 $mm\ h^{-1}$ (Haddad and Rosenfeld, 1997). DSD studies confirm the presence of multiple power law relationship among the DSD moments (Lee et al., 2004). Following their ideas, the PCA is envisaged here to analyse the log-transformed DSD moments, to 1) obtain the independent explaining parameters; 2) respect the multiple power law relationships among the DSD moments.

The 5-min DSD observations described in Section 1.3 are integrated into 13 successive moments (0^{th}, 0.5^{th}, 1^{st} ..... 6^{th}). These moment values are transformed by the logarithm function (log_{10}). Before the PCA analysis, the boxplot shows the statistical features of each log-transformed moment (Fig.2.1). The log-transformation reduces significantly the distinction of the variability among different moments. The medians and quartiles of all moments are between 2 and 3. This transformation insures the homogeneous weight of each moment for the principal component analysis. The cumulative variability explained by the principal components is showed in Fig.2.2. 85% of total variability is explained by the first component. The percentage increases to 99.5% if the second component is taken into account. And the first three principal components explain nearly 100% of the variance.

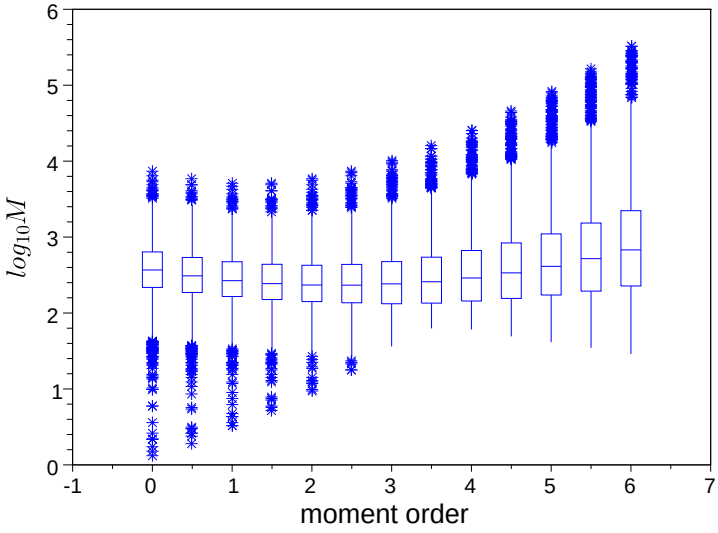

Figure 2.1: Boxplot of the log-transformed DSD moments for the 5-min data. - The boxplot shows the comparable variation among the DSD moments after the log-transformation.

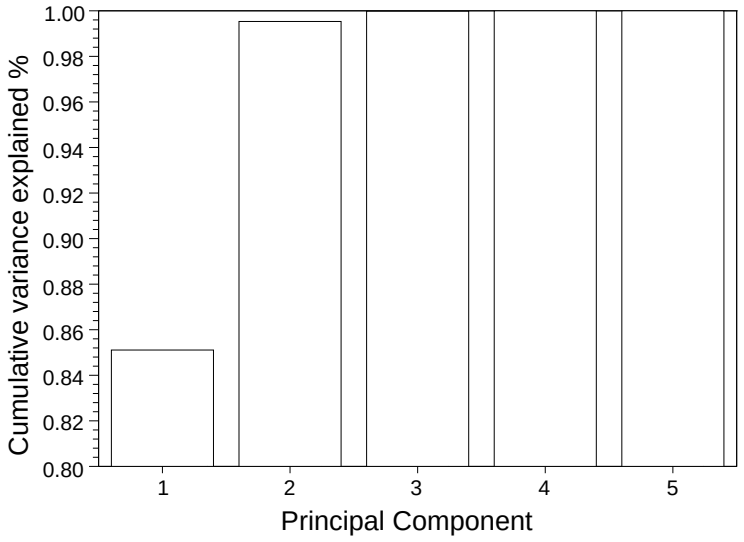

Figure 2.2: Cumulative variability explained by the principal components. - The first two principal components explain 99% variability of the whole log-transformed DSD moments.

The result of PCA shows the significant increase of the explained variance if the second (independent) principal component is used. The introduction of the third principal component yields a perfect representation of the original variation, but its improvement is relatively limited. The first three coordinates of the PCA are showed in Fig.2.3, illustrating three basic patterns of the log-transformed DSD moments. The first and second coordinates exhibit quasi linear patterns, while the third pattern is represented by a non-linear function. In the basis of the PCA theory, any log-transformed DSD moments can be reconstituted by the linear combination of these patterns. Selecting the 1^{st}, 1^{st} and 2^{nd} or 1^{st} 2^{nd} and 3^{rd} principal component(s), respectively, we reconstitute the DSD moments (M_0 to M_6) in Fig.2.4 to Fig.2.6. The reconstituted expressions of the DSD moments are written as:

$$M_0 = PC_1^{0.133} PC_2^{-0.455} PC_3^{0.498} \tag{2.1}$$

$$M_1 = PC_1^{0.156} PC_2^{-0.375} PC_3^{0.099} \tag{2.2}$$

$$M_2 = PC_1^{0.193} PC_2^{-0.264} PC_3^{-0.206} \tag{2.3}$$

$$M_3 = PC_1^{0.244} PC_2^{-0.127} PC_3^{-0.332} \tag{2.4}$$

$$M_4 = PC_1^{0.304} PC_2^{0.027} PC_3^{-0.248} \tag{2.5}$$

$$M_5 = PC_1^{0.368} PC_2^{0.189} PC_3^{0.023} \tag{2.6}$$

$$M_6 = PC_1^{0.434} PC_2^{0.352} PC_3^{0.430} \tag{2.7}$$

where the exponents of PC_1, PC_2 and PC_3 correspond to the first three patterns shown in Fig.2.3. Regarding the reconstitution by the first principal component (Fig.2.4), the middle order moments, such as M_4 and M_5, are well reconstituted, while the reconstitutions of the low and high moments, e.g. M_0 and M_6, produces a large error and bias. The introduction of the second principle component reduces significantly the reconstituted error both for the high and low order moments. And a nearly prefect reconstitution is produced if the third principle component is further used. In fact, the improved qualities of reconstitutions agree well with the variance explained by the principle components. More variance explained by principle components, better quality of DSD moments reconstituted by their combinations.

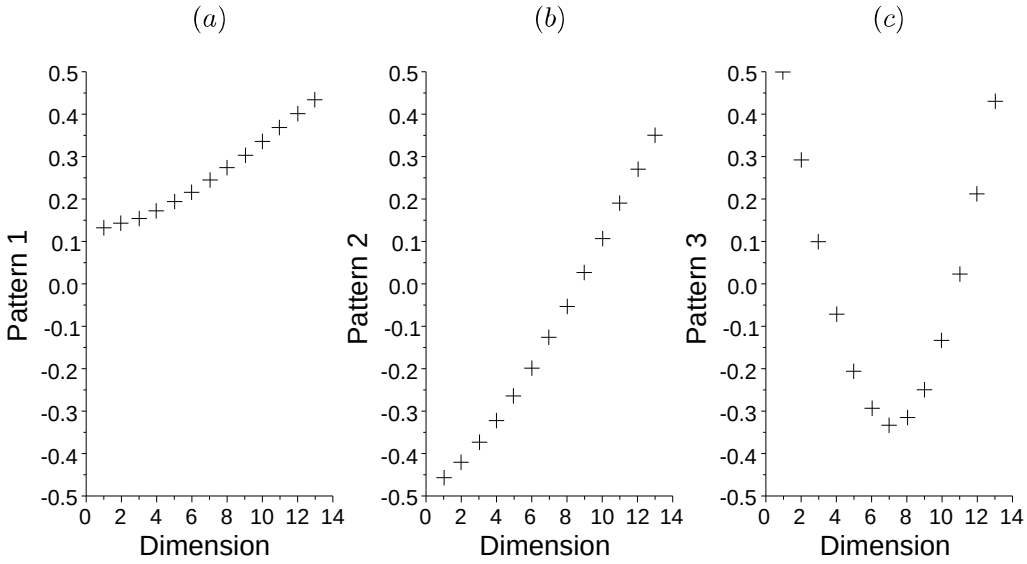

Figure 2.3: First three patterns of the DSD in the PCA. - Three major patterns correspond to the first three principle components.

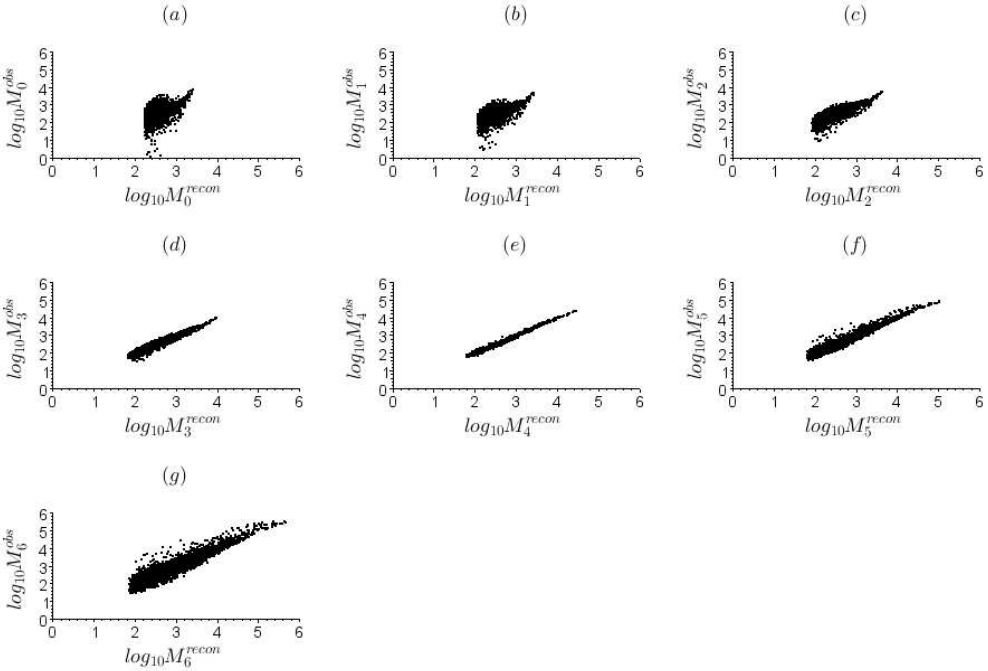

Figure 2.4: Reconstitution of log-transformed DSD moments based on the first principal component. - The measured moments (0^{th} to 6^{th}) are plotted against the reconstitutions (M_i^{recon}) in figures (a) to (g), respectively.

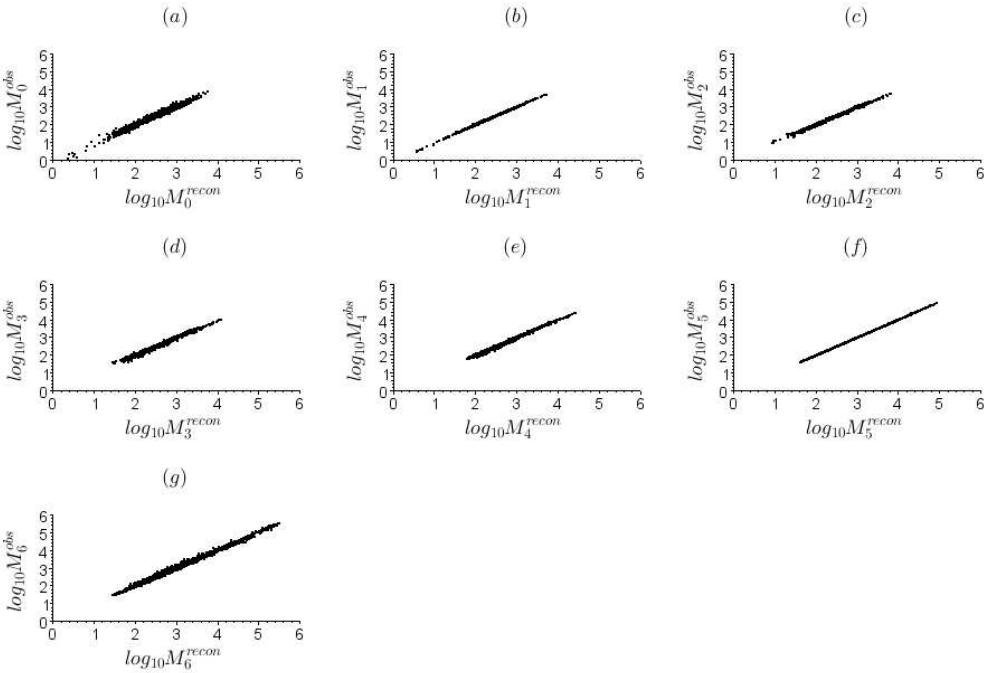

Figure 2.5: Reconstitution of log-transformed DSD moments based on the first two principal components. - The measured moments (0^{th} to 6^{th}) are plotted against the reconstitutions (M_i^{recon}) in figures (a) to (g), respectively.

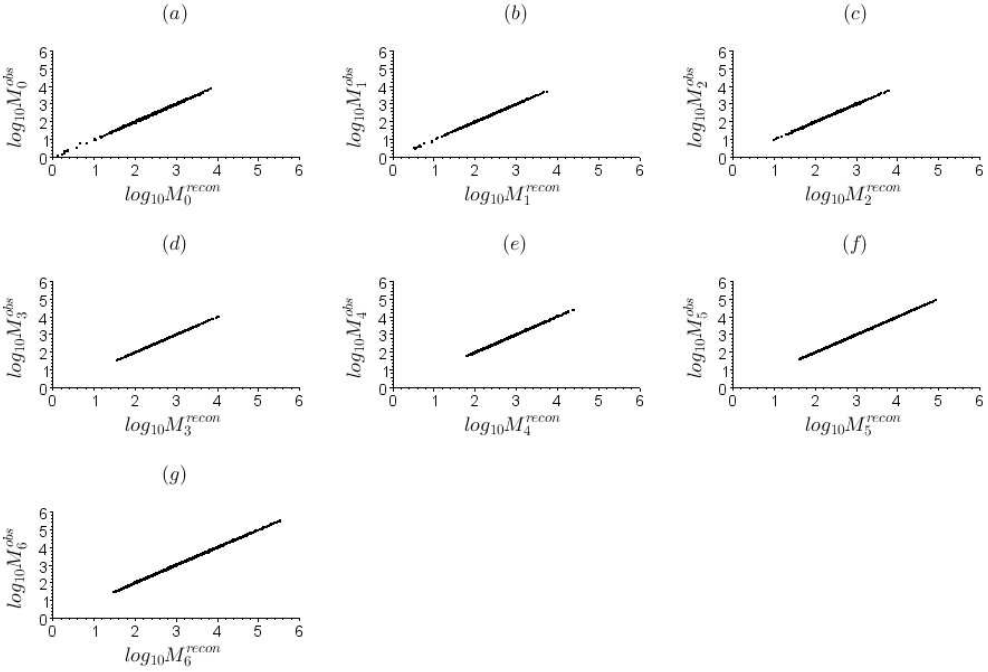

Figure 2.6: Reconstitution of log-transformed DSD moments based on the first three principal components. - The measured moments (0^{th} to 6^{th}) are plotted against the reconstitutions (M_i^{recon}) in figures (a) to (g), respectively.

2.1.3 Interpretation of the principal components

The previous discussions suggest that 3 principle components are largely enough to represent the variability of the DSD moments. It will be interesting to further investigate the physical meanings of these principal components. The correlation coefficient between each principal component and log-transformed moments are calculated in Table.2.1, which indicate a perfectly linear relationship between the first principal component and the log-transformed values of the middle order moment (M_4). It means that the information of such moment is largely contained in the first principle component. This feature explains the robust reconstitution of the middle order moments by the first principle component (Fig.2.4) , and also implies the rain intensity (R) to be a good candidate as a scaled moment in the normalized framework.

PC	M_0	M_1	M_2	M_3	M_4	M_5	M_6
PC_1	0.57	0.71	0.87	0.97	1.00	0.98	0.95
PC_2	-0.80	-0.70	-0.49	-0.21	0.04	0.21	0.32
PC_3	0.16	0.03	-0.07	-0.10	-0.06	0.00	0.07

Table 2.1: Coefficients of cross correlations between principal components and log-transformed moments.

The introduction of the second principle component brings the information of low moment into the reconstitution. The high negative correlation coefficient between PC_2 and M_0 suggests that the second principle component is likely related to the DSD concentration. This inference can be easily verified by the reconstitution showed in Fig.2.5. Regarding the third principle component, no physical dependency is found in the current study. Its interpretation needs further investigations with more precise DSD measurements.

Based on the result of the PCA, it seems that the middle and low order moments are essential to determine the variation in the DSD. The combination of the low and middle moments should be a good candidate for the DSD scaling process because these two type moments contain most variances of the total DSD moments. This idea will be respected in the following discussion in order to propose a robust and meaningful scaling DSD formulation.

2.2 DSD formulation scaled by concentration and characteristic diameter

2.2.1 DSD formulation

As pointed out by Uijlenhoet et al. (2003a,b) a raindrop size distribution is in fact a mixture of two different notions, namely that of the concentration N_t within a unit air volume (expressed in $[m^{-3}]$) and that of the probability distribution function (*pdf*) $p(D)$ $[mm^{-1}]$ of the rain drop diameter D $[mm]$, with:

$$N(D) = N_t \cdot p(D). \tag{2.8}$$

In order to work with a dimensionless probability density function, denoted by $g(x)$ hereafter, Porrà et al. (1998) suggested introducing a characteristic diameter D_c $[mm^{-1}]$ in (2.8), to yield:

$$N(D) = \frac{N_t}{D_c} g(x) \quad with \quad x = \frac{D}{D_c}. \tag{2.9}$$

Contrary to previous authors (e.g., Sempere Torres et al. (1994); Testud et al. (2001)), we impose a priori in this work the function $g(x)$ [-] to be a true *pdf*. Among the available models for *pdf s*, and due to the usual shapes of DSDs, we have selected the two-parameter gamma *pdf* (Mood et al., 1974) for modeling the $g(x)$-function:

$$g(x;\lambda,\mu) = \frac{\lambda^{\mu+1}}{\Gamma(\mu+1)} x^{\mu} exp(-\lambda x). \tag{2.10}$$

Note that if μ=0, this model reduces to the one-parameter exponential *pdf*:

$$g(x;\lambda) = \lambda exp(-\lambda x). \tag{2.11}$$

As suggested by Lee et al. (2004), the three-parameter generalized gamma *pdf* could provide further flexibility for the DSD adjustment at the cost of the estimation of an additional parameter c:

$$g(x;\lambda,\mu,c) = \frac{c\lambda^{c(\mu+1)}}{\Gamma(\mu+1)} x^{c(\mu+1)-1} exp\left[-(\lambda x)^c\right]. \tag{2.12}$$

Nevertheless, introducing (2.10) in (2.9) yields:

$$N(D) = \frac{N_t}{D_c} g(x;\lambda,\mu) = \frac{N_t}{D_c}\left[\frac{\lambda^{\mu+1}}{\Gamma(\mu+1)}\left(\frac{D}{D_c}\right)^{\mu} exp\left(-\lambda\frac{D}{D_c}\right)\right]. \tag{2.13}$$

Although more complex than classical DSD models (exponential, gamma) and less general than (2.12), the DSD formulation (2.13) has several definite advantages since: (i) the term between square brackets is the *pdf* of the scaled diameter $x = D/D_c$ with, by definition, $\int_0^\infty \frac{\lambda^{\mu+1}}{\Gamma(\mu+1)} x^\mu exp(-\lambda x)dx = 1$; (ii) the two parameters λ and μ are dimensionless; (iii) besides the two parameters λ and μ, the DSD depends on two physical variables, namely the total concentration of drops N_t and the characteristic diameter D_c; (iv) if we consider D_c/λ as one parameter, the DSD formulation (2.13) contains effectively only three free parameters. As we will show in the following subsection, a self-consistency relationship can be found between λ and μ depending on the choice of D_c. Based on the concept of normalization, the general distribution $g(x)$ is expected to characterize an intrinsic shape of the scaled DSD, ideally independent of N_t and D_c. The variability of λ and μ is hoped to depend on the meteorological conditions which govern the evolution of the raindrop concentration and the characteristic diameter in time and/or space.

Introducing (2.13) into the expression of the k^{th} order moment of the DSD yields:

$$M_k = \int_0^\infty N(D)D^k dD = \frac{\Gamma(\mu+k+1)}{\Gamma(\mu+1)} \frac{N_t D_c^k}{\lambda^k}. \tag{2.14}$$

Equation (2.14) allows us to estimate any moment M_k by N_t, D_c and the two parameters of the gamma *pdf* model: μ and λ. Another point to be addressed here before considering DSD moments and bulk variables is that the raindrop diameters extend over a range of values D_{min} and D_{max} which depend both on rainfall processes and on instrumental limitations. D_{min} and D_{max} do have to be considered as additional parameters of the DSD model and this undoubtedly makes the modeling more complex. For the sake of clarity, we assume $D_{min} = 0$ and $D_{max} = \infty$ for the main discussion of this study. The detail truncation problem will be address in the subsection 2.2.3.

Several possibilities are suggested in the literature concerning the choice of the characteristic diameter D_c: the mean diameter $D_m = M_1/M_0$, the median volumetric diameter D_v defined as $\int_0^{D_v} N(D)D^3 dD = \int_{D_v}^\infty N(D)D^3 dD$, or, as a generalization of the mean diameter, the ratio of two successive moments

$$D_{k+1,k} = \frac{M_{k+1}}{M_k}. \tag{2.15}$$

Due to classical observation problems of small raindrops and our interest for high order moments of the DSD (from k=3 for the liquid water content up to k=6 for the radar

reflectivity factor, typically), we have chosen as Testud et al. (2001) the following characteristic diameter hereafter:

$$D_c = D_{4,3} = \frac{M_4}{M_3}. \tag{2.16}$$

We must emphasize that the function $g(D/D_c)$ obviously depends on the definition of the diameter D_c. For the choice made herein, considering successively k=4 and k=3 in (2.14) and taking their ratio yields a so-called self-consistency relationship:

$$\lambda = \mu + 4, \tag{2.17}$$

which corresponds to a deterministic constraint between the two parameters μ and λ. Similarly, setting k=0 in (2.14) yields $N_t = M_0$, indicating very naturally that the 0^{th} order moment is *a priori* the best estimator for the total concentration. However, observation problems associated with the tiny raindrops may limit the validity of this result in practice.

2.2.2 Parameter estimation procedures

Assuming $N_t = M_0$, $D_c = M_4/M_3$, only one parameter, μ or λ in the DSD formulation (2.13) remains to be estimated. In this subsection, two estimation procedures are proposed, based on three moments (M_0, M_3 and M_4) and on all moments (M_0, $M_{0.5}$, M_1 ..... M_6), respectively. Considering the three moments used to define N_t and D_c, we express M_4 and M_3 through (2.14) as

$$M_4 = \frac{\Gamma(\mu+5)M_0(M_4/M_3)^4}{\Gamma(\mu+1)\lambda^4} \tag{2.18}$$

$$M_3 = \frac{\Gamma(\mu+4)M_0(M_4/M_3)^3}{\Gamma(\mu+1)\lambda^3}. \tag{2.19}$$

Combination of equations (2.18) and (2.19) so as to eliminate λ yields,

$$\frac{M_4^{1/4}}{M_3^{1/3}} = \frac{\Gamma(\mu+1)^{1/3}\Gamma(\mu+5)^{1/4}M_0^{1/4}}{\Gamma(\mu+1)^{1/4}\Gamma(\mu+4)^{1/3}M_0^{1/3}}. \tag{2.20}$$

A non-linear algorithm is applied to solve for the DSD shape parameter (μ) in (2.20).

A second method which is called "the ratio estimator" is proposed. Hazenberg et al. (2011) demonstrated its advantages in estimating parameters for the one-moment

scaling DSD formulation. Based on the moment relationship (2.14), the ratio of two successive moments for each DSD spectrum can be expressed as

$$\frac{M_{k+1}}{M_k} = \frac{D_c}{\lambda}(\mu + 1) + \frac{D_c}{\lambda}k. \tag{2.21}$$

Hence, μ and λ of each spectrum can be derived from a linear regression of all ratios of successive moment (M_{k+1}/M_k) on k. The slope and intercept in (2.21) produce independently the value of μ and λ, which are showed in Fig.2.7. The plot of the two parameters is in good agreement with the self-consistency relationship (2.17).

In order to compare the two estimators, the values of μ estimated by three moments through the non-linear relationship (2.20), and by all successive moments through the linear relationship (2.21), are plotted in Fig.2.8. The three-moment estimator produces larger values of μ compared to that estimated by all-moment estimator, especially for the high μ values. An evaluation of estimators will be addressed in Subsection 2.2.4, which shows that the scaling model fitted by 3 moments is robust enough to represent the natural DSD variability.

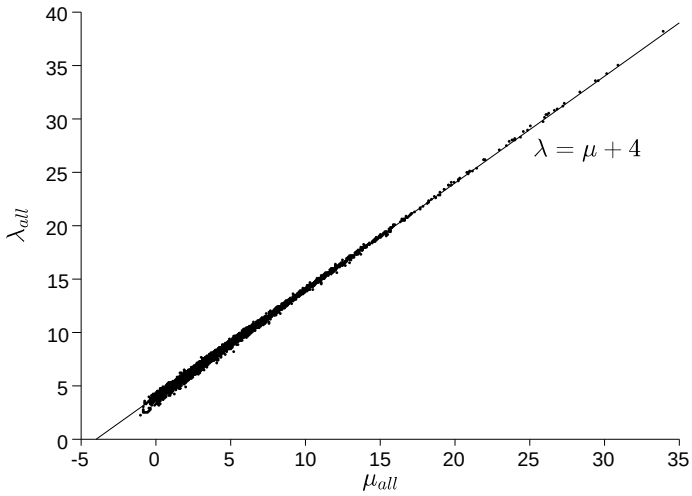

Figure 2.7: Relationship between the two parameters (μ and λ). - The two parameters are derived independently from a linear regression of all ratios of successive moment, for the climatological 5-min DSD dataset.

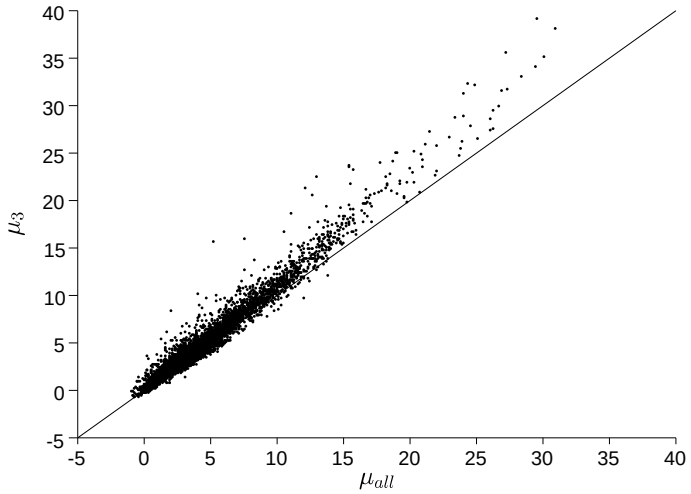

Figure 2.8: Comparison of μ derived from different estimators for the climatological 5-min DSD dataset. - The μ_3 is derived from the three DSD moments (M_0, M_3 and M_4), while the μ_{all} is obtained from a linear regression of all ratios of successive moment.

2.2.3 Effects of the DSD truncation

Due to rain microphysical processes and the instrumental limitations, the true rain moments are truncated at lower and upper drop diameters, denoted by D_{min} and D_{max}, respectively,

$$M_k^{Trun} = \int_{D_{min}}^{D_{max}} N(D) D^k dD. \tag{2.22}$$

The approximation of the truncated moment (M_k^{Trun}) by the complete moment (M_k) yields a bias in the parameters estimation. This problem was well studied by several previous works, such as Sekhon and Srivastava (1970); Ulbrich (1985, 1992), on assumption of different DSD formulations. Their findings indicated significant influences of truncation on the retrievals of the DSD parameters for the exponential and gamma DSD formulations. Hence, a special investigation on the truncation effect is addressed here for the scaled DSD formulation.

Considering the truncation effect, we define the truncated general distribution $g_t(x)$

as,

$$g_t(x) = \frac{g(x)}{\int_0^{x_{max}} g(x)dx - \int_0^{x_{min}} g(x)dx}, \tag{2.23}$$

where x_{max} and x_{min} are the upper and lower scaled diameters. They can be calculated by

$$x_{max} = D_{max}/D_c, \quad x_{min} = D_{min}/D_c. \tag{2.24}$$

In order to derive a simple mathematical expression, the lower incomplete gamma function is defined as:

$$\gamma(s, x) = \int_0^x t^{s-1}e^{-t}dt. \tag{2.25}$$

Introducing the $g(x)$ expression (2.10) and the incomplete gamma function (2.25) into (2.23) yields the expression of the general truncated distribution:

$$g_t(x) = \frac{x^\mu exp(-\lambda x)}{\frac{\gamma(\mu+1,\lambda x_{max})}{\lambda^{\mu+1}} - \frac{\gamma(\mu+1,\lambda x_{min})}{\lambda^{\mu+1}}}. \tag{2.26}$$

Then the truncated DSD can be expressed as:

$$N(D) = \frac{N_t}{D_c}\frac{\lambda^{\mu+1}x^\mu exp(-\lambda x)}{\gamma(\mu+1,\lambda x_{max}) - \gamma(\mu+1,\lambda x_{min})} \quad with \quad \frac{D_{min}}{D_c} < x < \frac{D_{max}}{D_c}. \tag{2.27}$$

Integrating this DSD formulation (2.27) with respect to the D^k, any truncated DSD moment is written as

$$M_k^{Trun} = \frac{N_t D_c^k}{\lambda^k}\frac{\gamma(\mu+k+1,\lambda x_{max}) - \gamma(\mu+k+1,\lambda x_{min})}{\gamma(\mu+1,\lambda x_{max}) - \gamma(\mu+1,\lambda x_{min})}. \tag{2.28}$$

Similar to the previous section, the deterministic constraint between λ and μ can be found through the following self-consistency relationship,

$$\lambda = \frac{\gamma(\mu+5,\lambda x_{max}) - \gamma(\mu+5,\lambda x_{min})}{\gamma(\mu+4,\lambda x_{max}) - \gamma(\mu+4,\lambda x_{min})}. \tag{2.29}$$

One may note that the constraint (2.29) simplifies to the simple self-consistency relationship (2.17) if $x_{min} = 0$ and $x_{max} = \infty$. The combination of equations (2.28) and (2.29) is then used to determine the DSD parameters for each DSD spectrum, by setting $M_k^{Trun} = M_0$, M_3 or M_4 in (2.28). A non-linear algorithm based on the modified Powell hybrid method (Powell, 1964) is applied to retrieve the DSD parameters. The values of the μ and λ estimated by 3 complete moments in previous section are used as the initial guess of parameters. In practice, due to the complexity of incomplete gamma

function (2.28), the solving algorithm cannot converge for some particular scaled DSD spectra under the considered algorithm precision ($< 10^{-10}$). Most of these particular scaled spectra possess a convex downward shape distribution with a negative μ. In order to simplify the calculations, the values of the μ and λ parameters estimated by complete moments are used for these spectra, which account for 3.77% of total 5-min spectra.

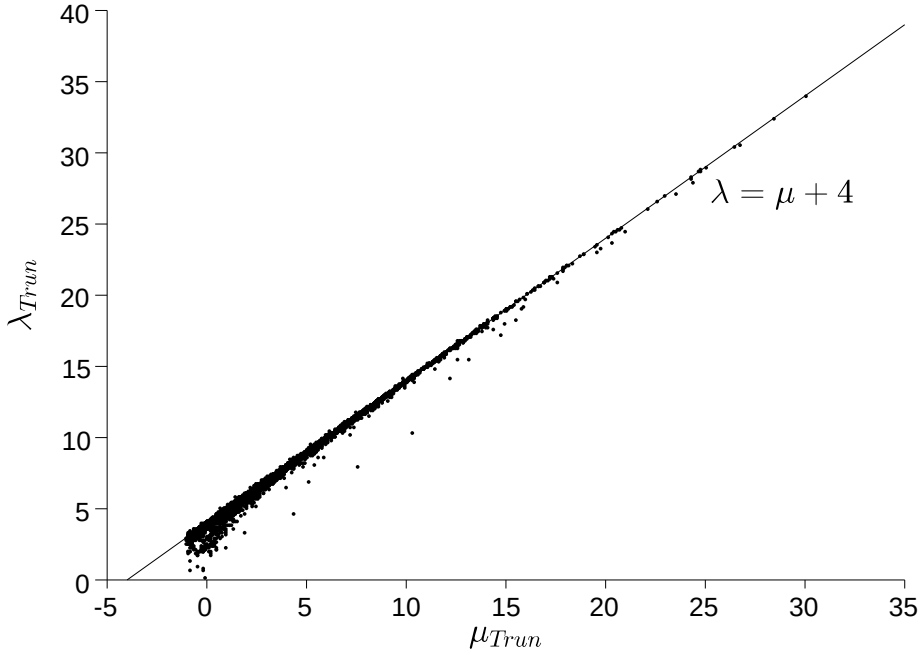

Figure 2.9: Relationship between the two parameters (μ and λ) derived from the three truncated moments for the 5-min DSD dataset. - A non-linear algorithm based on the modified Powell hybrid method (Powell, 1964) is applied to retrieve the DSD parameters based on (2.28) and (2.29), using M_0, M_3 and M_4.

In Fig.2.9, the relation (2.29) between μ_{Trun} and λ_{Trun} is illustrated, with a solid line representing $\lambda = \mu + 4$. Regardless the incomplete moments are considered, the relationship (2.29) is still similar to the simple self-consistency relationship (2.17). Some scatter can be found when the shape parameter μ is around zero. That means that the truncation effects play an important role on the $\mu - \lambda$ relationship for the spectra when the shape parameter (μ) is small. Fig.2.10 represents the contours of λ as a function of

x_{min} and x_{max} for two special cases: $\mu = 1$ and $\mu = 10$ based on the $\mu - \lambda$ relationship (2.29). It confirms that the truncation effect becomes significant to alter the simple $\mu - \lambda$ relationship (2.17) if the DSD spectrum has small upper scaled diameter x_{max} (x_{max} <1.5) and small shape parameter μ (e.g. the area of contours between λ=4.5 and 5 for the $\mu = 1$ is smaller than that of contours between λ=13.5 and 14 for $\mu = 10$). On the contrary the D_{min}/D_c has little influence on the $\mu - \lambda$ relationship. A histogram of the x_{max} is illustrated in Fig.2.11 for the total 5-min DSD spectra with a mode equal to 2.2, which explains that the truncation has an insignificant effect on the $\mu - \lambda$ relationship for the most 5-min DSD spectra in our study case.

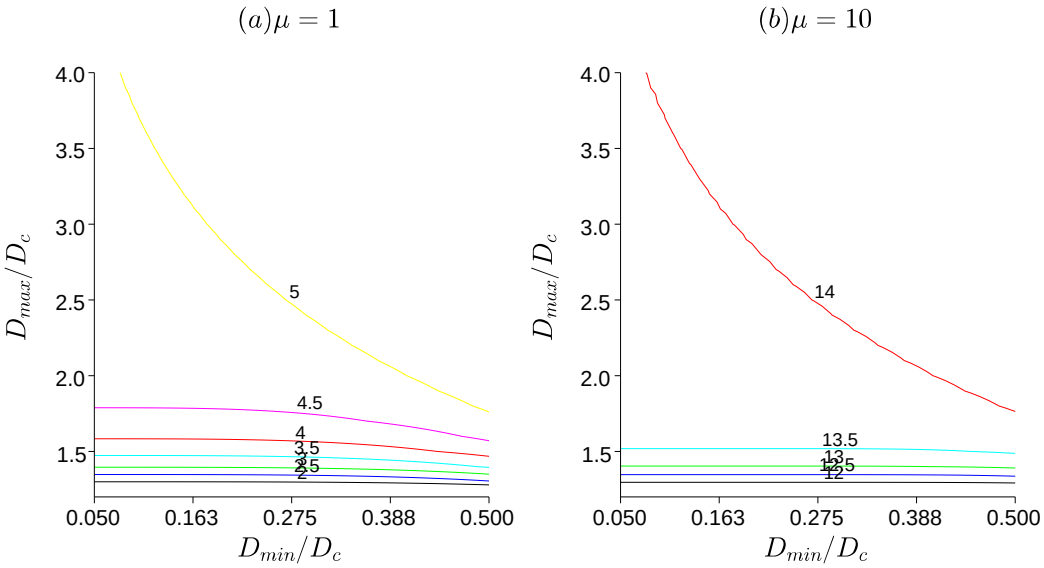

Figure 2.10: Truncation effects on the self-consistency relationship (2.29) between μ and λ. - The contours represent the values of λ for the case of (a) μ=1 and (b) μ=10.

The comparison of the μ estimated by truncated and by complete moments is illustrated in Fig.2.12. It seems that neglecting truncation effects will yield an overestimation of the μ parameter, especially for the scaled spectra with a high μ-value. As we have seen in Fig.2.9 that the truncation effect has insignificant influence on the $\mu - \lambda$ relationship, this departure should be explained by the truncated moment relationship (2.28). A special evaluation in the following subsection will be addressed to compare the model performances regarding the truncated and complete DSD modes. The results

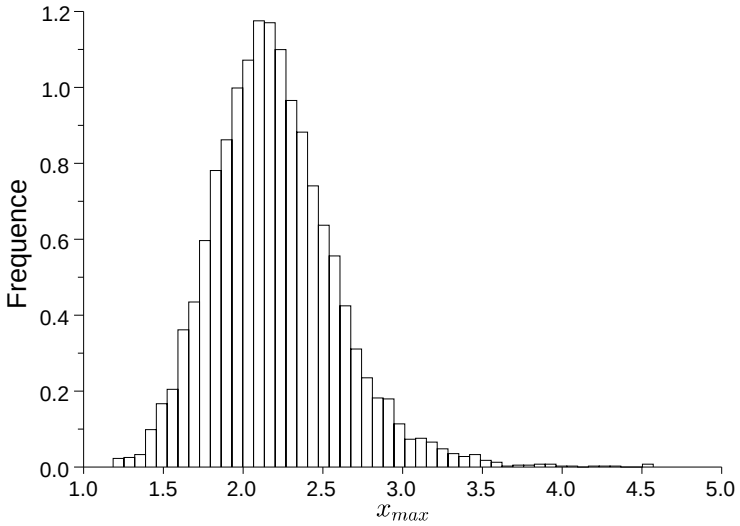

Figure 2.11: Histogram of the upper scaled diameter ($x = D_{max}/D_c$) for the 5-min DSD. - Most DSD spectra possess a upper scaled diameter between 1.5 and 3.0.

will show this distinction can be neglected in the DSD reconstitutions.

2.2.4 Evaluation of the DSD model scaled by N_t and D_c

Recent investigations made by (Cao and Zhang, 2009; Handwerker and Straub, 2011; Smith et al., 2009) showed that the errors in the estimates of the DSD parameters are usually larger when higher-order moments are employed. All of these works indicate the estimator based on M_2, M_3 and M_4 produces the smallest errors compared to other moments. Hence, we consider the classical gamma model $N(D) = N_0 D^{\mu} exp(-\lambda D)$ (Ulbrich 1983), taking into account the effect of truncation based on the 2^{nd}, 3^{rd} and 4^{th} order moments (MODTgamma234) as a reference. Table.2.2 lists the scaled DSD models associated with different estimators described in previous subsections.

Each DSD spectrum is parameterized by four formulations (Ga234T, Gx034T, Gx034, Gxall). Fig.2.13 illustrates the comparisons of the different model fits for 6 individual 5-min DSD which presents contrasting shapes. At the first sight, four models are generally well suited to represent the natural raindrop size distribution. Fig.2.13a shows a special DSD with multiple peaks. The representations of four DSD models

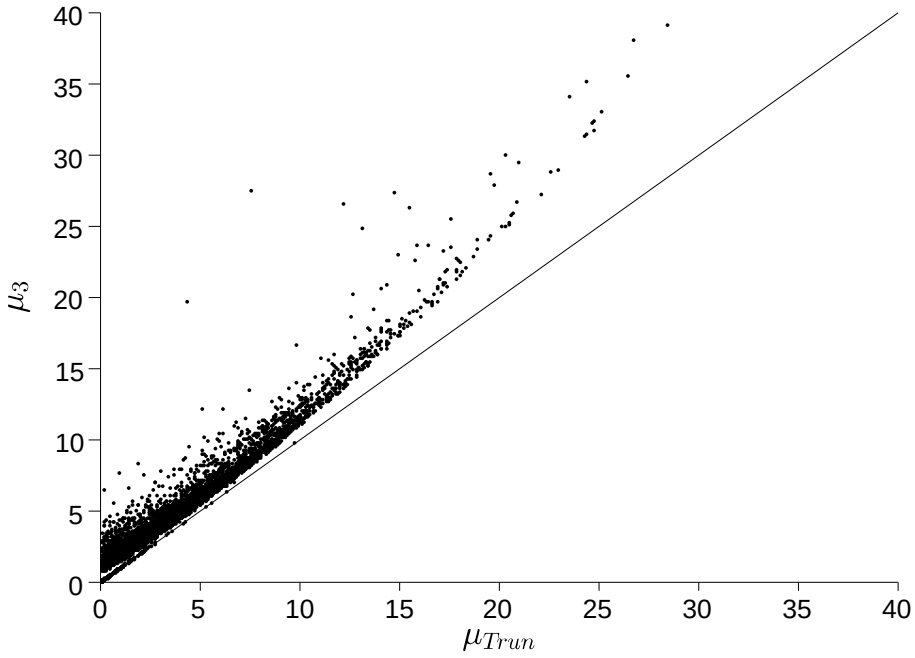

Figure 2.12: Comparison of μ estimated by the three truncated and complete moments. - This results illustrates that neglecting truncation effects will yield an overestimation of the μ parameter.

DSD formulation	Estimator	Abbreviation
Ulbrich Gamma model (1.4)	Truncated M_2 M_3 M_4	Ga234T
Scaled DSD model (2.27)	Truncated M_0 M_3 M_4	Gx034T
Scaled DSD model (2.13)	Complete M_0 M_3 M_4	Gx034
Scaled DSD model (2.13)	Complete all moments	Gxall

Table 2.2: Summary of DSD models with different estimators.

are less satisfactory for this multimodal spectrum. The consideration of the truncation effects improves the model performance for the small raindrops (Fig.2.13b and c), but produces sometimes significant errors for the large raindrops (Fig.2.13d). For the other cases (Fig.2.13e and f), the four scaling models provide similar fits. The detailed model parameters are listed in Table. 2.3. One may note that the shape parameter μ produced by Ga234T is similar to the Gx034T, which supports the fact that the shape parameter of the DSD can not be normalized by the scaling techniques. Note also that λ in the scaling formulation is different from the one in the gamma model because the latter contains the D_c. A slight overestimation of μ for the Gx034 compared to the Gx034T, confirms the results plotted in Fig.2.12. This overestimation is then slightly corrected by using all moments (Gxall) in the estimate procedure.

DSD	Ga234T			N_t	D_c	Gx034T		Gx034		Gxall	
	N_0	μ	λ			μ	λ	μ	λ	μ	λ
a	5061	-0.45	3.58	520	1.03	0.79	4.97	2.7	6.7	1.09	4.51
b	6836	1.08	2.72	669	1.86	1.38	5.36	1.92	5.92	1.67	5.58
c	8385	1.47	4.24	213	1.27	2.03	5.95	3.1	7.1	2.77	6.68
d	361502	3.06	8.14	356	0.85	3.06	6.94	5.56	9.56	5.42	9.46
e	27031153	7.64	10.4	833	1.12	7.59	11.59	8.31	12.31	7.47	11.42
f	1010	11.1	16.8	737	0.9	11.59	15.58	13.17	17.17	11.22	15.14

Table 2.3: Parameters of different DSD model fits for 6 individual 5-min DSDs, which are showed in Fig.2.13

Based on all 5-min DSD dataset, the global performance of the DSD scaling models is assessed by two criteria (bias and correlation coefficient) calculated between the measured and modeled DSD spectra, defined as,

$$bias = \frac{\overline{N(D)}_{MOD}}{\overline{N(D)}_{OBS}}, \tag{2.30}$$

$$r = \frac{\sum_{i=1}^{n}(N(D)^i_{OBS} - \overline{N(D)}_{OBS})(N(D)^i_{MOD} - \overline{N(D)}_{MOD})}{\sqrt{\sum_{i=1}^{n}(N(D)^i_{OBS} - \overline{N(D)}_{OBS})^2}\sqrt{\sum_{i=1}^{n}(N(D)^i_{MOD} - \overline{N(D)}_{MOD})^2}}. \tag{2.31}$$

A common DSD evaluation problem is related to the variability of the raindrop concentrations in the various diameter classes. For most DSDs, the small raindrops account for a large number of total raindrops. As a result, a global statistical assessment of DSD

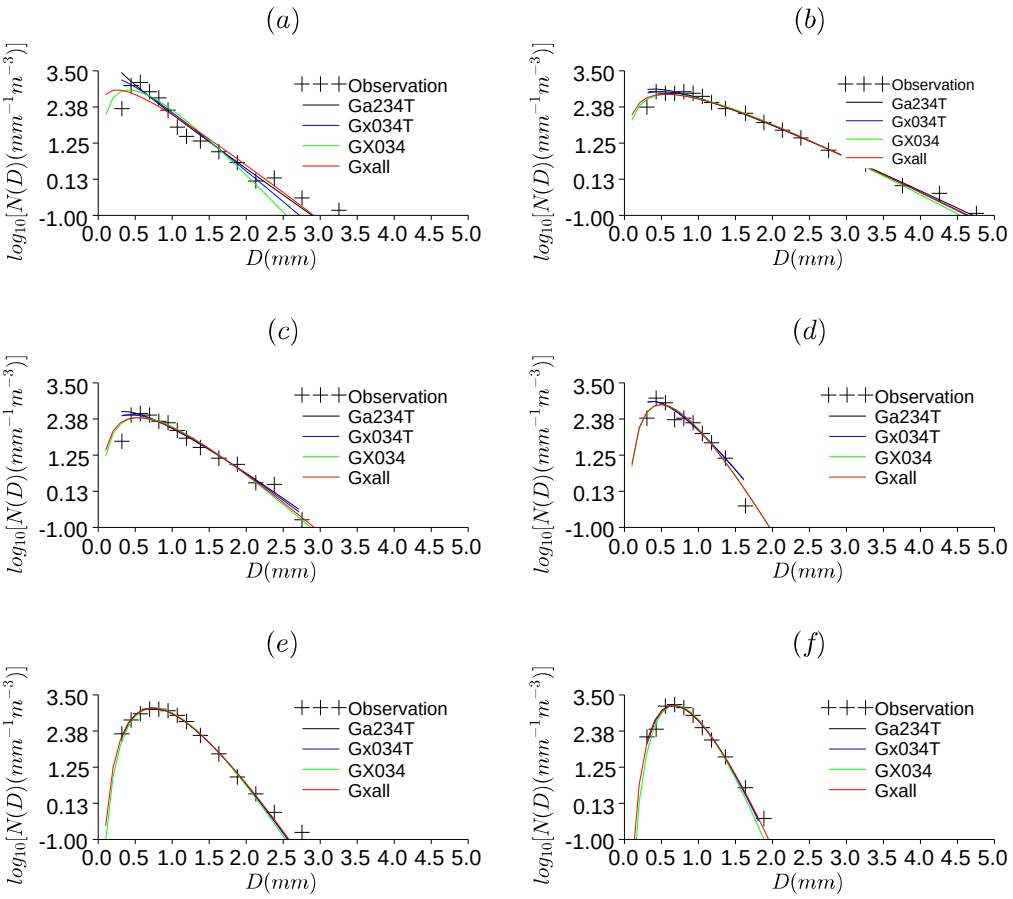

Figure 2.13: Comparisons of modeled DSDs derived from different estimators to the observations. - Six individual DSDs observations are separately fitted by different models, showed in (a) to (f).

spectra will be significantly influenced by small drops. In order to avoid this impact, the assessment procedure is performed as a function of the drop diameters. Raindrops belonging to each diameter-size interval are separately evaluated.

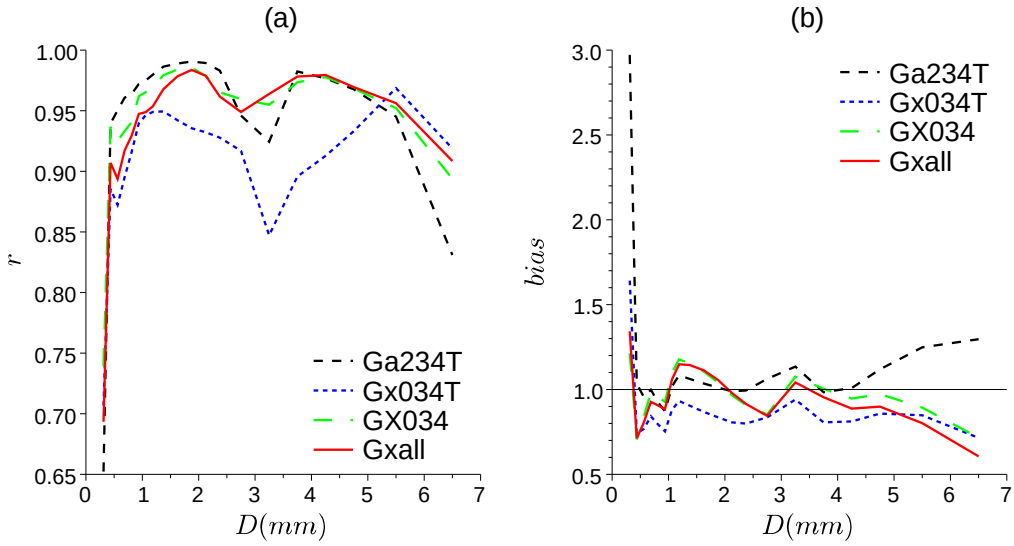

Figure 2.14: Evaluation of different DSD models by $N(D)$. - The correlation coefficient in (a) and bias in (b) between modeled and observed DSDs are illustrated as function of diameter (D) for different models.

Fig.2.14 shows that Gxall and Gx034 have a similar performance compared to Ga234T. The raindrops with the diameter between 1.5 mm and 4.5 mm are well reconstituted by these two models. However, all four models produce large bias for the small raindrops (D<0.4 mm). This bias can be slightly reduced by the introduction of the M_0 in the scaling formulations (Green line). But it is worth mentioned that this improvement does not really make sense due to the instrumental uncertainty for the tiny raindrops. For the middle-diameter drops (0.4 $mm < D <$5 mm), the truncated scaling formulation Gx034T produces a significant underestimation with a relative poor correlation coefficient, while the other models yield better performances. These results imply that the scaling formulation Gx034 is good enough to represent the natural variation in the DSD.

The estimation of the DSD moments provides an alternative way to assess the DSD formulations. If the analytical expression is a good approximation of natural DSD spec-

tra, its derived moment relationship should be able to reconstitute the different DSD moments. As a further assessment of the proposed DSD models for each 5-minute spectrum, we present in Table.2.5 and 2.4, the bias and the correlation coefficient (similar to the definition in (2.30) and (2.31)) calculated between the observed and reconstituted moments (from 0 to 6) according to the four DSD models. The moment reconstituted relationships can be derived from (2.14) for complete moment consideration, and from (2.28) for truncated moment consideration. Before the evaluation, some spectra with the shape parameter (μ) smaller than -1 are removed from the 5-min DSD dataset to avoid the negative gamma function in the M_0 reconstitution. These spectra take up to 4.38% of total DSD spectra.

DSD formulation	M_0	M_1	M_2	M_3	M_4	M_5	M_6
Ga234T	0.9920	0.9991	1.0000	0.9999	0.9992	0.9951	0.9832
Gx034T	1	0.9984	0.9973	0.9973	0.9977	0.9972	0.9924
Gx034	1	0.9980	0.9995	1.0000	1.0000	0.9995	0.9952
Gxall	1	0.9947	0.9968	0.9994	0.9998	0.9997	0.9987

Table 2.4: Correlation coefficients between the observed moments and the estimated moments based on different DSD formulation.

DSD formulation	M_0	M_1	M_2	M_3	M_4	M_5	M_6
Ga234T	1.0208	1.0049	0.9994	0.9991	0.9969	0.9897	0.9776
Gx034T	1	0.9980	1.0013	1.0053	1.0054	1.0022	0.9981
Gx034	1	0.9897	1.0084	1.0192	1.0170	1.0194	1.0574
Gxall	1	0.9792	0.9866	1.0011	0.9997	0.9926	1.0028

Table 2.5: Bias between the observed moments and the estimated moments based on different DSD formulation.

Fig.2.15 illustrates the comparison of the criteria listed in Table.2.5 and 2.4. We note that, due to the fitting technique, the calibrated moments which are used to adjust the models are well reconstituted. The truncated scaling DSD formulation fitted by 3 moments (Gx034T) produces the best performance in bias, but a poor score in correlation coefficient. Similar to the previous evaluation, the complete moment model Gx034 yields a performance as good as the truncated one. Its correlation coefficients remain high for all the DSD moments. A slight bias is found for high moments (6% for

the 6^{th} moment). This error is probably linked to the truncation effect. Nevertheless, based on the evaluations showed in Fig.2.14 and 2.15 for the purpose of simplicity of the calculation, the scaling model based on the complete moments is selected to study the microphysical characteristics of Mediterranean rainfalls in the following study.

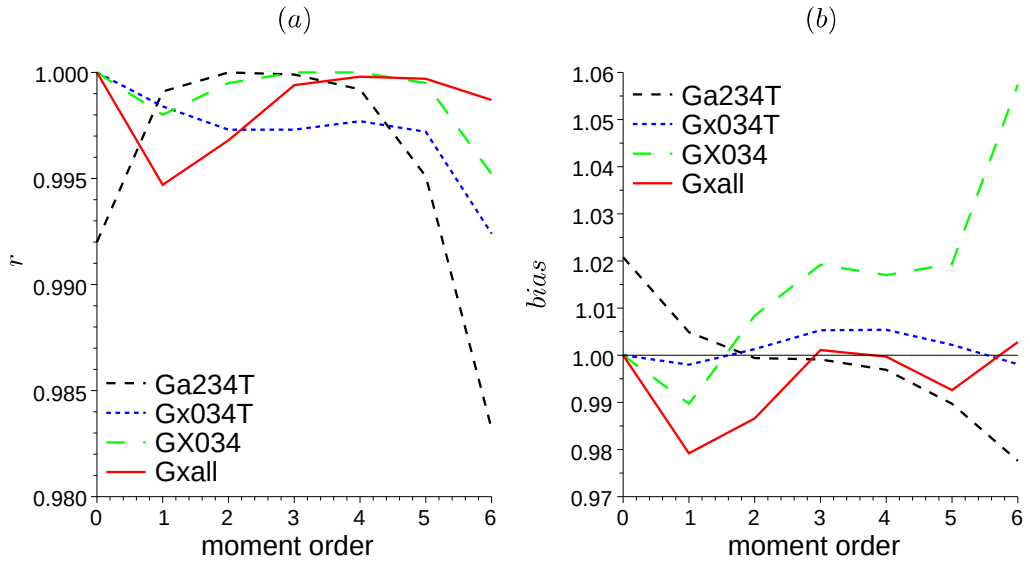

Figure 2.15: Evaluation of different DSD models by moments. - The correlation coefficient in (a) and bias in (b) between modeled and observed DSD moments (from 0^{th} to 6^{th}) are illustrated for different models.

2.2.5 Climatological characteristics of the DSD

The previous discussion showed a good performance of the scaling DSD formulation (2.13) fitted by M_0, M_3 and M_4. Based on this model, an overview of the climatological characteristics of the 5-min DSD spectra observed in the Cévennes-Vivarais region is addressed in this subsection.

For the whole observed DSD, the maximum 5-min rainfall intensity reached 132.2 mmh^{-1}. The DSD spectra with rain intensity less than 5 mmh^{-1}, 10 mmh^{-1} and 20 mmh^{-1} take up to 79.51%, 91.32% and 96.73% of total DSD spectra, respectively. The averaged rain intensity for the 5-min DSD spectra is 4.15 mmh^{-1}. A histogram of rain intensity is showed in Fig.2.16. It should be noted that theses statistic rain intensity values depend significantly on the rain filter (0.5 mmh^{-1}) described in Section 1.3.2.

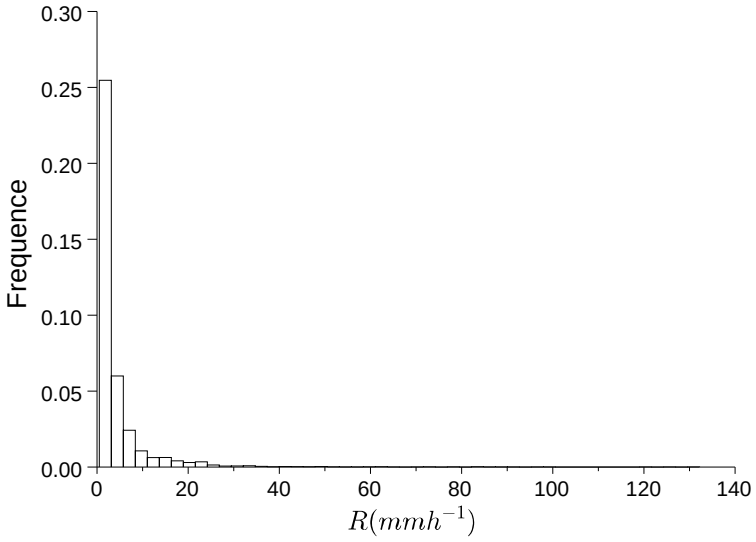

Figure 2.16: Histogram of the rain intensity derived from the 5-min DSD measured at Alès. - Whole 5-min DSDs are used to obtained the Histogram of the R.

Fig.2.17 shows the averaged spectra as function of the rain intensity. Except for the DSDs with high rain intensity values, most averaged 5-min DSD spectra possess the form of the "gamma" function. The peaks of the distributions are found around D=0.5 mm. The high-intensity DSDs are characterized by a broad distribution with large raindrops. In fact, the contribution of the tiny raindrops to the rain intensity is relatively small regardless their large numbers. Fig.2.18 shows the percentages of the contributions to the cumulative rainfall and radar reflectivity factor as a function of the drop diameter. The rain intensity depends clearly on the number of the middle-size raindrops (between 1 and 2 mm), while the radar reflectivity factor is mainly contributed by the large raindrops (between 2 and 4 mm). Therefore, the climatological Z-R relationship reflects the fact that some intrinsic relationships should exist between the middle and large size raindrops.

Each 5-min DSD is parameterized by the scaling DSD formulation (2.13) with M_0, M_3 and M_4. Three parameters (N_t, D_c and μ) are then used to study the DSD climatological characteristics.

Fig.(2.19) and Fig.(2.20) show the histograms of the concentration (N_t) and the

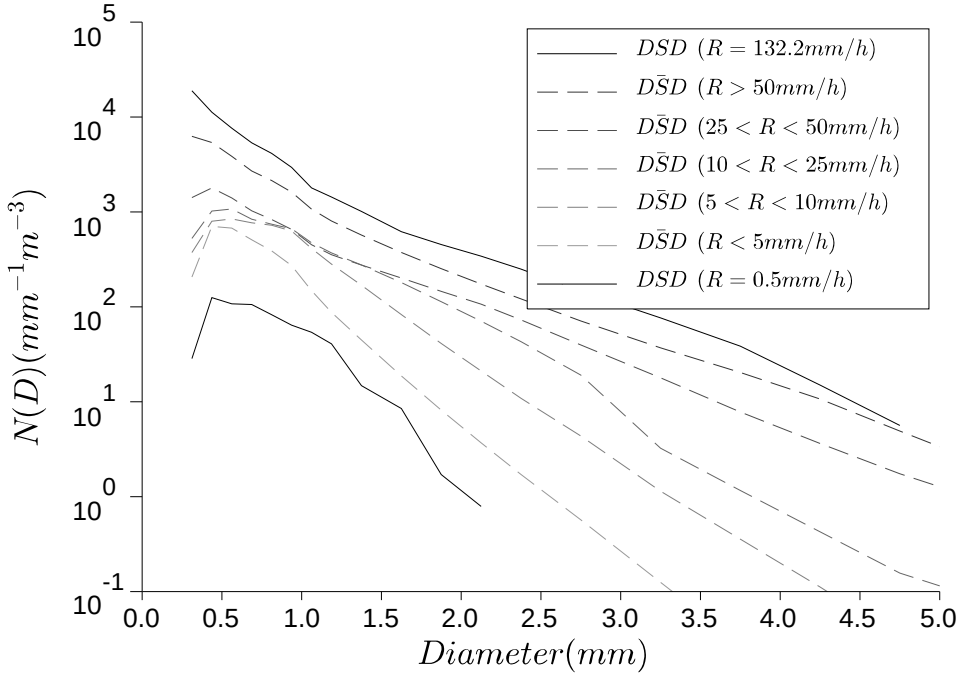

Figure 2.17: Averaged 5-min DSD as a function of the rainfall intensity. - The figure shows the average 5-minute DSD spectra for various rain rate classes (dashed lines), and two individual DSD spectra with the maximum (132.2 $mm\ h^{-1}$) and the minimum (0.5 $mm\ h^{-1}$) rain rate.

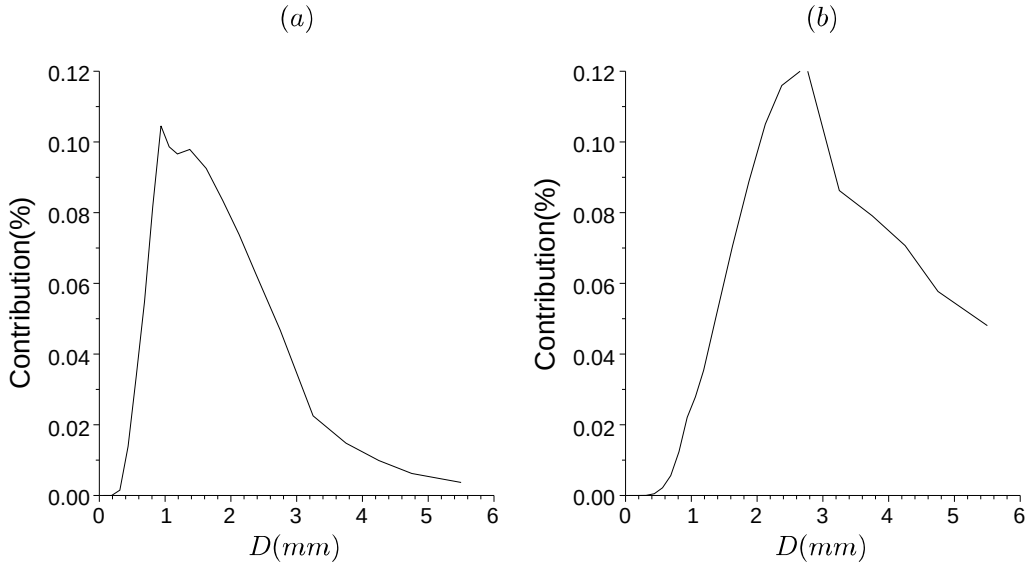

Figure 2.18: Percentages of the contributions to the cumulative rainfall depth and radar reflectivity factor. - The contributions to the R in (a), and Z in (b), are illustrated as a function of the drop diameter D.

characteristic diameter (D_c) derived from the 5-min DSD dataset. For most of the 5-min samples, the number of raindrops is less than 1000 m^{-3} with characteristic diameters ($D_c = M_4/M_3$) between 1.0 and 1.5 mm. The averaged concentration and characteristic diameter is 486 m^{-3} and 1.33 mm, respectively. The very large value of D_c (D_c >4 mm, taking up 0.3% of total DSDs) corresponds to the discontinued or multiple peaks spectra, which cannot be well parameterized by the scaling DSD formulation (2.13).

Fig.(2.21) shows the histograms of μ derived from the estimator (2.20). The distribution is positively skewed, containing a mode of μ equal to 2.5, and a limited fraction of negative (5%) and high μ-values (less than 15% for μ >10). The mode of histogram suggests that most of the 5-min scaled DSDs possess the gamma function shape, rather than the exponential distribution. The variation in shape parameter is still large after the scaling procedure. In order to understand the variation in N_t, D_c and μ, a physical interpretation of these parameters is further needed to be clarified.

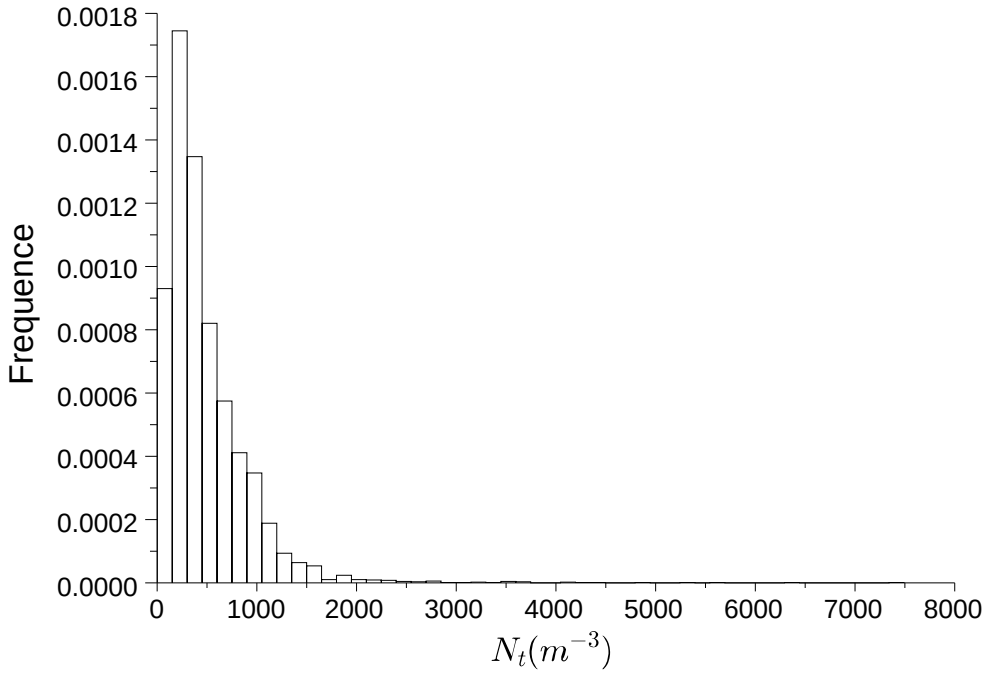

Figure 2.19: Histogram of the concentration (N_t) derived from the all 5-min DSD dataset. - The concentration is equal to the 0^{th} moment.

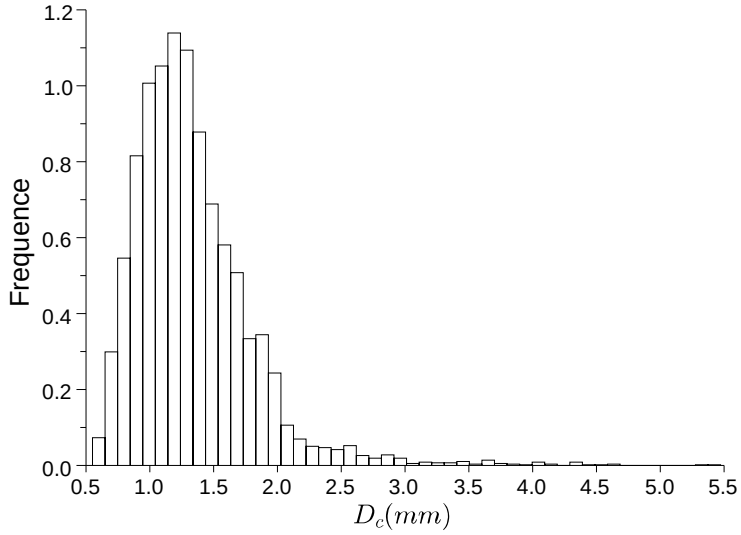

Figure 2.20: Histogram of the characteristic diameter (D_c) derived from the all 5-min DSD dataset. - The characteristic diameter is equal to the ratio of 4^{th} to 3^{rd} DSD moment.

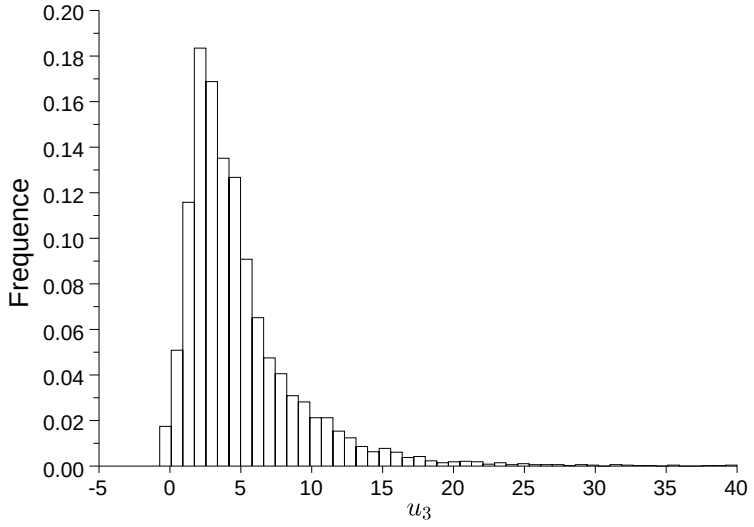

Figure 2.21: Histogram of shape parameter (μ) derived from the all 5-min DSD dataset. - The estimator (2.20) is applied on each 5-min DSD spectra to obtain a μ value.

2.3 Interpretation of parameters in the DSD formulation scaled by N_t and D_c

2.3.1 Interpretation of parameters

The DSD scaling formulation (2.13) contains three parameters (N_t, D_c and μ). The concentration (N_t) describes the number of raindrops present in a unit air volume. It is equal to the 0^{th} moment of the DSD. The variation in the concentration depends largely on the number of small drops. Many microphysical processes, such as break-up, coalescence, have direct impacts on the concentration. The concept of the number-controlled rainfall situation was well documented by Uijlenhoet et al. (2003a). In this case, the DSDs variation is totally controlled by the drop concentration, while the other parameters are constant.

The characteristic diameter (D_c) is defined by the ratio of the 4^{th} to the 3^{rd} DSD moment. Compared to the averaged diameter (D_0) defined by the ratio of the 1^{st} to the 0^{th} DSD moment, D_c is more sensitive to the middle and large raindrops. It is hoped that D_c is less influenced by the instrument uncertainty in the measurement of small drops. Fig.2.22 plots the characteristic diameters (D_c) versus the averaged diameters (D_0). It can be seen that the characteristic diameter is systematically larger than the averaged diameter. In fact, this distinction can be explained by the moment relationship (2.14). Taking the expression of D_0, a theoretical relationship is written as

$$\frac{D_c}{D_0} = \frac{\mu + 4}{\mu + 1}. \tag{2.32}$$

Hence, the relationships between the D_c and D_0 are principally controlled by the parameter μ which describes the variation of the shape in the scaled DSD. In the case of a scaled DSD spectrum following the exponential function (μ=0), D_c is theoretically four times greater than D_0. In the case of the scaled DSD spectrum following the extreme gamma function ($\mu = \infty$), the value of D_c is the same as D_0. One can note that the scatter showed in Fig.2.22 is limited by these two extreme situations.

The dimensionless μ is a shape parameter which is linked to the intercept of the scaled distribution (λ) by a self-consistency relationship. Taking the expression of the scaled gamma distribution model (2.10), one can write the mean ($mean_g$) and standard

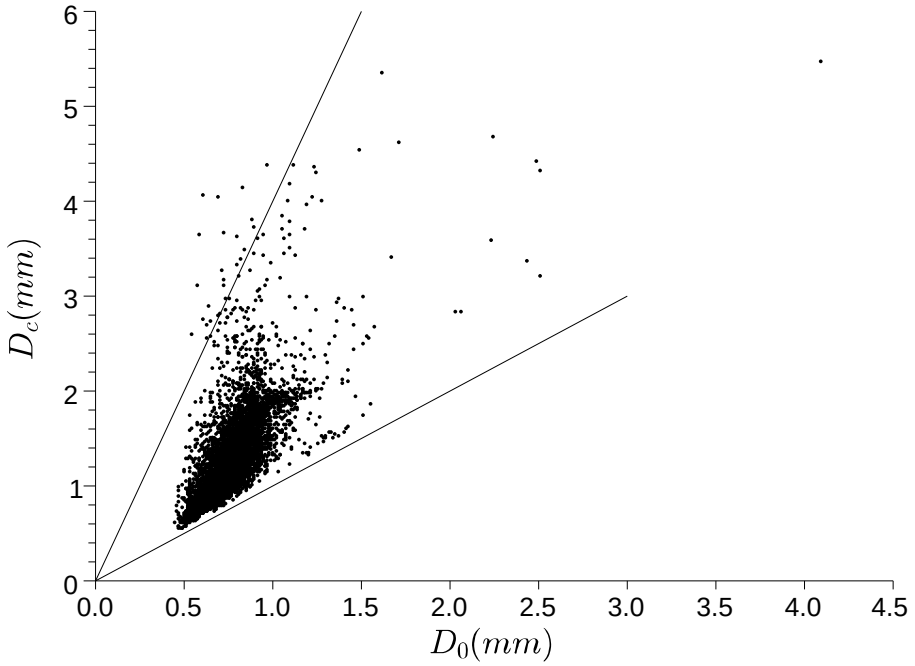

Figure 2.22: Relationship between the characteristic diameters (D_c) and the averaged diameters (D_0). - Two solid lines represent $D_c = D_0$ and $D_c = 4D_0$

deviation (σ_g) for a determined DSD as

$$mean_g = \frac{1+\mu}{\lambda}, \tag{2.33}$$

$$\sigma_g = \frac{(1+\mu)^{0.5}}{\lambda}. \tag{2.34}$$

From a statistic point of view, the shape parameter μ is associated with the coefficient of variation (CV), which is a normalized measure of dispersion of the scaled distribution, expressed as

$$CV_g = \frac{\sigma_g}{mean_g} = (1+\mu)^{-0.5}. \tag{2.35}$$

For example, the standard deviation of an exponential distribution (μ=0) is equal to its mean, thus its coefficient of variation (CV) is always equal to 1. The shape parameter reflects the combination of the mean value and standard deviation of scaled distribution. A large value of μ indicates a narrow scaled distribution with a large averaged diameter, while the small or negative shape parameter suggests usually a broad scaled distribution with a large number of small drops. And the self-consistency relationship (2.17) reflects the instinct constraint between mean and standard deviation of the scaled DSD.

2.3.2 Links between scaling DSD formulation and the classical gamma model

To obtain some further idea of the parameter interpretations, the comparison between the classical gamma model $N(D) = N_0 D^{\mu} exp(-\lambda D)$ proposed by Ulbrich (1983) and the scaling formulation will be discussed. Replacing N_0 by the concentration in the classical gamma model yields

$$N(D) = N_t \frac{\lambda_g^{\mu_g+1}}{\Gamma(\mu_g+1)} D^{\mu_g} exp(-\lambda_g D). \tag{2.36}$$

The subscript "g" is used to distinguish the parameters of the classical gamma models and those of the scaling formulation. Assuming that $\lambda_g = \lambda/D_c$ and $\mu_g = \mu$, one obtains the same expression as the scaling formulation (2.13). This implies the shape parameter in the scaling formulation is the same as that in the gamma function. However, the introduction of the characteristic diameter (D_c) in the DSD formulation switches the intercept parameter (λ_g) into a dimensionless parameter (λ), which is linked to the shape parameter (μ) by a simple self-consistency relationship.

Another advantage of reforming the gamma function by the scaling formulation (2.13) will be shown in the next chapter: the scaling formulation (2.13) can be easily extended to the generic DSD formulations scaled by any DSD moment(s), based on the same probability density function representing the general scaled distribution. This framework can provide a comparison between general distributions scaled by different moment(s) and a better understanding of the variation in the scaled distribution.

Chapter 3

Practical DSD formulations based on scaling technique

As we have demonstrated in the previous chapter, the gamma probability density function (*pdf*) with three DSD parameters (concentration, characteristic diameter and the shape parameter) is suitable to model each individual scaling DSD spectra. A complication comes from the fact that the concentration (N_t) and the characteristic diameter (D_c) can only be measured by the disdrometer at ground level, while other DSD moments (e.g. rain rate, radar reflectivity factor etc.) can be measured with a variety of in situ (e.g. raingauge) and remote sensing instruments (e.g. weather radar) over much wider spatial and temporal domains and scales. It is the purpose of the present study is to extend the scaling DSD model proposed in the previous chapter to a generic DSD model scaled by any one or two "measurable" moment(s), also termed as predictor moments in the following. Hence, this chapter is devoted to construct a bridge linking purely DSD formulation study to operational hydro-meteorological applications.

3.1 Two-moment scaling DSD formulation

3.1.1 Formulation

In order to construct the two-moment scaling DSD formulation, the concentration (N_t) and the characteristic diameter (D_c) are expressed as double power-law relationships of the predictor moments M_i and M_j, with:

$$N_t = C_{ij} M_i^{\alpha_i} M_j^{\alpha_j}, \tag{3.1}$$

$$D_c = K_{ij} M_i^{\beta_i} M_j^{\beta_j}. \tag{3.2}$$

Replacing N_t and D_c in the scaling DSD formulation (2.13) by the above power-law relationships yields the expression of the two-moment scaling DSD formulation as,

$$N(D) = \frac{C_{ij} M_i^{\alpha_i} M_j^{\alpha_j}}{K_{ij} M_i^{\beta_i} M_j^{\beta_j}} \frac{\lambda^{\mu+1}}{\Gamma(\mu+1)} (\frac{D}{K_{ij} M_i^{\beta_i} M_j^{\beta_j}})^{\mu} exp(-\lambda \frac{D}{K_{ij} M_i^{\beta_i} M_j^{\beta_j}}). \tag{3.3}$$

Integrating the two-moment scaling formulation (3.3) with respect to D^k, one obtains the expression of the k^{th} order moment expression:

$$M_k = \frac{\Gamma(\mu+k+1)}{\Gamma(\mu+1)} C_{ij} K_{ij}^k \frac{M_i^{\alpha_i + k\beta_i} M_j^{\alpha_j + k\beta_j}}{\lambda^k}. \tag{3.4}$$

There are 8 parameters in the two-moment scaling formulation (3.3). However, these parameters are not totally independent. In an analogous manner as Chapter 2, setting $k = i$ and $k = j$ in (3.4), one obtains the following six self-consistency relationships to reduce the number of parameters in the DSD formulation (3.3):

$$\alpha_i + i\beta_i = 1, \tag{3.5}$$

$$\alpha_j + i\beta_j = 0, \tag{3.6}$$

$$\alpha_i + j\beta_i = 0, \tag{3.7}$$

$$\alpha_j + j\beta_j = 1, \tag{3.8}$$

$$\frac{\Gamma(\mu+i+1)}{\Gamma(\mu+1)} C_{ij} (\frac{K_{ij}}{\lambda})^i = 1, \tag{3.9}$$

$$\frac{\Gamma(\mu+j+1)}{\Gamma(\mu+1)} C_{ij} (\frac{K_{ij}}{\lambda})^j = 1. \tag{3.10}$$

Through (3.5) – (3.8), an interesting feature of the two-moment scaling DSD formulation can be obtained as already demonstrated by Lee et al. (2004): the exponents of the double power-law models only depend on the predictor moment orders, with:

$$\alpha_i = -\frac{j}{i-j} \tag{3.11}$$

$$\alpha_j = \frac{i}{i-j} \tag{3.12}$$

$$\beta_i = \frac{1}{i-j} \tag{3.13}$$

$$\beta_j = -\frac{1}{i-j} \tag{3.14}$$

Expression of the ratio M_4 to M_3 as a function of the predictor moments M_3 and M_4 using (3.4) yields the seventh self-consistency constraint $\lambda = \mu + 4$, identical to that mentioned in (2.17). As a consequence, only one free parameter remains to be estimated in the two-moment scaling formulation.

3.1.2 Parameter estimation procedure

In theory, the free parameter can be easily estimated either from the regression (3.1) or (3.2). Application of such regressions linking the predictor moments (M_i and M_j) into the explanatory variables (N_t and D_c) makes the main difference on the scaling formulations presented in previous and current chapter. In contrast to the DSD scaling model developed in Chapter 2, which parameterizes each individual DSD, the two-moment scaling DSD formulation (3.3) is applied over a series of DSD spectra. In the current study, the whole 5-min DSD data are used to estimate a climatological parameter for the two-moment scaling DSD formulation.

As mentioned before, only one regression relationship is required to determine the scaling DSD formulation. The choice of the relationship (3.1) or (3.2) depends on the quality of the regressions. Fig. 3-1 shows a first plot of concentration against the combination of M_3 and M_6, and a second plot of concentration against the combination of rain rate (R) and reflectivity factor (M_6). Below these two figures, Fig. 3-2 shows the relationships between the combinations of predictor moments and the characteristic diameter (D_c). Because of the uncertainty in the measurement of N_t and the poor relationship between the concentration (N_t) and the predictor moments (R and M_6),

the regression based on the characteristic diameter (3.2) is selected in the estimation procedure to obtain K_{ij}. The other parameters, such as C_{ij}, λ and μ, can be easily determined using the self-consistency relationships (3.9), (3.10) and (2.17).

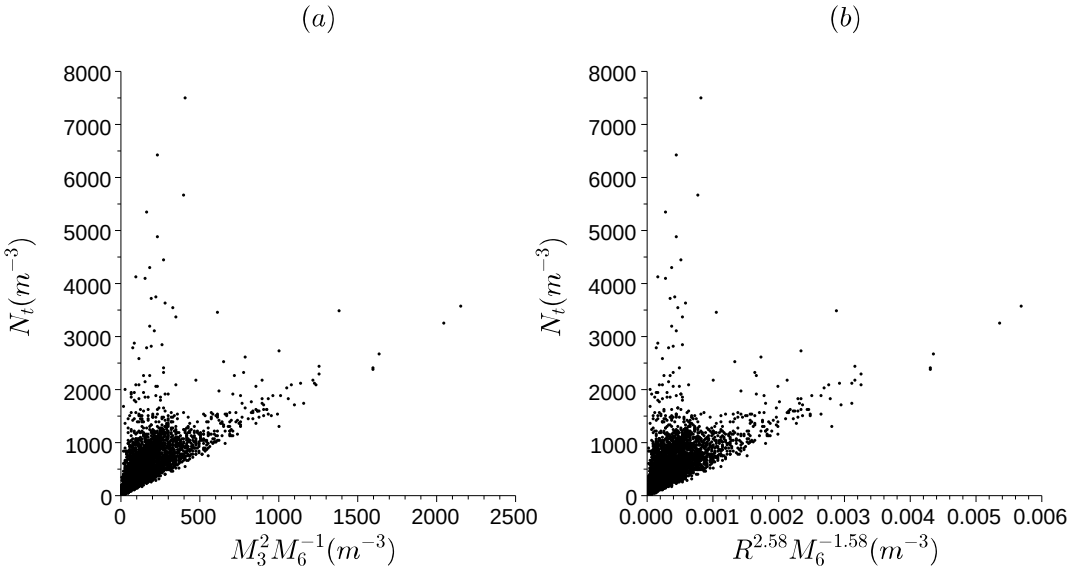

Figure 3.1: Relationship between the concentration and the predictor moments - Poor relationships are showed between the concentration and the combination of M_3-M_6 in (a); between the concentration and the combination of R-M_6 in (b).

In an analogous manner as Chapter 2, an estimation method using all DSD moments is proposed to compare with the result obtained from the regression. The estimate procedure is the following:

- We firstly establish the multiple power-law relationships $M_k = a_{ijk} M_i^{b_{ki}} M_j^{b_{kj}}$ based on (3.4), between all moments M_k (k=0 to 6) and predictor moments Mi, M_j by forcing the exponent b_{ki} and b_{kj} equal to appropriate values through (3.11) - (3.14).

- With the self-consistency relationship (2.17) and the moment expression 3.4, we can determine the values of K_{ij}, λ and μ from a linear regression analysis on the ratio of consecutive coefficients $a_{ij,k+1}$ and $a_{ij,k}$, as a function of k

$$\theta_k = \frac{a_{ij,k+1}}{a_{ij,k}} = (\mu + 1)\frac{K_{ij}}{\lambda} + k\frac{K_{ij}}{\lambda}. \tag{3.15}$$

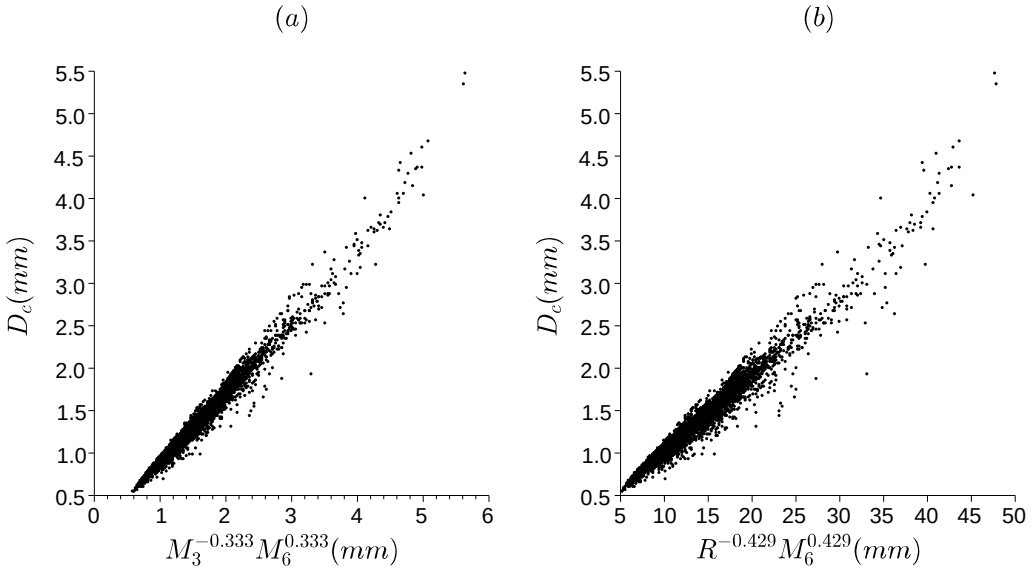

Figure 3.2: Relationship between the characteristic diameter and the predictor moments - Good relationships are showed between the characteristic diameter and the combination of M_3-M_6 in (a); between the characteristic diameter and the combination of R-M_6 in (b).

- C_{ij} can then be determined either by the self-consistency relationship (3.9) or by (3.10). This step allows us to verify our theory by the comparison of the C_{ij} values derived from the 2 different self-consistency relationships.

Fig.3.3 demonstrates the relationship between the ratio of consecutive coefficients ($a_{ij,k+1}/a_{ij,k}$) as a function of order (k) for the DSD formulation scaled by the rain intensity (R) and reflectivity factor (Z). A linear relationship agreeing well to the theory (3.15) is obtained. The K_{ij}, λ and μ are then determined by the intercept and slope together with the self-consistency relation (2.17).

The parameter values estimated by the regression (3.2) and by all moments using (3.15) are listed in Table.3.1. For the reason of simplicity, $M_{3.67}$ ($mm^{3.67}m^{-3}$) instead of rain intensity (R: mm/h) is used as the predictor moment for the following studies. A simple linear relationship between the $M_{3.67}$ and R is

$$M_{3.67} = R/0.0071251. \tag{3.16}$$

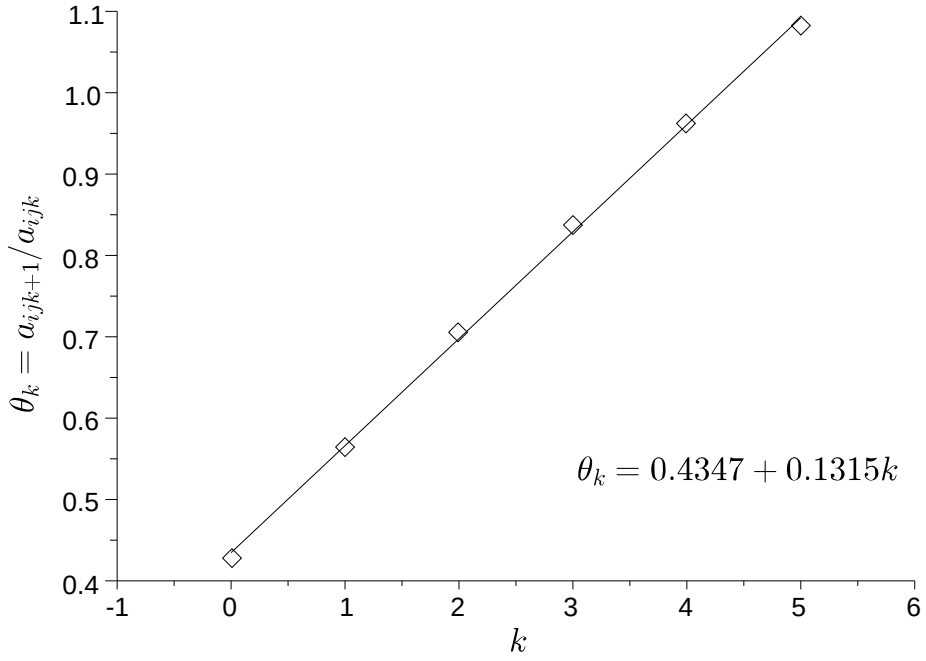

Figure 3.3: Linear relationship between the ratio of consecutive coefficients ($a_{ij,k+1}/a_{ij,k}$) and the order k. - The slope and intercept are used to estimate parameters in the two-moment scaling DSD formulation.

Estimators	α_i	α_j	β_i	β_j	C_{ij}	C^*_{ij}	K_{ij}	μ	λ
(3.2)	2.575	-1.575	-0.429	0.429	6.457		0.831	2.439	6.439
(3.15)	2.575	-1.575	-0.429	0.429	6.720	6.698	0.829	2.306	6.305

Table 3.1: Parameters of DSD formulation scaled by ($M_{3.67}$) and radar reflectivity factor (Z) by two estimation methods. C_{ij} can then be determined either by the self-consistency relationship (3.9) or by (3.10).

Both estimation methods produce similar parameter values in the DSD formulation. The climatological shape parameter (μ) for the whole DSD series scaled by $M_{3.67}$ and M_6 is around 2.4, which is very closed to the mode of the μ-histogram for the previous DSD formulation scaled by N_t and D_c. Introducing these climatological parameters (K_{ij}, C_{ij}, α_i, α_j, β_i and β_j) into (3.3) and then inversing the DSD formulation, we obtain an expression of the scaled DSD function as

$$g(x) = N(D)/\frac{C_{ij}M_i^{\alpha_i}M_j^{\alpha_j}}{K_{ij}M_i^{\beta_i}M_j^{\beta_j}} \quad with \quad x = \frac{D}{K_{ij}M_i^{\beta_i}M_j^{\beta_j}}. \tag{3.17}$$

The expression (3.17) provides the second way to illustrate the scaled distribution. Each 5-min DSD spectrum is scaled by $M_{3.67}$ and M_6 through (3.17) with the climatological values of C_{ij} and K_{ij} listed in Table.3.1. The averaged spectrum of these scaled DSDs is then plotted in Fig.3.4 to compare with the scaled distribution modeled by the gamma function with the shape values (μ). The scaled distribution derived from the regression (3.2) is shown on the left hand side and the one derived from all DSD moments (3.15) is shown on the right hand side. The two scaled distributions are very similar. The two modeled $g(x)$ are generally in good agreement with the averaged scaled spectra, except for a slight underestimation for $x < 0.5$ and overestimation for $x > 3.0$. These biases are possibly related to the measurement errors concerned with tiny rain drops, and the sampling error related to large drops. The low standard deviation indicates the good performance of scaling technique for the scaled spectra with $0.5 < x < 2.0$.

Two climatological moments relationships can be derived from equation (3.4) based on the climatological DSD parameters listed in Table.3.1,

$$M_k = \frac{2.077\Gamma(3.439+k)}{0.129^{-k}}\left(\frac{R}{7.125\times10^{-3}}\right)^{2.575-0.429k}(Z)^{-1.575+0.429k}, \tag{3.18}$$

$$M_k = \frac{2.489\Gamma(3.306+k)}{0.131^{-k}}\left(\frac{R}{7.125\times10^{-3}}\right)^{2.575-0.429k}(Z)^{-1.575+0.429k}. \tag{3.19}$$

One may note that these two DSD moments relationships are very similar. In fact, because the two estimators produce very similar parameters listed in Table.3.1, it is expected that there is no fundamental difference between the DSD models calibrated by the regression (3.2) and by all moments using (3.15).

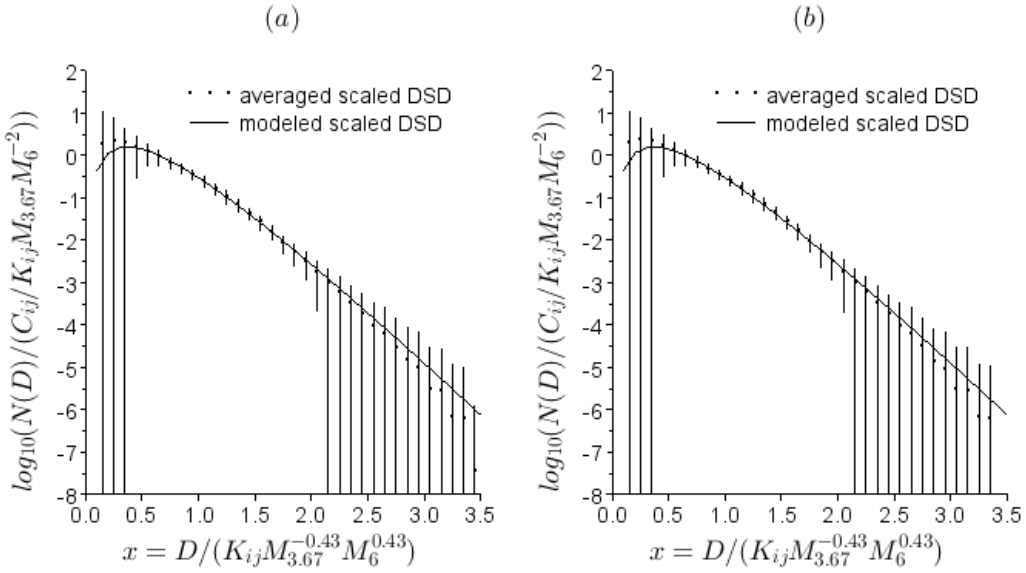

Figure 3.4: Averaged scaled distribution (points) with the DSD model scaled by $M_{3.67}$ and Z. - The models adjusted by the regression relationship (3.2) and (3.15) are illustrated in (a) and (b), respectively. The vertical bars represent the standard deviation in logarithmic scale of the scaled distribution.

3.1.3 Evaluation of the two-moment formulation

Similarly to the evaluated methods presented in Section 2.2.4, two evaluation procedures are performed in this subsection. The first evaluation is based on the comparison between the modeled and the observed DSD, while the second one is to assess the quality of reconstituted moments. A detailed description of the evaluation process can be found in Section 2.2.4.

The correlation and bias between the modeled and observed DSD are displayed in Fig.3.5. As expected, the two models have nearly the same performance. The models are well correlated with the observations for the raindrop diameter range 1 $mm < D <$5 mm. But the performance decreases rapidly for the raindrops less than 1 mm. This is explained by the fact that both the rain rate and the radar reflectivity factor are high order moments, quite insensitive to the small raindrop counts. Fig.3.6 shows the quality of reconstituted moments. The high order ($M_{3.67}$ to M_6) moments are well estimated by the scaling DSD models, while the low order moments are seriously overestimated. Comparing to the results presented in Fig.2.15, one can easily note

the difference between the DSD models scaled by R-Z, and by N_t-D_c. The latter model produces a good performance both for the low and high order moments. This result highlights the limitation of high-order moments for the estimation of low-order moments. The estimation of low order moments, sensitive to small raindrops counts, is still a challenge in the future research.

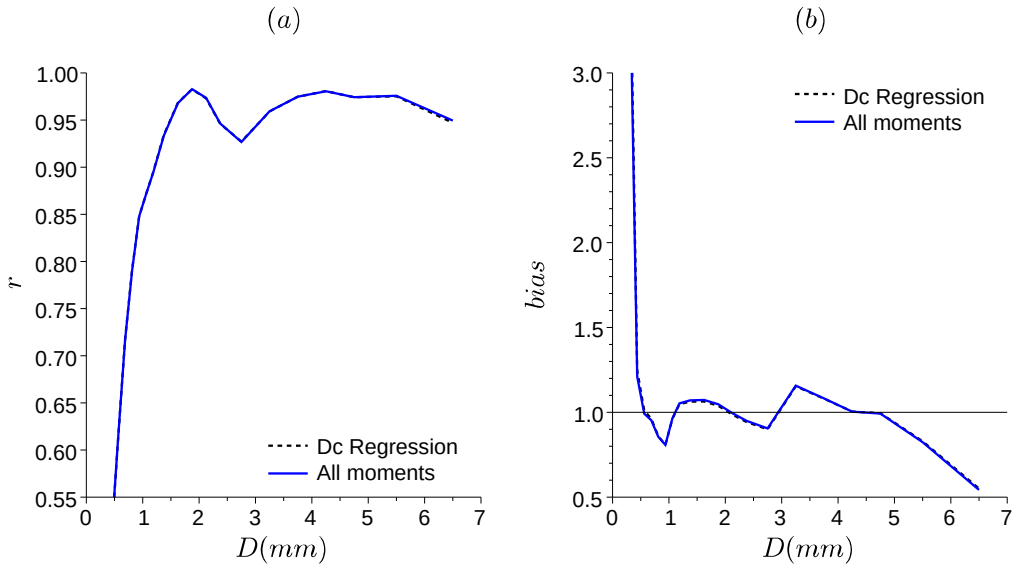

Figure 3.5: Evaluation of reconstituted DSDs based on the 2-moment ($M_{3.67}$ and M_6) DSD formulations. - Two climatological DSD models derived from different estimators are evaluated by correlation coefficient in (a) and bias in (b).

3.2 One-moment scaling DSD formulation

3.2.1 Formation

If only one DSD moment is available, the concentration (N_t) and the characteristic diameter (D_c) may be expressed as power-law relationships of the predictor moment M_i, with

$$N_t = C_i M_i^{\alpha_i}, \tag{3.20}$$

$$D_c = K_i M_i^{\beta_i}. \tag{3.21}$$

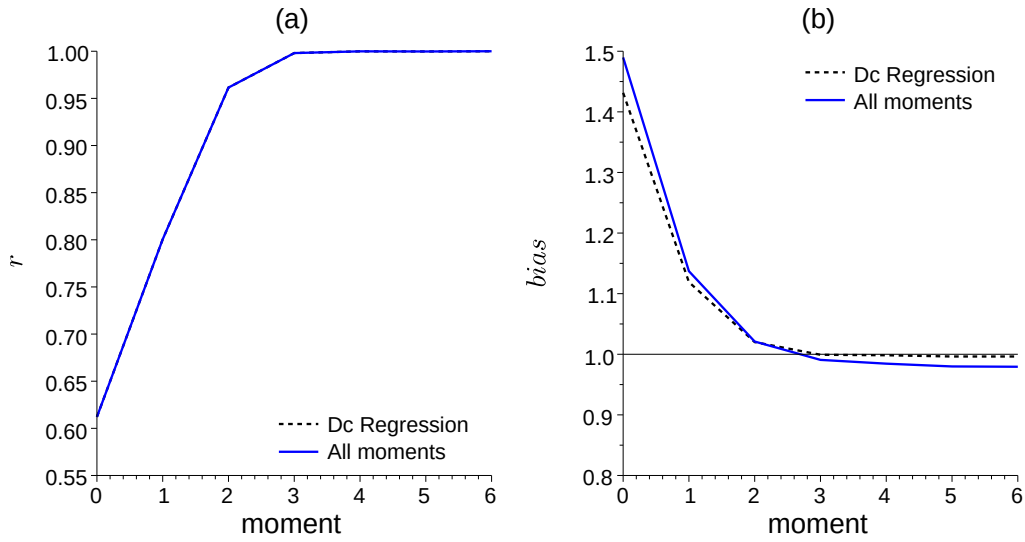

Figure 3.6: Evaluation of reconstituted moments based on the 2-moment ($M_{3.67}$ and M_6) DSD formulations. - Reconstituted moments based on two climatological DSD models are separately evaluated by correlation coefficient in (a) and bias in (b).

Similarly, replacing N_t and D_c in (2.13) by the above power-law relationships yields the one-moment scaling DSD formulation:

$$N(D) = \frac{C_i M_i^{\alpha_i}}{K_i M_i^{\beta_i}} \frac{\lambda^{\mu+1}}{\Gamma(\mu+1)} (\frac{D}{K_i M_i^{\beta_i}})^{\mu} exp(-\lambda \frac{D}{K_i M_i^{\beta_i}}) \tag{3.22}$$

Introducing the one-moment DSD formulation in the expression of the k^{th} order moment yields:

$$M_k = \frac{\Gamma(\mu+k+1)}{\Gamma(\mu+1)} C_i K_i^k \frac{M_i^{\alpha_i+k\beta_i}}{\lambda^k}. \tag{3.23}$$

There are 6 parameters in the one-moment scaling DSD formulation (3.22). By setting $k = i$ in (3.23), one obtains two self-consistency constraints as

$$\alpha_i + i\beta_i = 1, \tag{3.24}$$

$$\frac{\Gamma(\mu+i+1)}{\Gamma(\mu+1)} C_i (\frac{K_i}{\lambda})^i = 1. \tag{3.25}$$

In addition, it can be verified that the self-consistency constraint (2.17) related to the choice of the characteristic diameter (D_c) holds by the expression the ratio (M_4/M_3) as a function of the predictor M_i using (3.23). As a consequence, there are three free parameters that remain to be specified for the one-moment scaling DSD formulation.

3.2.2 Parameter estimation procedure

In order to illustrate an implementation of the one-moment scaling DSD formulation, we have chosen to consider in this section the $M_{3.67}$ or M_6, to scale the 5-min DSD spectra.

Similar to the two-moment scaling DSD formulation, a series of DSD observations are required to obtain the DSD parameters. In theory, three free DSD parameters can be obtained from the linear regression analysis (3.20) and (3.21) with respect to the log-transformed DSD moments. Fig.3.7 and Fig.3.8 show the plots of explained moments (N_t and Dc) against predictor moments ($M_{3.67}$ or M_6). As expected, the relationship between the total concentration (N_t) and the predictor moment ($M_{3.67}$ or M_6) is rather weak (Fig.3.7). It becomes even weaker in the Z-scaling case due to the poor correlation between drop concentration and the highest order moment. These results show the difficulty in estimating N_t by the commonly observed moments, such as R or Z. Hence, we propose to rely on the statistical relationship between D_c and the predictor moment (3.21) for estimating the parameters K_i and β_i, and then to rely on the self-consistency relationships for estimating C_i and α_i.

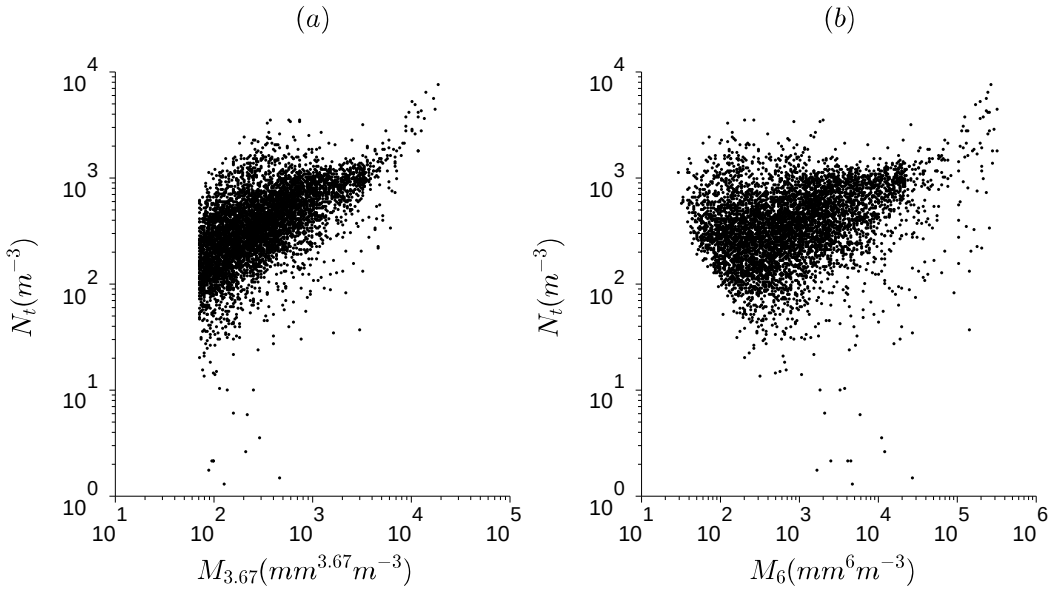

Figure 3.7: Relationships between the DSD concentration and the predictor moment. - The relationship between N_t and $M_{3.67}$ is illustrated in (a); relationship between N_t and M_6 is illustrated in (b).

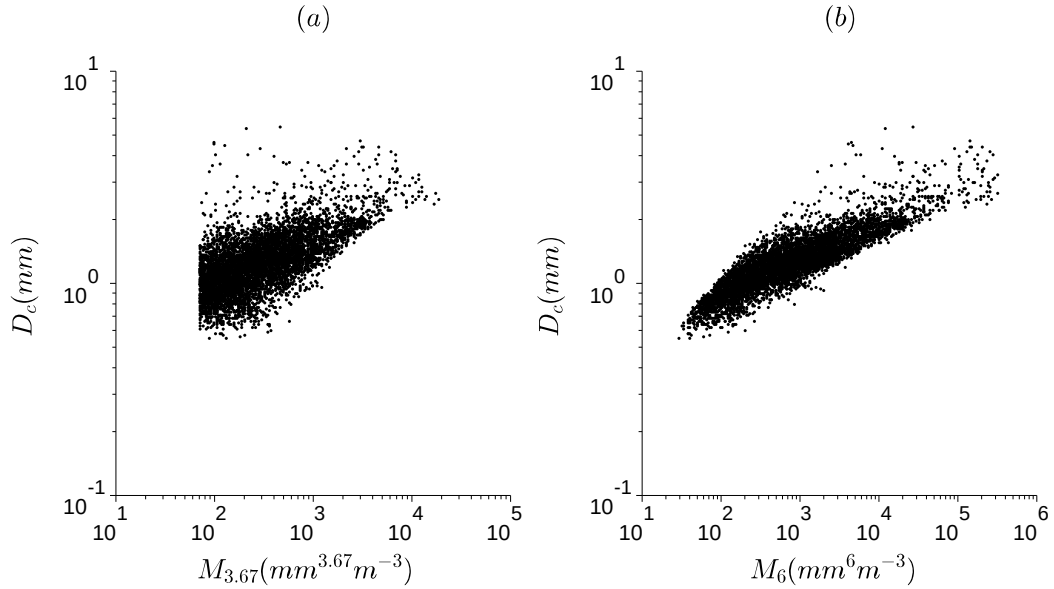

Figure 3.8: Relationships between the DSD characteristic diameter and the predictor moment. - The relationship between D_c and $M_{3.67}$ is illustrated in (a); relationship between D_c and M_6 is illustrated in (b).

In practice, K_i and β_i are determined from the regression analysis of log-transformed D_c versus the log-transformed M_i. Next, α_i can be calculated from the self-consistency relationship (3.24) and, in a third step, C_i is estimated by forcing the exponent in (3.20) to be equal to α_i. Finally, considering the self-consistency relation (2.17), μ and λ can be derived from (3.25). However, a serious shortcoming of this estimation procedure is related to the unreliable regression (3.20). To partly overcome this problem, an alternative method based on all observed DSD moments is proposed and described below:

- Establish the power law relationships $M_k = a_{ik}M^{b_{ik}}$ between all moments M_k (k=0 to 6) and the predictor moment M_i (i = 3.67 or i = 6) to derive a_{ik} and b_{ik}.

- Estimate α_i and β_i by the method proposed by Sempere Torres et al. (1998) based on the linear relationship between the exponent values b_{ik} (k=0 to 6) and moment order k.

- Through the self-consistency relationship (2.17), determine the values of K_i, λ

and μ from a linear regression analysis on the ratios of consecutive coefficients $a_{i,k+1}$ and $a_{i,k}$ following the method proposed by Hazenberg et al. (2011)

$$\theta_k = \frac{a_{i,k+1}}{a_{i,k}} = (\mu + 1)\frac{K_i}{\lambda} + k\frac{K_i}{\lambda}. \tag{3.26}$$

- Calculate the value of C_i from the self-consistency relationship (3.25).

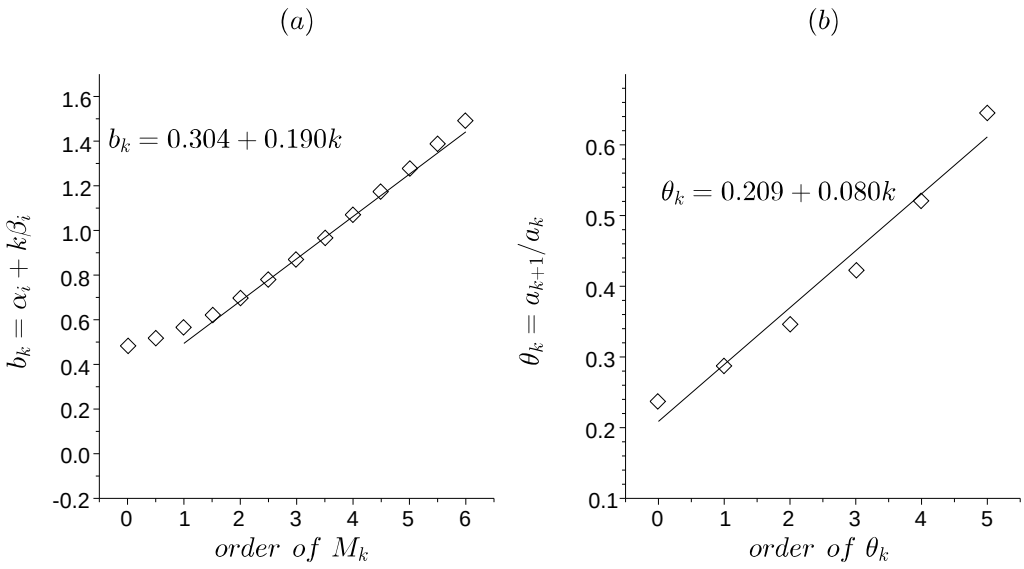

Figure 3.9: Estimation of the parameters in the DSD formulation scaled by $M_{3.67}$. - Relationship between the exponent b_i and the moment order k is showed in (a); the ratios of consecutive coefficients (θ_k) and the moment order k is showed in (b).

Fig.3.9a and 3.10a display the exponent b_{ik} as a function of the moment order k, for DSD formulations scaled by $M_{3.67}$ and M_6, respectively. In both cases, a good linear relationship is found, except for the low order moment. This is probably explained by: (i) the uncertainty associated with the measurement of small raindrops, which is essential to determine the low order moments; (ii) the inherent uncertainty in the power-law relationships ($M_k = a_{ik}M_i^{b_{ik}}$) between the low and the high order moments. Hence, the 0^{th} moment is neglected in the regression analysis to estimate

Fig.3.9b and 3.10b show the relationships between the ratios of consecutive coefficients ($\theta_k = a_{i,k+1}/a_{i,k}$) and the moment order k, for DSD formulation scaled by $M_{3.67}$ and M_6, respectively. As expected from the theoretical relationship (3.26), a linear

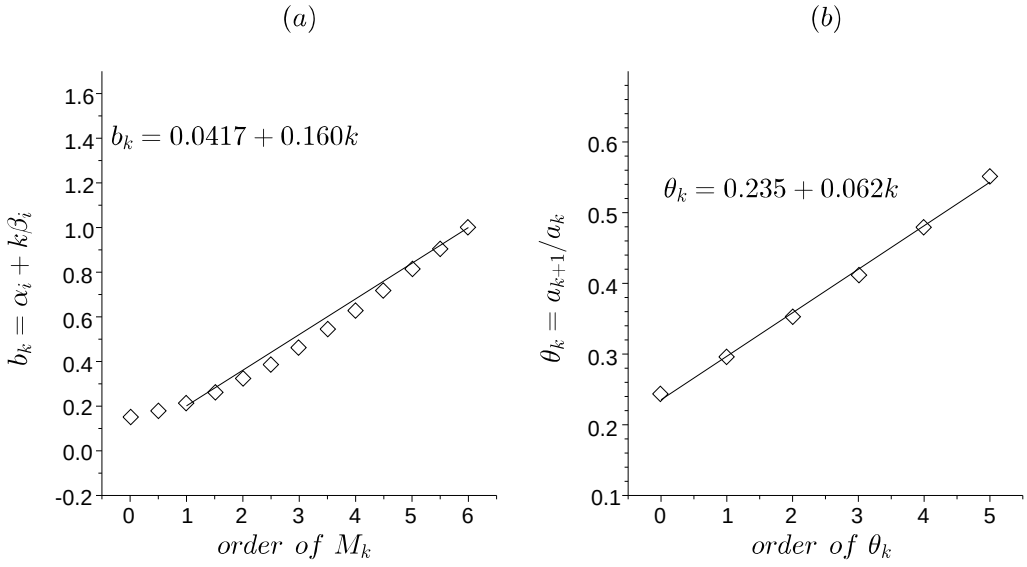

Figure 3.10: Estimation of the parameters in the DSD formulation scaled by M_6. - Relationship between the exponent b_i and the moment order k is showed in (a); the ratios of consecutive coefficients (θ_k) and the moment order k is showed in (b).

behavior is exhibited between θ_k and k. This linear relation is then used to estimate K_i, λ and μ based on the linear expression (3.26). Note that, after the estimation of α_i and β_i, the exponents b_{ik} in $M_k = a_{ik}M^{b_{ik}}$ are slightly changed. It was found numerically important to adapt the values of the coefficients a_{ik} to coincide with the shift of exponent values (b_{ik}). Once K_i, λ and μ are determined, C_i can be derived from the self-consistency relationship (3.25).

The two estimation methods (based on simple regressions (3.20) - (3.21), or on all DSD consecutive moments) are performed to obtain the climatological parameters for the DSD formulation scaled by $M_{3.67}$ and by M_6, respectively. All parameters in these formulations are listed in Table.3.2.

It seems that the choice of the estimation method has a significant influence on the shape parameter (μ). The "all moments" method produces a low shape parameter (μ=1.595) in the DSD formulation scaled by $M_{3.67}$, in opposite to a high shape parameter produced by the regression (3.20) - (3.21). On the contrary, the "all moment" produce a higher shape parameter in the DSD formulation scaled by M_6. The other parameters, such as C_i, β_i and α_i, depend more on the order of the scaling moment.

Scaling Moment	Estimators	α_i	β_i	C_i	K_i	μ	λ
$M_{3.67}$	Regression	0.271	0.199	93.84	0.405	2.266	6.266
$M_{3.67}$	All Moment	0.304	0.190	77.91	0.450	1.595	5.595
M_6	Regression	-0.0028	0.167	496.1	0.414	1.699	5.699
M_6	All Moment	0.0417	0.160	363.6	0.420	2.823	6.823

Table 3.2: Parameters of DSD formulation scaled by rain intensity (R) or radar reflectivity factor (Z) by two estimated methods.

The scaling process by high order moment yields a lower α_i and a higher C_i, compared to that scaled by low order moment.

In the same manner as the two-moment scaling formulation, we introduce the climatological parameters (K_i, C_i, β_i and α_i) into (3.22) and reform the DSD formulation to obtain the expression of the scaled distribution as,

$$g(x) = N(D)/\frac{C_i M_i^{\alpha_i}}{K_i M_i^{\beta_i}} \quad with \quad x = \frac{D}{K_i M_i^{\beta_i}}. \tag{3.27}$$

Each 5-min DSD spectrum is scaled by the predictor moment ($M_{3.67}$ or M_6) based on the expression (3.27). The averaged spectrum of these scaled DSD spectra is plotted in Fig.3.11 and Fig.3.12 for the $M_{3.67}$- and M_6-scaled DSD formulations, respectively, to compare with their modeled scaled distributions calculated from the shape parameter (μ). For each moment scaled spectrum, the scaled distributions estimated by the "simple regression" and by the "all-moments" are displayed separately. Regardless the choice of the estimation method, the $M_{3.67}$-model yields a slight overestimation for $x < 0.5$ and an underestimation for $x > 2.0$ (Fig.3.11). This bias is significantly reduced in the DSD spectra scaled by M_6, especially when the "simple regression" method is used to estimate the DSD parameters (Fig.3.12a). It seems that the choice of parameters estimator depends on which moment is used in the scaling procedure. The model scaled by $M_{3.67}$ derived from "all-moment" exhibits a slightly better performance compared to that derived from "regression", while the "regression" estimator is better than the estimator based on "all-moment" for the DSD model scaled by M_6. The detailed model performance will be evaluated in the next subsections.

Substituting the climatological DSD parameters listed in Table.3.2 into the moment relationship (3.23) yields expressions of any moment M_k as a function of R and Z, respectively. The expressions (3.28) and (3.30) are obtained based on the "regression"

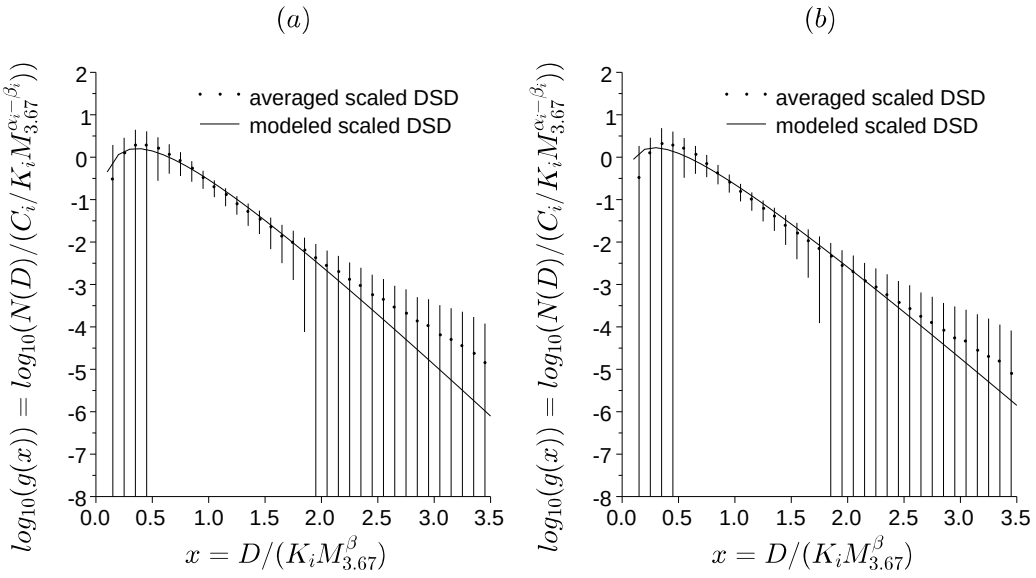

Figure 3.11: Averaged scaled distribution (points) with the DSD model scaled by $M_{3.67}$. - The models adjusted by the regression relationships and by "all-moment" are showed in (a) and (b), respectively. The bars represent the standard deviation of the scaled distributions.

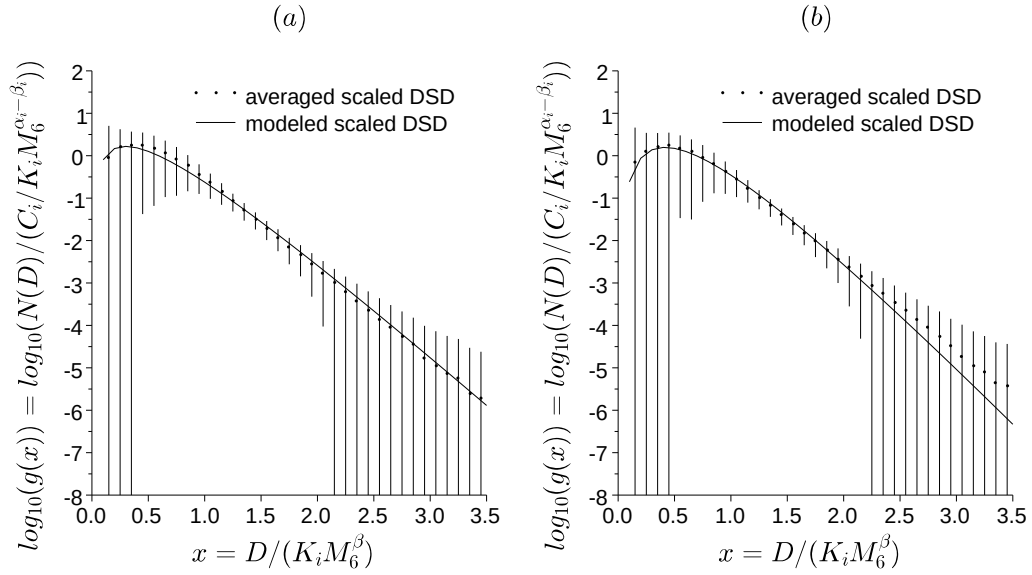

Figure 3.12: Averaged scaled distribution (points) with the DSD model scaled by M_6. - The models adjusted by the regression relationships and by "all-moment" are showed in (a) and (b), respectively. The bars represent the standard deviation of the scaled distributions.

estimator, and the (3.29) and (3.31) are obtained based on "all moments" estimator. All these expressions are under the form of power-law relationships, the exponent is related to the parameter α and β, and the general distribution has a direct impact on the prefactor of the power-law relationship.

$$M_k = \frac{36.216\Gamma(3.266+k)}{0.0657^{-k}}\left(\frac{R}{7.125\times10^{-3}}\right)^{0.271+0.199k}, \tag{3.28}$$

$$M_k = \frac{57.717\Gamma(2.595+k)}{0.0805^{-k}}\left(\frac{R}{7.125\times10^{-3}}\right)^{0.304+0.190k}, \tag{3.29}$$

$$M_k = \frac{321.45\Gamma(2.699+k)}{0.0726^{-k}}(Z)^{-0.0028+0.167k}, \tag{3.30}$$

$$M_k = \frac{75.349\Gamma(3.828+k)}{0.0616^{-k}}(Z)^{0.0417+0.160k}. \tag{3.31}$$

These relationships which link any DSD moment (M_k) to the predictor moment are totally based on the estimated DSD parameters. The model evaluations carried out in the next section are devoted to select the better DSD models, so as the better moment relationships, which provide the possibility to derive the climatological Z-R and KE-R relationships.

3.2.3 Evaluation of one-moment formulations

The same criteria (bias and correlation coefficient) defined in (2.30) and (2.31) are used to evaluate the scaling DSD model (3.22). Fig.3.13 shows the performance of the DSD formulation scaled by the $M_{3.67}$ as a function of raindrop diameter.

As the middle order moment ($M_{3.67}$) is applied in the DSD formulation, the middle-size raindrops are rather well reconstituted. The correlation coefficient between the modeled and measured drops numbers reaches 0.9 for drops with 2 $mm < D <$4 mm. But the correlation degrades rapidly for the small and large drops. A significant bias (20%) is evidenced by the evaluation. And the bias becomes even larger for the drops with $D <$0.3 mm and $D >$4 mm. Regarding the different estimators, the DSD estimated by "all moments" reduces slightly the bias for the large raindrops. And the correlation coefficients of the two estimators are nearly identical.

Fig.3.14 shows the performance of the DSD formulation scaled by M_6 as a function of the drop diameter. Compared to the formulation scaled by $M_{3.67}$, this model yields a good performance for the large drops at the cost of a low correlation coefficient for

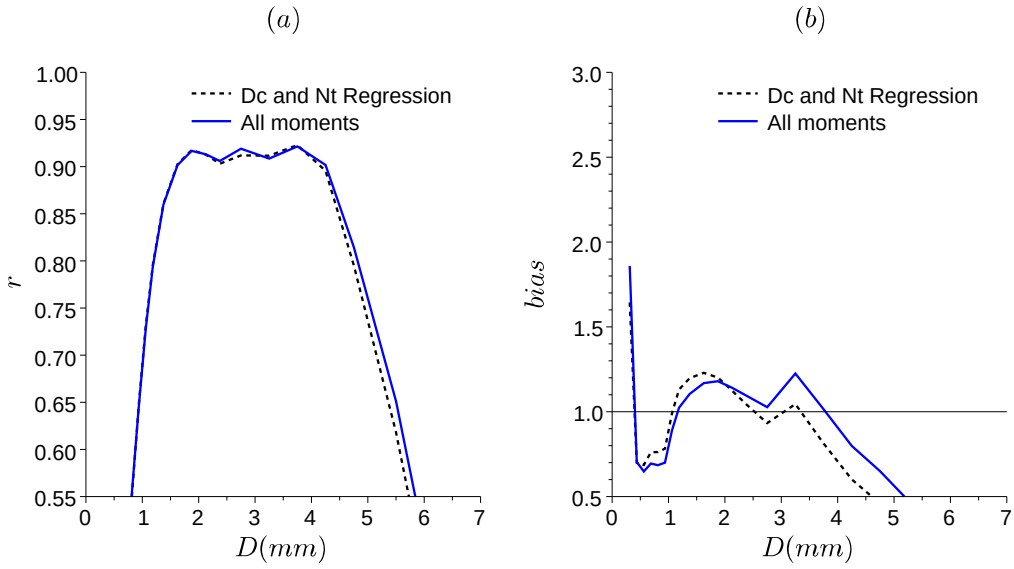

Figure 3.13: Evaluation of DSD model scaled by $M_{3.67}$. - The correlation coefficient and bias between the modeled and observed $N(D)$ are showed in (a) and (b). The black and blue curves represent the DSD models parametrized by "regression" and "all-moment" methods, respectively.

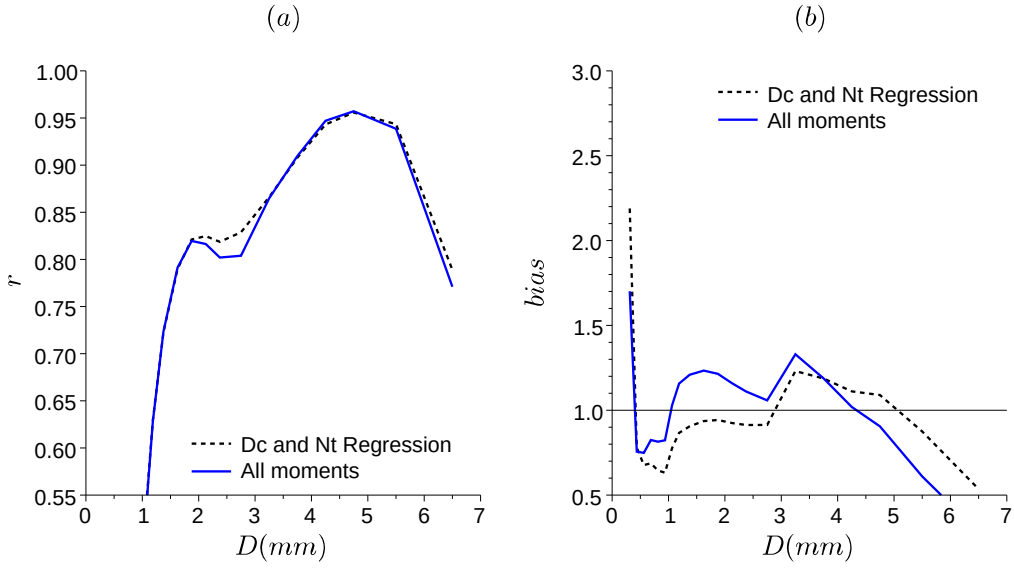

Figure 3.14: Evaluation of DSD model scaled by M_6. - The correlation coefficient and bias between the modeled and observed $N(D)$ are showed in (a) and (b), The black and blue curves represent the DSD models parametrized by "regression" and "all-moment" methods, respectively.

the small drops. This behavior is explained by the weak relationships between the number of small drops and the high order moment (M_6). A significant bias (+- 20%) is produced by this model as well. However, in this case, the model parameterized by the "simple regression" approach seems to be less biased than the one estimated by the "all moments" approach.

The reconstituted moments based on the $M_{3.67}$- and M_6- scaling DSD formulations are evaluated in Fig.3.15 and Fig.3.16, respectively. As mentioned before, the predictor moment which is used to scale the DSD formulation is well reconstituted. For the moment relationships with the predictor moment $M_{3.67}$, both the "simple regression" and "all-moment" estimators produce the same correlation coefficients. Note that the "all-moment" estimation reduces significantly the bias for the high order moments, at the cost of an underestimation at the low order moments. The high order moments are potentially important for the following studies, such as investigations of KE-R and Z-R relations. Thus the estimator based on "all moments" is selected for the DSD formulation scaled by the rain rate.

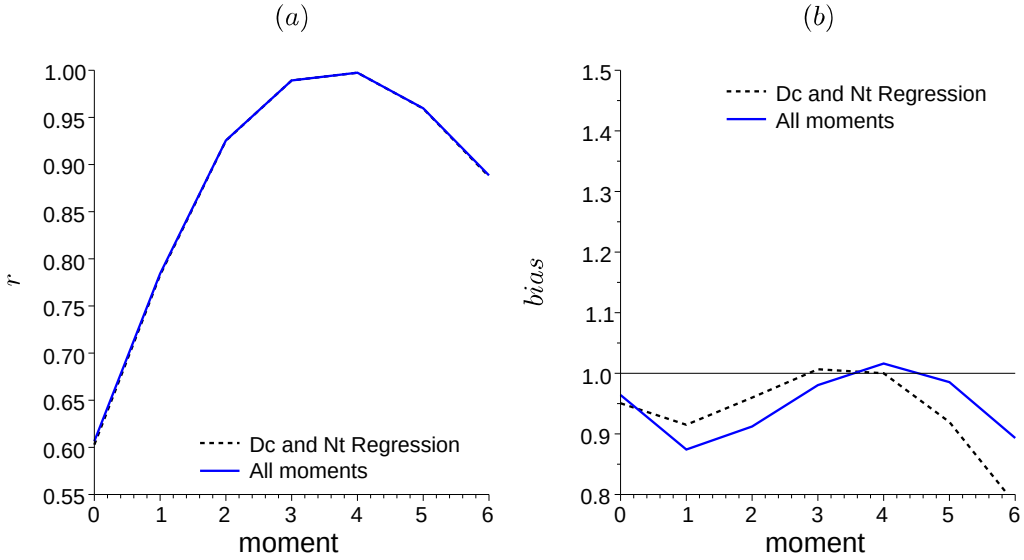

Figure 3.15: Evaluation of reconstituted moments based on the DSD model scaled by $M_{3.67}$. - The correlation coefficient and bias between the reconstituted and observed M_i are showed in (a) and (b). The black and blue curves represent the DSD models parametrized by "regression" and "all-moment" methods, respectively.

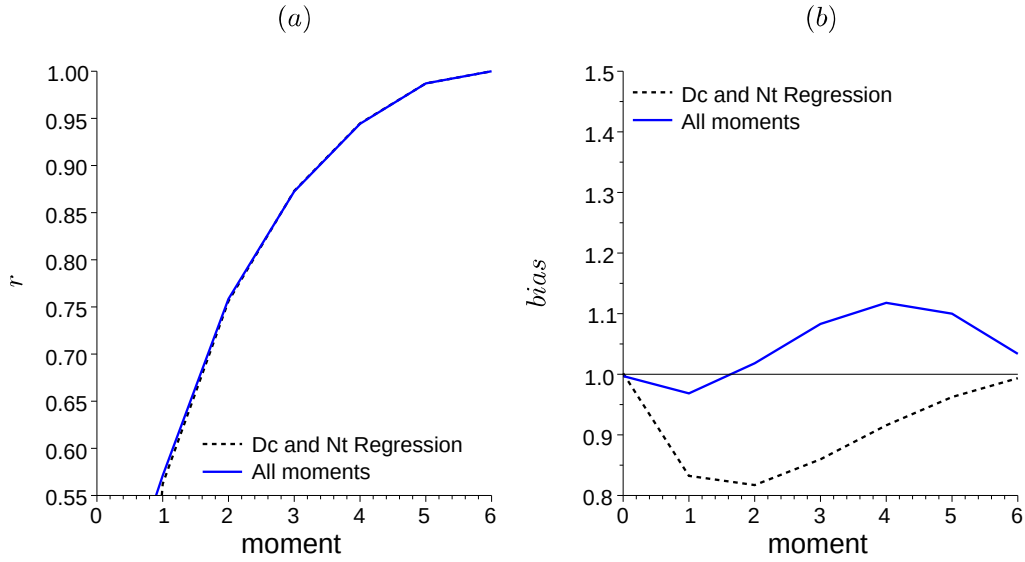

Figure 3.16: Evaluation of reconstituted moments based on the DSD model scaled by M_6. - The correlation coefficient and bias between the reconstituted and observed M_i are showed in (a) and (b). The black and blue curves represent the DSD models parametrized by "regression" and "all-moment" methods, respectively.

Regarding the moment estimation made by Z (Fig.3.16), the "simple regression" and "all moments" estimators exhibit totally different behaviors. The moments estimated by Z based on "all moments" are higher than the observations (up to 12%), while a significant underestimation (up to 18%) of middle and large order moments is produced by the DSD model based on "simple regression". For the same reason (potential importance of the high order moment), the "simple regression" estimator is selected in the following investigations concerning the DSD formulation scaled by Z.

To conclude, a comprehensive evaluation of DSD models scaled by $M_{3.67}$ or M_6 has been presented in this subsection. Different from the case of two-moment DSD model, the choice of the estimators ("regression" or "all moments") has a direct impact on the estimation of parameters contained in the one-moment formulation. Regarding the model performance, it seems that the coefficient correlation is less influenced by the estimators, compared to the model bias. And it is hard to conclude which parameter-estimator produce less bias to another. All depends on the moments or the raindrop diameters that we focus on. In this study, the estimator "all-moment" and "regression" are selected for the DSD formulations scaled by R and Z, respectively, for the purpose

of the better estimation of high order moments.

3.3 DSD scaled by different moment(s)

3.3.1 Comparison of the climatological $g(x)$ scaled by different moment(s)

As mentioned before, the two- and one-moment scaling DSD formulations come from the same DSD formulation scaled by N_t and D_c. With respect to previous work e.g. Lee et al. (2004), the two parameters (K and C) are accounted for in the formulation to remove the impact of the scaling moment(s) on the scaled distributions. Hence, it will be interesting to compare the distributions obtained in the different scaling frameworks, and notably the $g(x)$ functions. Because the DSD model scaled by N_t and D_c is devoted to parameterize the individual spectrum, while the $g(x)$ in the one- and two-moment DSD model is related to the climatological scaled distribution for whole 5-min DSD spectra, the mode of the shape parameter (μ=2.5) in the histogram 2.21 is considered as an average value for the DSD model scaled by N_t and D_c. Shape parameters describing

Scaling Moment(s)	**Estimators**	μ
N_t and D_c	Mode of μ estimated by M_0, M_3 and M_4	2.5
M_6 and $M_{3.67}$	Regression (3.2)	2.439
M_6	Regression (3.20) and (3.21)	1.699
$M_{3.67}$	All Moments (3.26)	1.596

Table 3.3: Shape parameter (μ) obtained in different scaling frameworks.

the scaled distributions are listed in Table.3.3. The value of μ varies from 1.5 to 2.5 among different scaling frameworks. It seems that the distributions scaled by one moment are characterized by a smaller μ, compared to those scaled by two moments. One should note that the parameters for one-moment DSD formulation are issued from the evaluation focused on reconstitutions of high order moments, otherwise, one may obtain a totally different estimate of shape parameters (μ=2.266 and 2.823 for the DSD model scaled by $M_{3.67}$ and M_6, respectively, see previous subsection and Table.3.2 for details). Nevertheless, the values listed in Table.3.3 are considered as the "best" estimate for the climatological DSD parameters in current study.

3. PRACTICAL DSD FORMULATIONS BASED ON SCALING TECHNIQUE

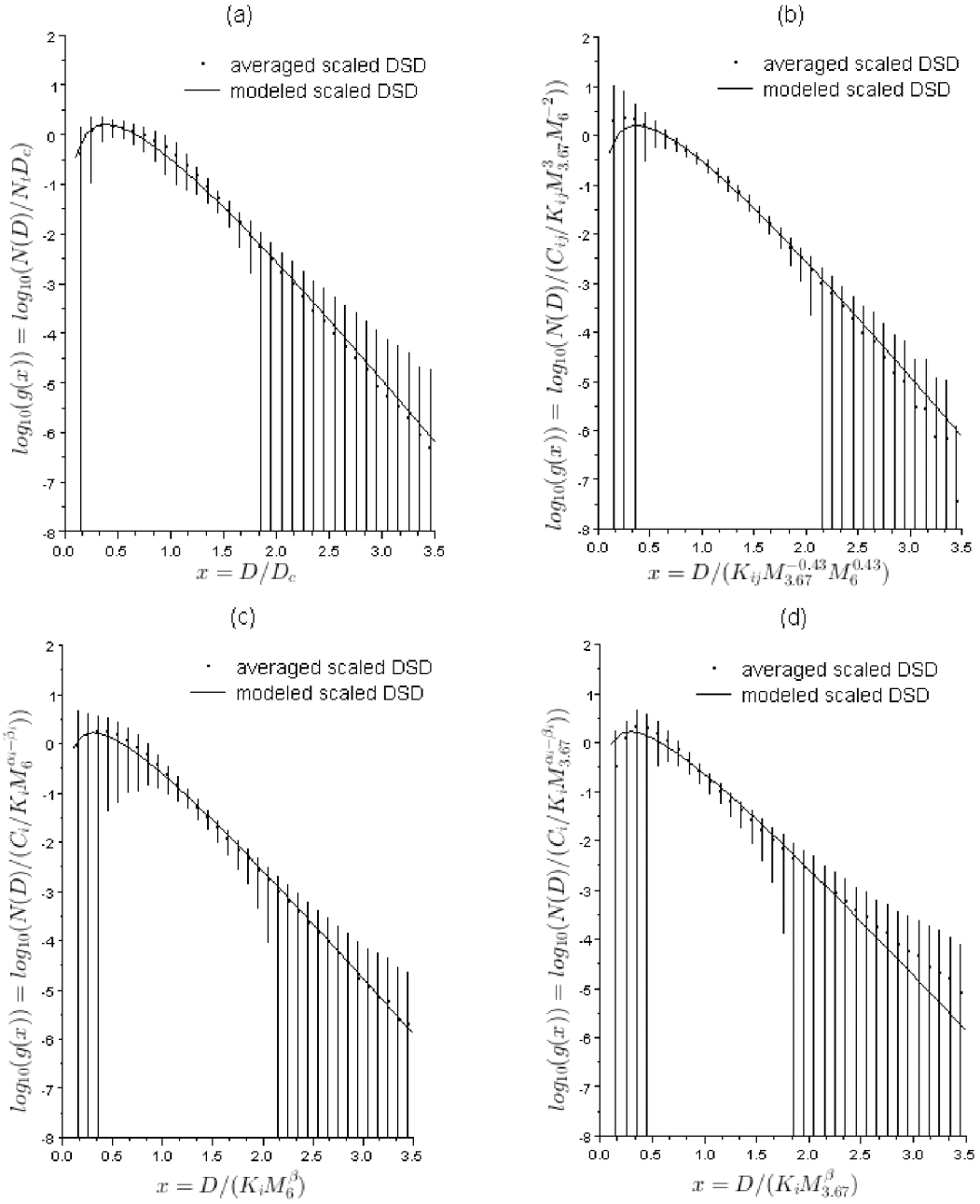

Figure 3.17: Averaged scaled $g(x)$ distributions (points) with the appropriate modeled gamma functions in different scaling framework. - The averaged distributions and gamma models scaled by N_t-D_c, M_6-$M_{3.67}$, M_6 and $M_{3.67}$ are showed in (a), (b), (c) and (d), respectively. The bars represent the standard deviation of the scaled distributions.

Four averaged and modeled $g(x)$ distributions scaled by N_t-D_c, M_6-$M_{3.67}$, M_6 and $M_{3.67}$, respectively, are displayed in Fig.3.17. The distributions showed in Fig.3.17b, c and d are identical to those showed in Fig.3.4a, Fig.3.11b and Fig.3.12a. The modeled scaled distribution displayed in Fig.3.17a is based on the mode of the shape parameters distribution (μ=2.5). Each figure displays the standard deviation of the scaled distributions by the black bars as. It is hoped that the variation of the $g(x)$ function could be reduced as much as possible by the scaling procedure.

As a general comment regarding the standard deviation of the scaled spectra, one may consider the vertical bars at the different diameters for the different moment scaling formulations. As expected, accounting for N_t in the DSD formulation reduces significantly the variability of scaled distribution for x <0.5. The $M_{3.67}$-scaled process reduces the variability of the scaled distribution for the medium scaled diameter range (0.5< x <1.8). And the M_6-scaled process allows a significant reduction of the standard deviation for the upper x values ($x \approx 2.0$) at the cost of an increased variability for the small scaled diameters (x <0.5). The scaling technique using $M_{3.67}$ and M_6 together yields the reduction of the variation both for the small and large scaled diameter (0.5< x <2.5). It is worth mentioning that the four averaged scaled distributions are similar to each other, which is in good agreement with the concept of the DSD formulation as the product of a concentration multiplied by a unique probability density function of the raindrop diameter scaled by a characteristic diameter.

3.3.2 Climatological Z-R relationships

The moment relationships (3.29) and (3.30) are able to link various rainfall variables to measurable DSD moments. Investigation of Z-R relationship is an application with particular interests in hydrometeorological research. Setting k=6 in the $M_{3.67}$-scaling moment relationships (3.29), or k=3.67 in the M_6-scaling moment relationships (3.31) produces two climatological Z-R relationships

$$Z = 338.8R^{1.44}, \tag{3.32}$$

and

$$Z = 249.9R^{1.64}. \tag{3.33}$$

Equation (3.32) comes from the DSD formulation scaled by rain rate, which means that the reflectivity factor is expressed as a function of the rain rate, while equation

(3.33) is derived from the DSD formulation scaled by radar reflectivity factor, which implies that the rain rate is reconstituted by the reflectivity factor (this is the general case in radar hydrology). This result is analogous to standard regression analyses e.g. Chapon et al. (2008) that could be performed on the (Z, R) pairs derived from each single spectra, by considering successively Z and R as the explanatory variable.

Fig.3.15 and Fig.3.16 display preliminary evaluations of these two Z-R relationships by comparing reconstituted and observed Z and $M_{3.67}$ values. Both of them have good coefficient correlations (>0.9), with 10% underestimation of Z for (3.32) and 10% underestimation of R for (3.33). In order to further evaluate these two climatological Z-R relationships, four criteria (coefficient correlation, bias, Nash coefficient and root mean square deviation) calculated between the estimated and observed rainfall are calculated for the $Z = aR^b$ relationships with prefactor (a) ranging from 50 to 350 and exponent (b) ranging from 1.0 to 3.0, based on the whole 5-min DSD data. The contours in Fig.3.18 show the statistical criteria as a function of prefactor and exponent. The cross (+) and (x) pictograms represent the Z-R relationship (3.32) and (3.33), respectively.

Fig.3.18 confirms the good performance of two Z-R relationships regardless their different prefactor and exponent. The Z-R relationship (3.33) produces 10% underestimation of rainfall, which is slightly improved in the (3.32). Except for this underestimation, the other statistical criteria indicate that the relationship (3.33) is slightly better than (3.32) for the rainfall estimation. In any case, this example illustrates the impact of the scaling procedure on the prefactor and exponent of the Z-R relationship.

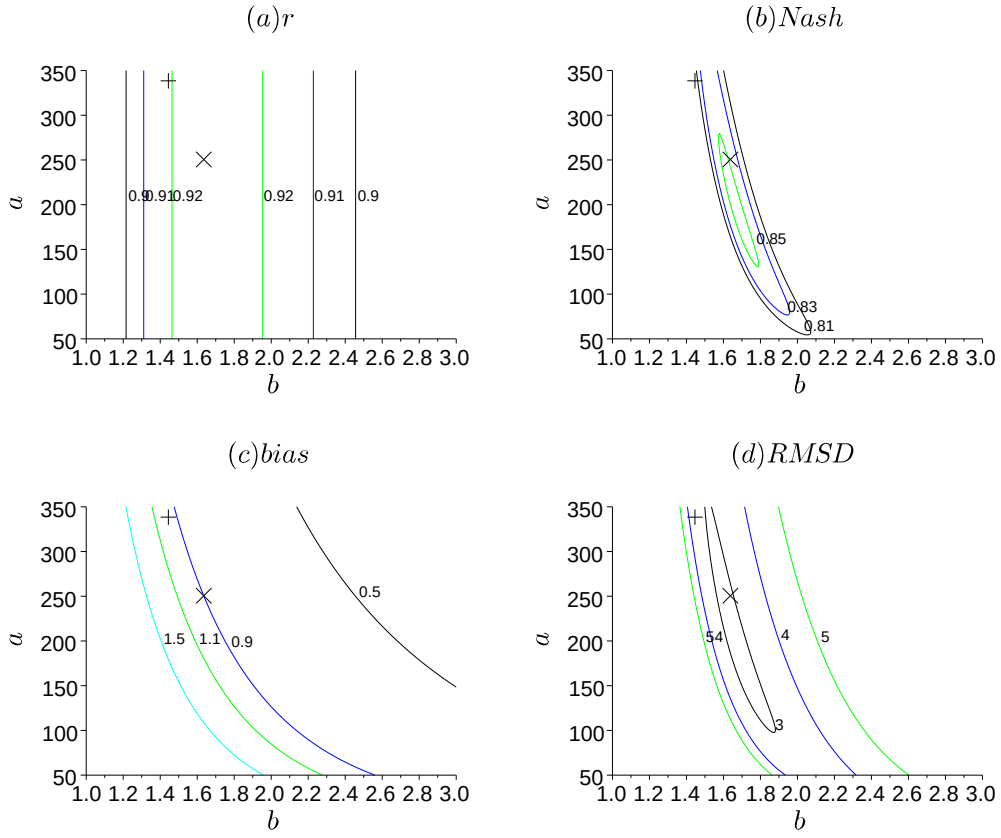

Figure 3.18: Statistical criteria calculated between estimated and observed rainrates as a function of the exponent and prefactor in the Z-R relationship, for the climatological 5-min DSD data. - The coefficient correlation, bias, Nash coefficient and root mean square deviation are showed in a, b, c and d. The cross (+) and (x) pictograms represent the Z-R relationship (3.32) and (3.33), respectively.

Chapter 4

Application of scaling DSD formulation

In the previous chapter, a general framework has been developed to extend the DSD formulation scaled by N_t and D_c to general DSD formulations scaled by any one or two moment(s). This chapter will be devoted to illustrate three typical applications of scaling DSD formulations: 1) understanding the intra-event variability of rainfall based on the variation in the DSD; 2) reconstitution of DSDs by available observed DSD moments and 3) estimation of the rainfall kinetic energy for soil erosion studies. Instead of using the reflectivity factor and rain rate derived from the disdrometer, the operational weather radar and rain gauge measurement are used in this chapter. The objective is to show the performance of the scaling DSD formulation in the practical rain event analysis.

4.1 Investigation of the intra-event variability through the scaling DSD formulation

4.1.1 Rain event description

In order to investigate the intra-event DSD variability, one rain event, mixing high and low intensity rain rate occurred during the night of October 22, 2008 is studied in this section. This intense rain event was characterized by the arrival of a cold front on the Mediterranean south moisture flow. During the daytime of 21 October, southeastern France was covered by a stable moisture flow from the Mediterranean Sea which generated some local convective systems in the Cévennes-Vivarais region. A frontal disturbance moved from the northeast to the southwest and converged to the convective systems in the Cévennes-Vivarais region at midnight on 22 October (See Fig.4.1). The largest rainfall occurred over the foothills of the Cévennes on the evening of 21 October. Daily maximum rainfall reached 470 mm at La Grand Combe (about 10 kilometers to the north of Alès) (Vincendon et al., 2011). The raingauge installed at Alès measured 86.6 mm rainfall during 17 hours (22:00 21 October-17:00 22 October). This heavy rainfall led to a significant rise of the water level of the Gardons, Cèze and Ardèche rivers.

Fig.4.2 shows the intensity of rain measured by the disdrometer and rain gauge for each 5-minute interval. The maximum intensity of precipitation (about 50 mm h^{-1}) occurred between 2:30 and 4:30 of the 22 October, when the frontal disturbance arrived in the Cévennes-Vivarais region. Strong radar echoes (>=50 dBZ) were also obtained during this period. It is worth mentioning that the rain intensities measured by raingauge and disdrometer, the reflectivity factor observed by weather radar and disdrometer are in good agreement.

Fig.4.3 illustrates the evolution of the meteorological observations (temperature, wind speed, wind direction and humidity) during this event. The temperature decreased by 7 °C after the cold front passage. A sudden cooling occurred in the morning (08:00-11:00) of 22 October associated with the passage of the cold front. The measurement of the wind revealed more details about the cold frontal disturbance. A stable southeast wind blew until the arriving of the cold front at around 2:00. During the passage of the cold front (2:00 to 6:00), the wind speed decreased between 4:00 and 5:00. And then, a moderate north wind (5 ms^{-1}) was observed after the passage of the cold front.

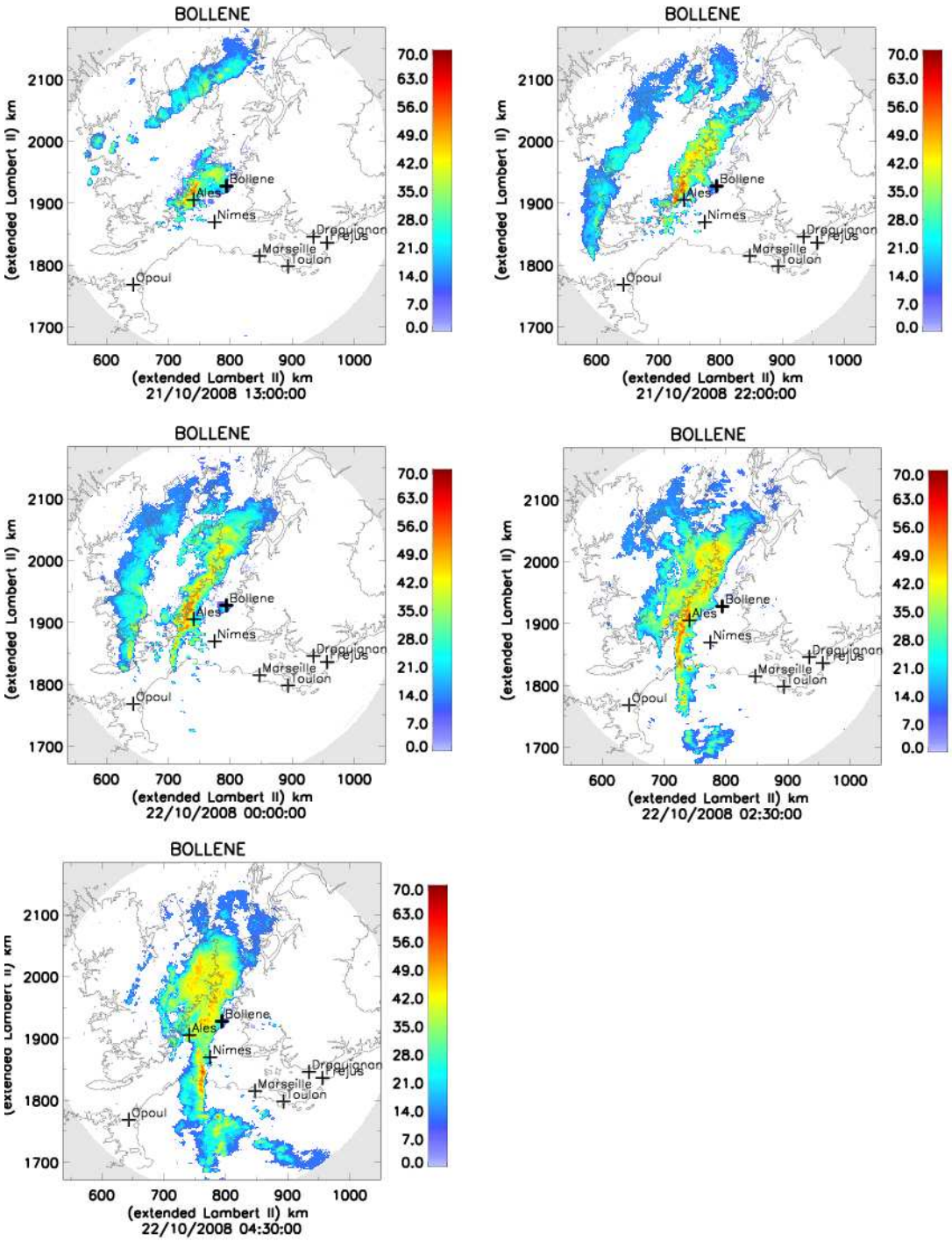

Figure 4.1: Reflectivity images observed by the Bollène radar at 0.8 degree elevation, for the rain event of the 21-22 October 2008. - Radar observation reveals a passage of the cold font.

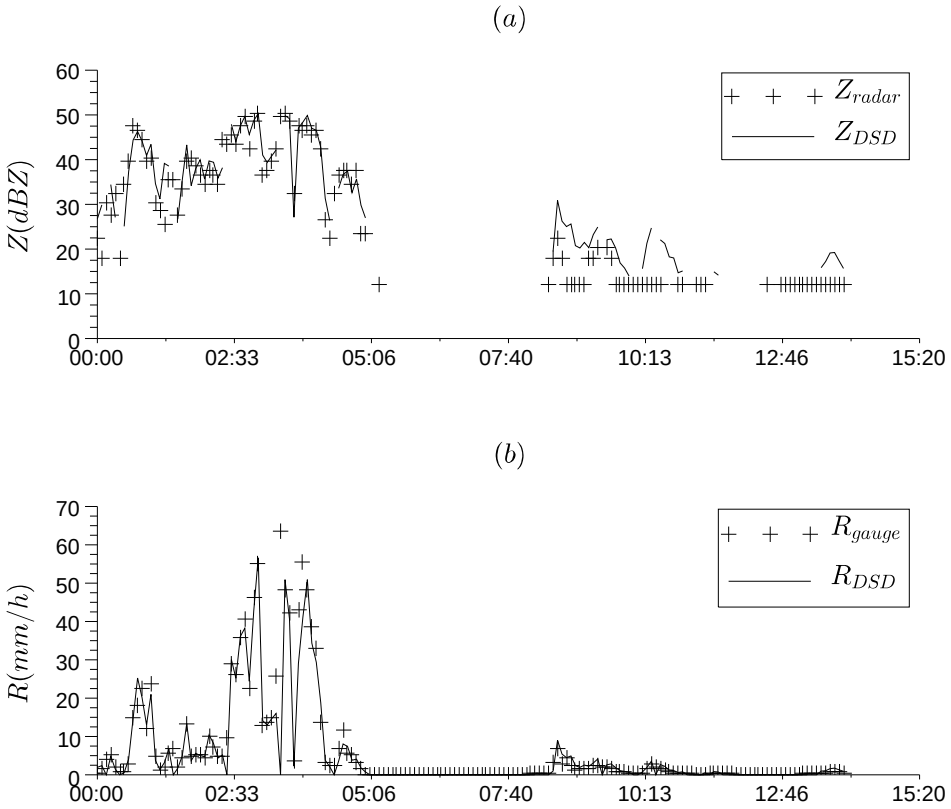

Figure 4.2: Comparison of Radar reflectivity factor derived from disdrometer at Alès and observed by the Nîmes radar in (a); rain intensity observed by the disdrometer and raingauge in (b) for the event of the 22/10/2008. - Good agreements are found among different instruments.

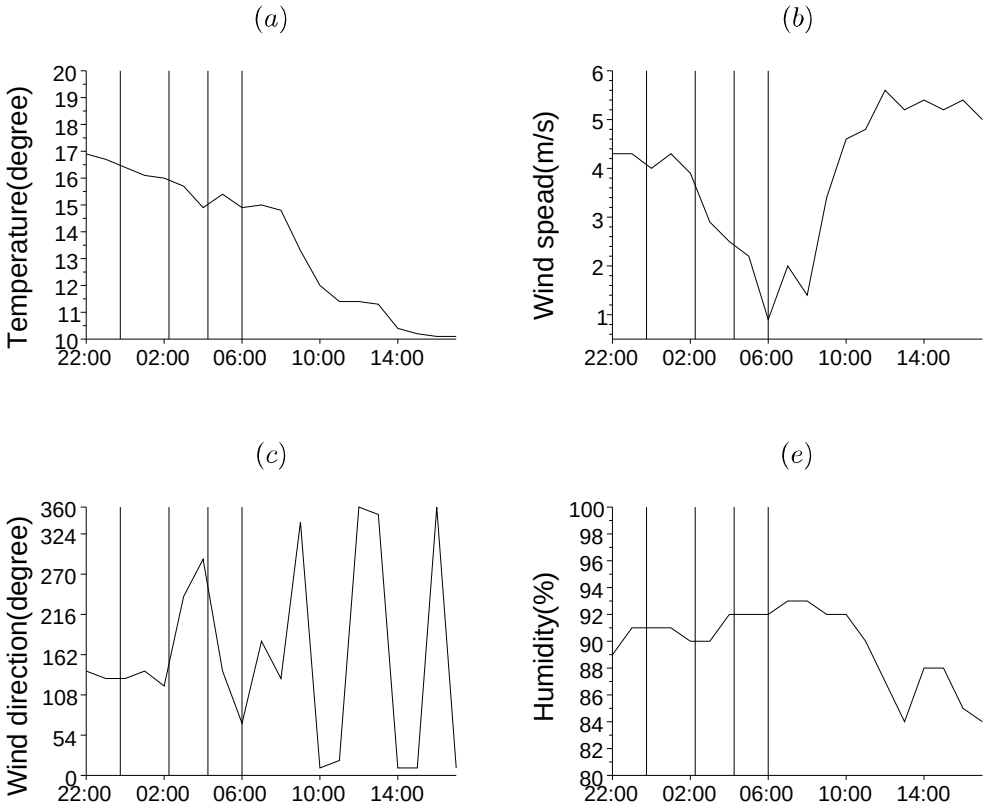

Figure 4.3: Meteorological observations for the rain event of the 22/10/2008. - The figure shows the time series of temperature, wind speed, wind direction and humility measured by a meteorological station near Alès.

The upper air observations by the radiosonde at Nîmes (about 40 km away from Alès) are presented in Fig.4.4. The red, continued blue and dashed blue curves represent the temperature, the wet bulb potential temperature and the dew point curves, respectively. The latter two terms are used to infer the amount of moisture in the air. The freezing level was found at 3100 m before the front passage and 2800 m after the front passage. A narrow thermal inversion layer was situated between 3500 m and 4000 m with a rapid decrease of humidity. This layer is likely to be associated with the production of the precipitating hydrometeors.

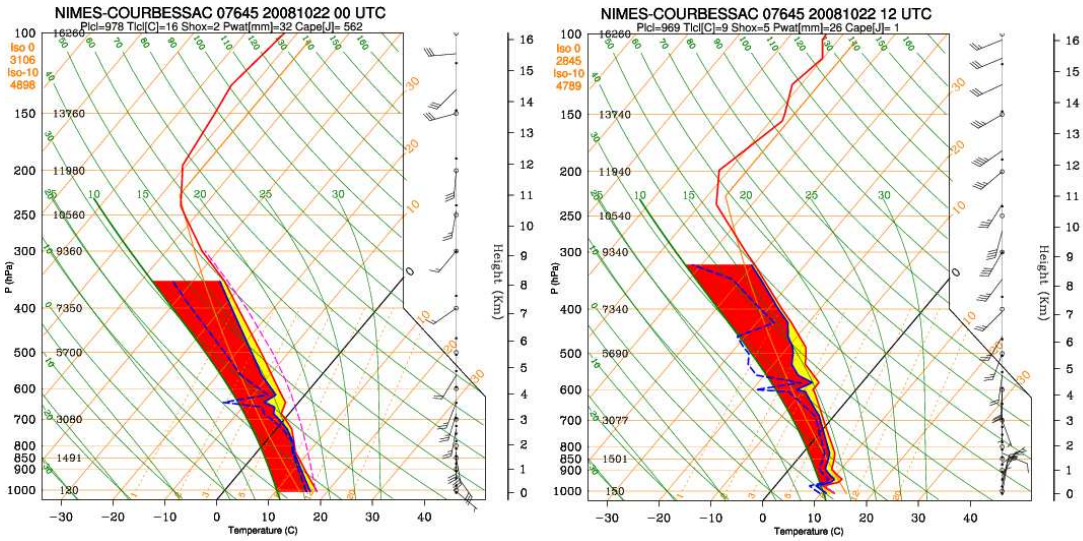

Figure 4.4: Radiosounding observed at Nîmes, at 00:00 and 12:00 of the 22 October 2008. - (www.meteocenter.com)

Some numerical model studies for this event have been carried out by several authors. Vié et al. (2011) performed a rainfall forecasting based on the operational AROME model. The rainy location forecasting by the numerical model approximately matched the observed precipitation area but the convective part was underestimated in terms of both spatial extent and maximum rain intensity. Duffourg and Ducrocq (2011) highlighted the role of the moisture flow from the Mediterranean Sea during the initiation and mature phase of the rain event. This moisture flow was raised to the top of the troposphere (10 km) in the core of the convective parts.

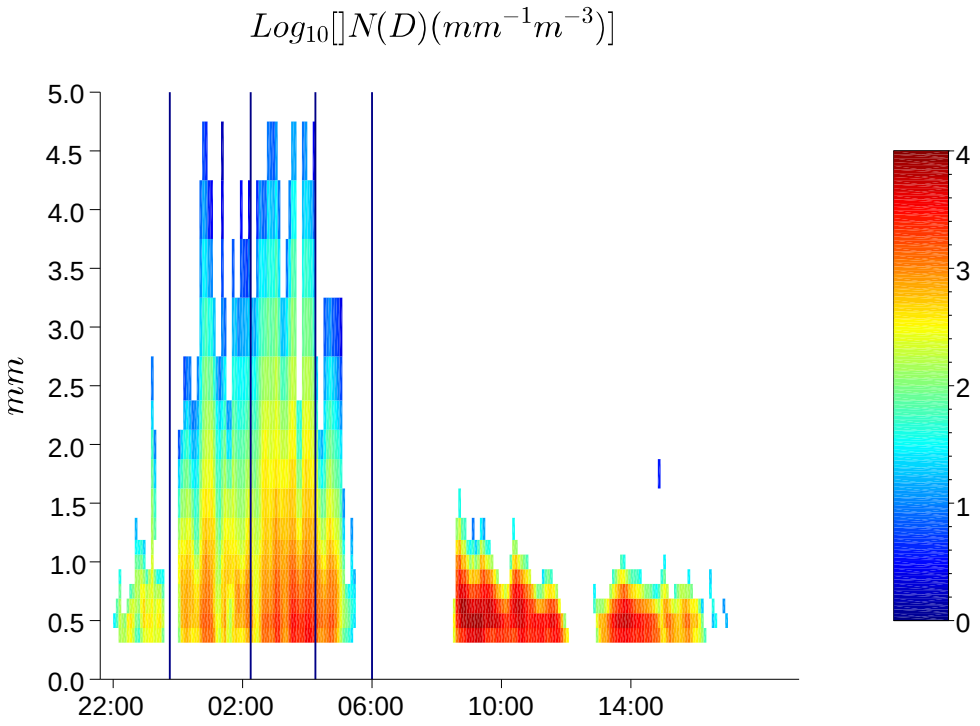

Figure 4.5: Disdrometer observations for the rain event of the 22/10/2008. - The y-axis represents the size of the raindrop, and the color refers to the number of raindrops.

4.1.2 Variation of the DSD and rain phases within the event

Fig.4.5 shows the time-evolution of the DSD for this rain event with a 5-min resolution. The y-axis represents the size of the raindrop, and the color refers to the number of raindrops. Different DSD characteristics can be distinguished before, during and after the passage of the cold front. The 5-min DSD spectra have been parameterized based on the scaling DSD formulation presented in Section 2.2. The three time-series of N_t, D_c and μ are shown in Fig.4.6.

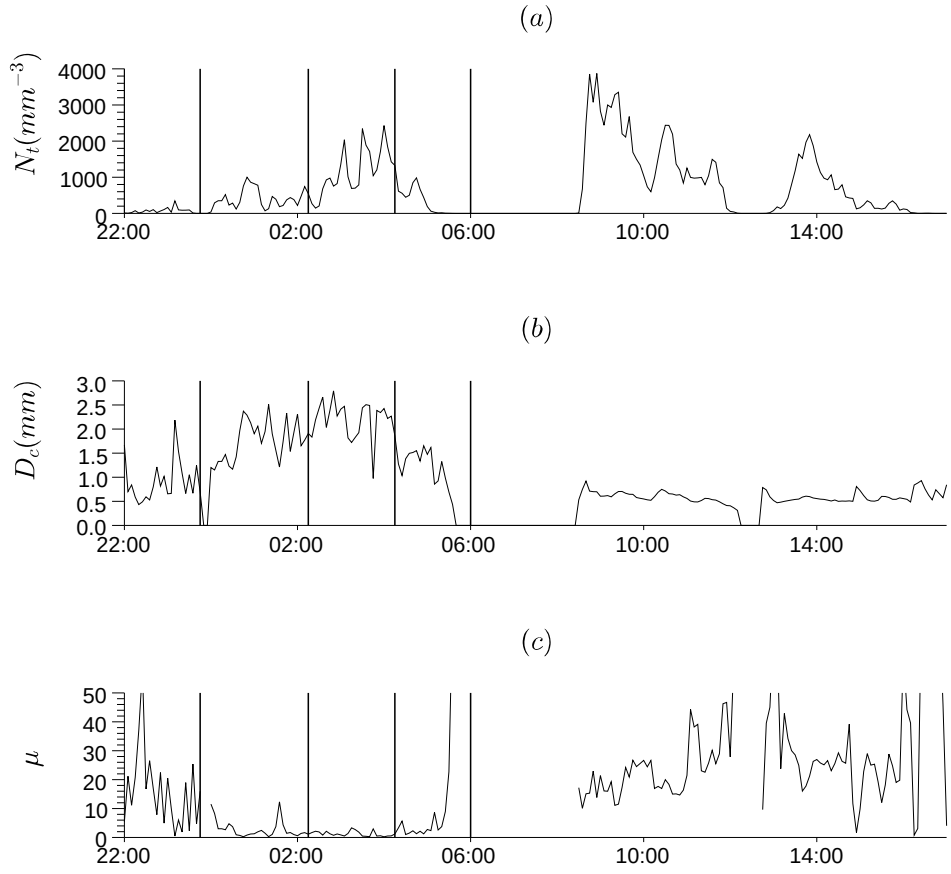

Figure 4.6: Time series of the DSD parameters for the rain event of the 22/10/2008. - (a) concentration; (b) characteristic diameter and (c) the scaling DSD shape parameter μ.

Five intra-event rain phases are subjectively distinguished considering the radar images (Fig.4.1), the meteorological observations (Fig.4.3) and the DSD time-series

(Fig.4.6) together. The event started with a light rain between 22:00 and 23:55 (phase 1). The cold front was still far away. A strong convective system had already developed close to Alès. Its maximum reflectivity reached 60 dBZ. The disdrometer was located at the edge of the convective system. A few small raindrops (diameter around 1 mm) were observed at that time (Fig.4.5). From 00:00 to 02:25 (phase 2), the cold front was approaching. At the same time, the convective system began to move to the east. More and more raindrops are detected by the disdrometer. A significant increase of D_c and decrease of μ was observed during this phase. However, the concentration of the drops (N_t) remained limited to 1000 m^{-3}. After 02:30 (phase 3), the cold front merged with the convective system, and eventually enhanced the convection. At this moment, the center of the convective system arrived at Alès and produced the majority of the rainfall. The most remarkable variation in the DSD observations was the increase of the raindrop concentration to 2000 m^{-3}, while the D_c and μ remained relatively steady with respect to the previous phase. The rainfall began to decrease at 4:30 (phase 4) and finally stopped at 6:00 in the morning. This dissipating phase was characterized by the rapid decrease of N_t and D_c together.

The fifth (last) rain phase occurred in the daytime of the 22 and lasted for several hours. The light rainfall consisted of many small raindrops. The concentration of drops reached up to 3500 m^{-3}. The characteristics of this phase correspond to the typical drizzle precipitation, which is usually seen at either the front or tail end of convective systems.

Fig.4.7 illustrates the DSD spectra scaled by N_t and D_c in each rain phase. As predicted by the evolution of the shape parameter (μ), two contrasting shapes are found between the strong convective phases (such as the phases 2 and 3) and weak convective phases (such as the phases 1 and 5). The strong convective phase is characterized by a broad scaled distribution with a μ near zero, while the non-convective phase is characterized by a narrow distribution with a high value of μ.

The DSD is scaled by $M_{3.67}$-M_6, M_6 and $M_{3.67}$ in Fig.4.8, 4.9 and 4.10, respectively. It can be seen that, for each rain phase, the shapes of distributions scaled by different moment(s) are approximately similar to each other. Regardless the moment(s) used in the scaling procedure, the strong convective phase is always characterized by a broad distribution while a narrow distribution is exhibited for the weak convective phases.

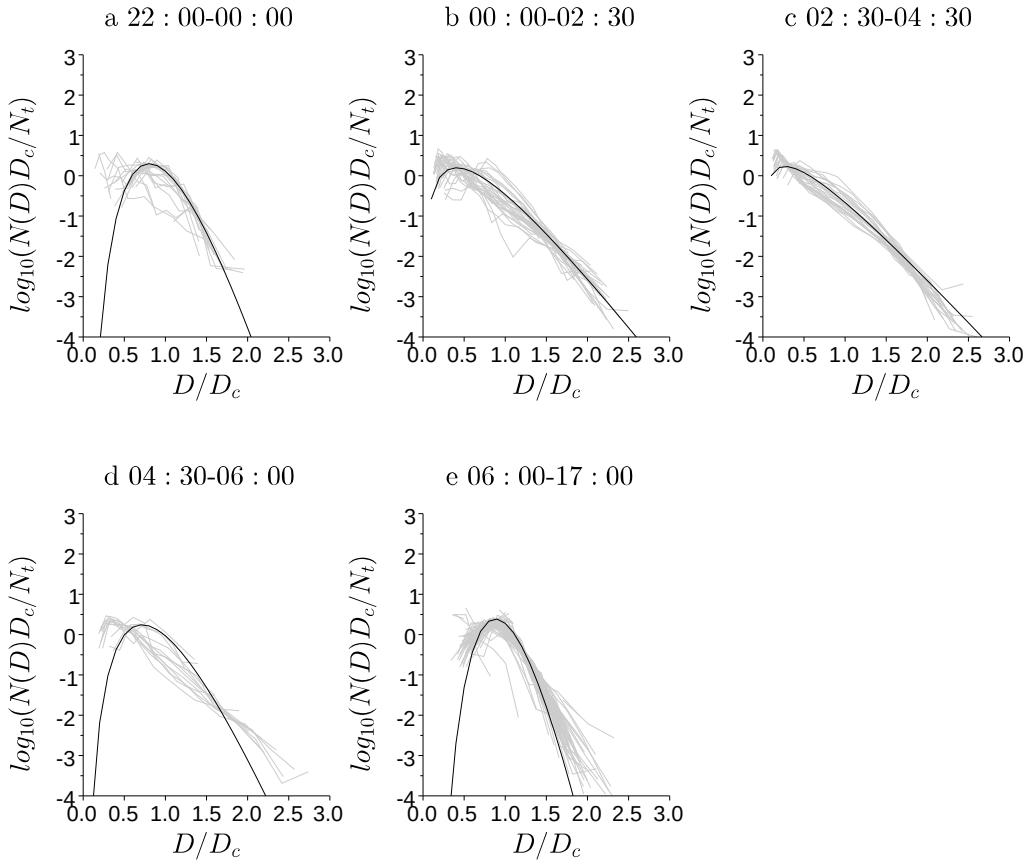

Figure 4.7: DSDs scaled by the concentration and characteristic diameter for each rain phase. - The black curve represents the mean scaled spectrum of each rain phase, based on the average μ value.

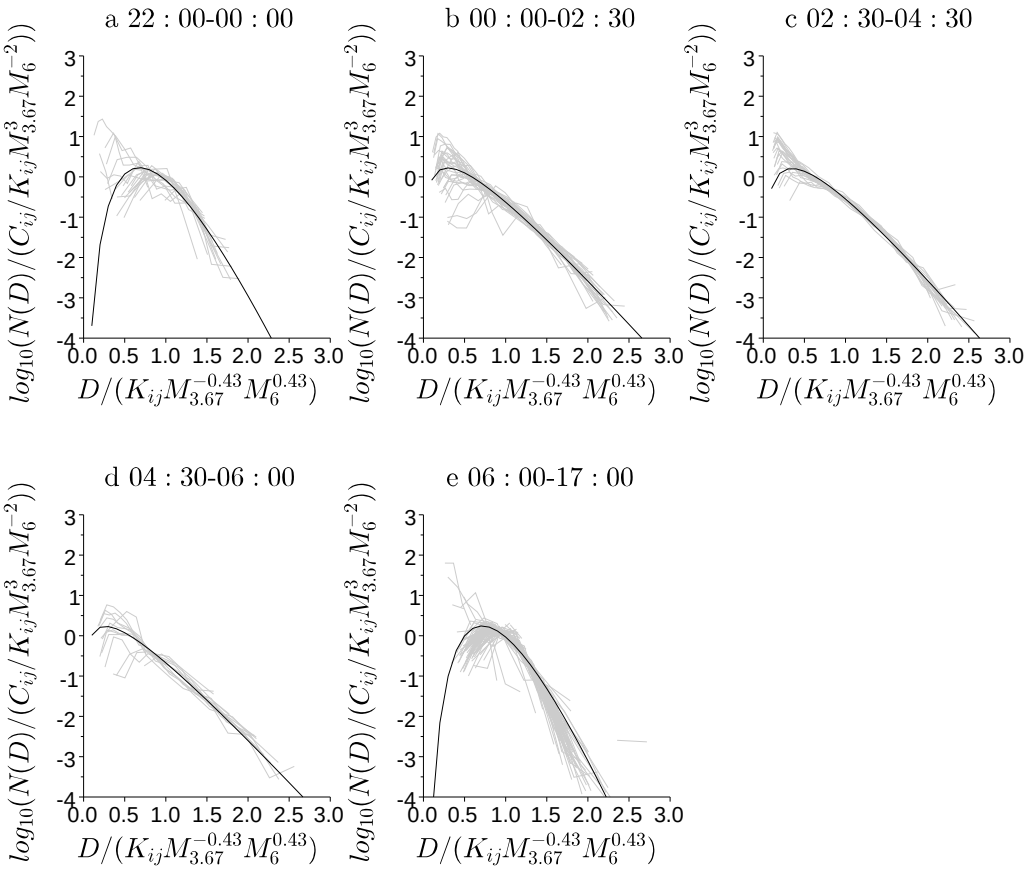

Figure 4.8: Distributions scaled by the $M_{3.67}$ and M_6 for each rain phase. - The black curve represents the modeled scaling distribution.

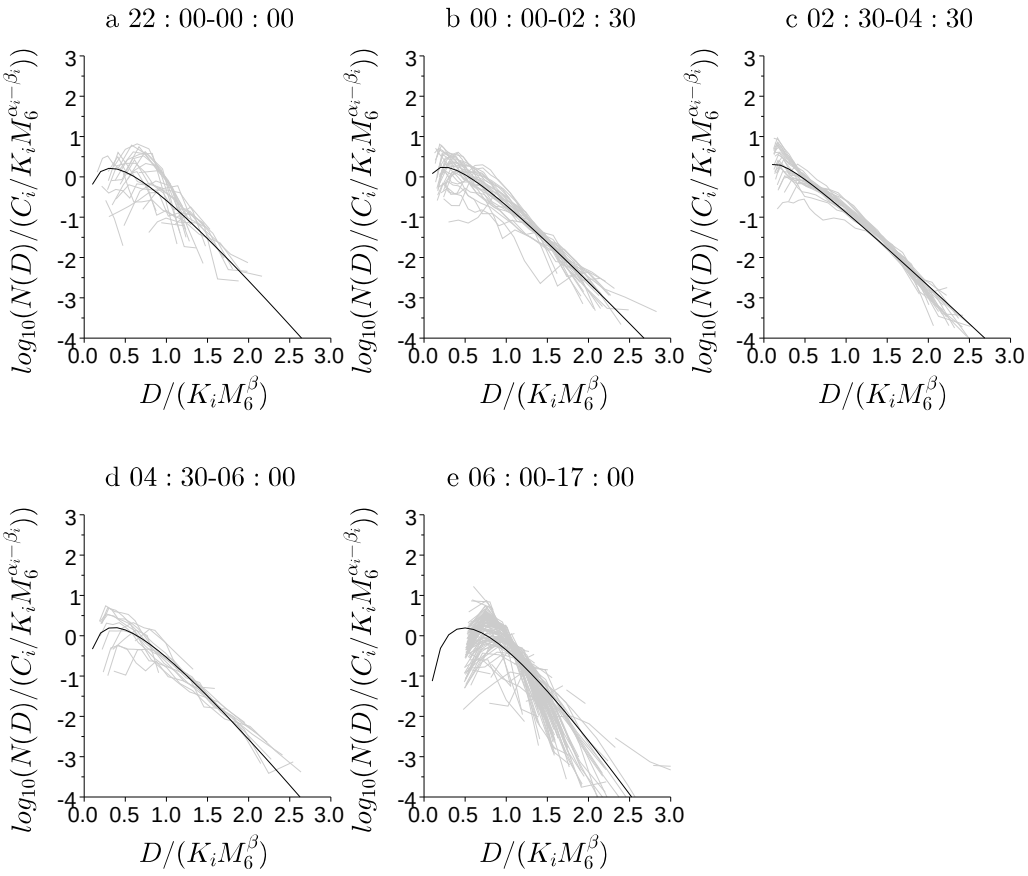

Figure 4.9: Distributions scaled by the M_6 for each rain phase. - The black curve represents the modeled scaling distribution.

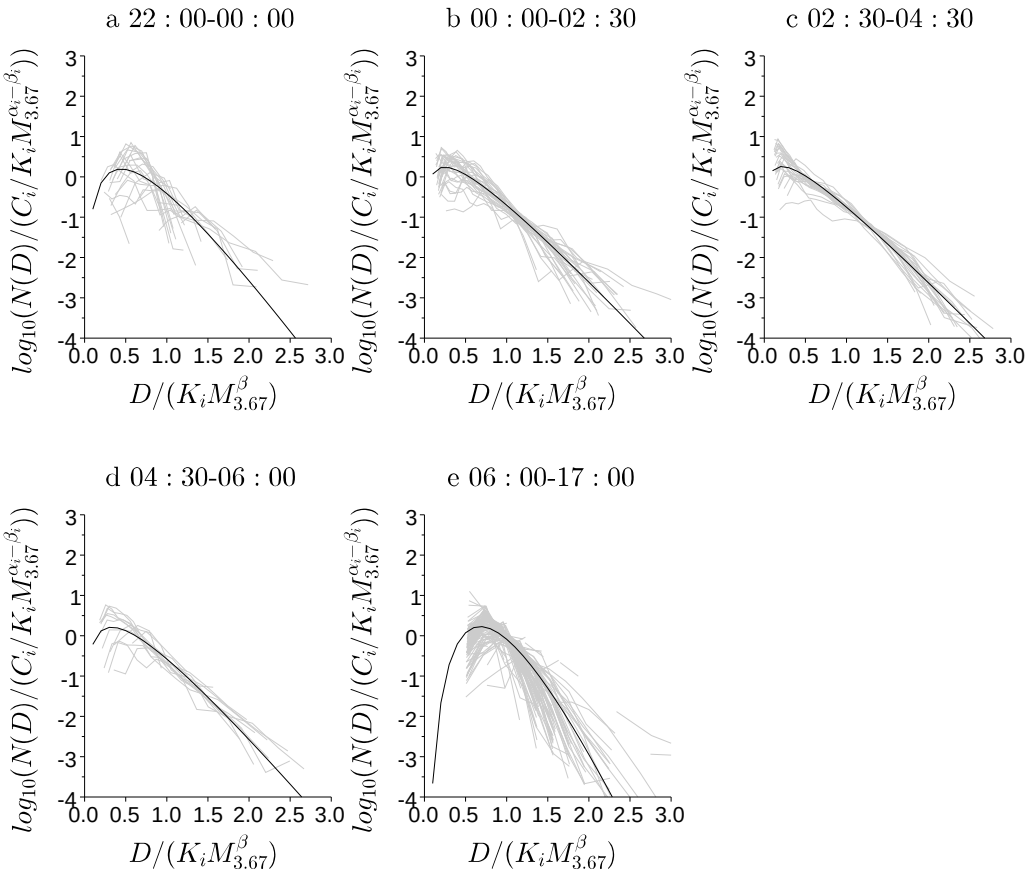

Figure 4.10: Distributions scaled by the $M_{3.67}$ for each rain phase. - The black curve represents the modeled scaling distribution.

4.1.3 Investigation of the rain phases based on remote sensing observations

Assuming that the front system is stationary, the disdrometer captured the principle DSD characteristics belonging to different parts of the convective system. The raindrops in the edge of system (phase 2) are dominated by some large raindrops with a low concentration. This implies that the collision-coalescence of the raindrops plays an important role in this phase. The core of convective system (phase 3) is characterized by the increase of concentration, and more particularly, the increase of the number of small drops. This phenomenon is probably explained by the weak evaporation, under the condition of the updraft which supplies enough moisture in the column of air. A typical drizzle occurred after the passage of the cold front. This precipitation type indicates usually the presence of a relatively stable air preventing continued vertical development of convection in atmosphere.

Fig.4.11 shows the evolution of the vertical reflectivity profile and the air vertical velocity profile above Alès derived from the Doppler radars. It can be seen that the phase-separation based on the surface DSD characteristics corresponds well with the distinct property of the vertical profiles observed in the atmosphere. In the leading and ending edge of the convective system (phases 1 and 4), the reflectivity factor extends vertically to 10 km, with the maximum reflectivity factor around 35 dBZ. The low vertical velocity implies weak convection in these phases. The main precipitation fell down in the phases 2 and 3. In phase 2, the reflectivity factor increases suddenly compared to that in phase 1. The 30 dBZ reflectivity factor can be found at 5 km in altitude, with a vertical velocity between 1 and 2 m/s. The phase 3 corresponds to the strongest convection in this rain event. The convective system extending to a high altitude (30 dBZ is found at 7 km) produces an intense rainfall at Alès. The air vertical velocity reaches up to 3 m/s at the same time. And in the last drizzle phase, the low radar reflectivity factor ($<$25 dBZ) extending to about 4 km in altitude, with a stable and low vertical air velocity is found in Fig.4.11. The combination of Fig.4.11, 4.6 and 4.5 reveals the correspondence among the characteristic of the DSD, the vertical extension of the convective system, the maximum radar reflectivity factor and the vertical velocity of air.

Fig.4.13 shows the evolution of the vertical cross section passed through Alès (Fig.4.12) during the second and third rain phases. A very strong convective system located 10

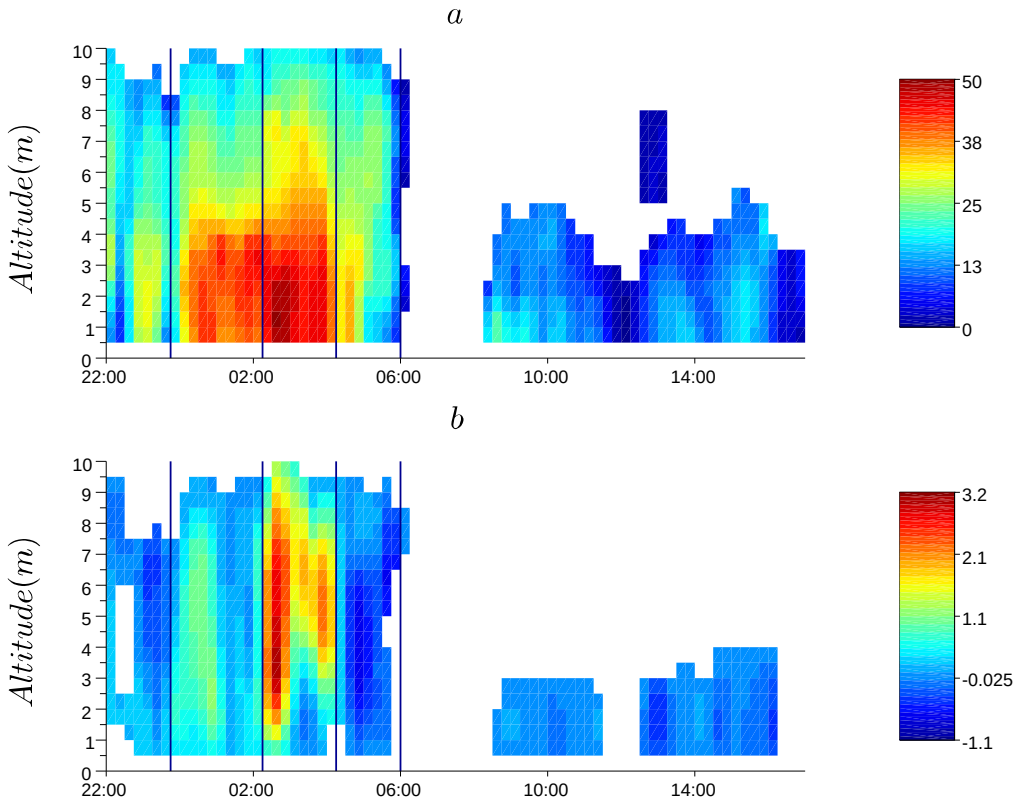

Figure 4.11: Vertical reflectivity (dBZ) profile (top) and air vertical velocity (m/s) profile (bottom) above Alès derived from the Doppler radars. - The velocity profile is provided by Olivier Bousquet (Météo-France).

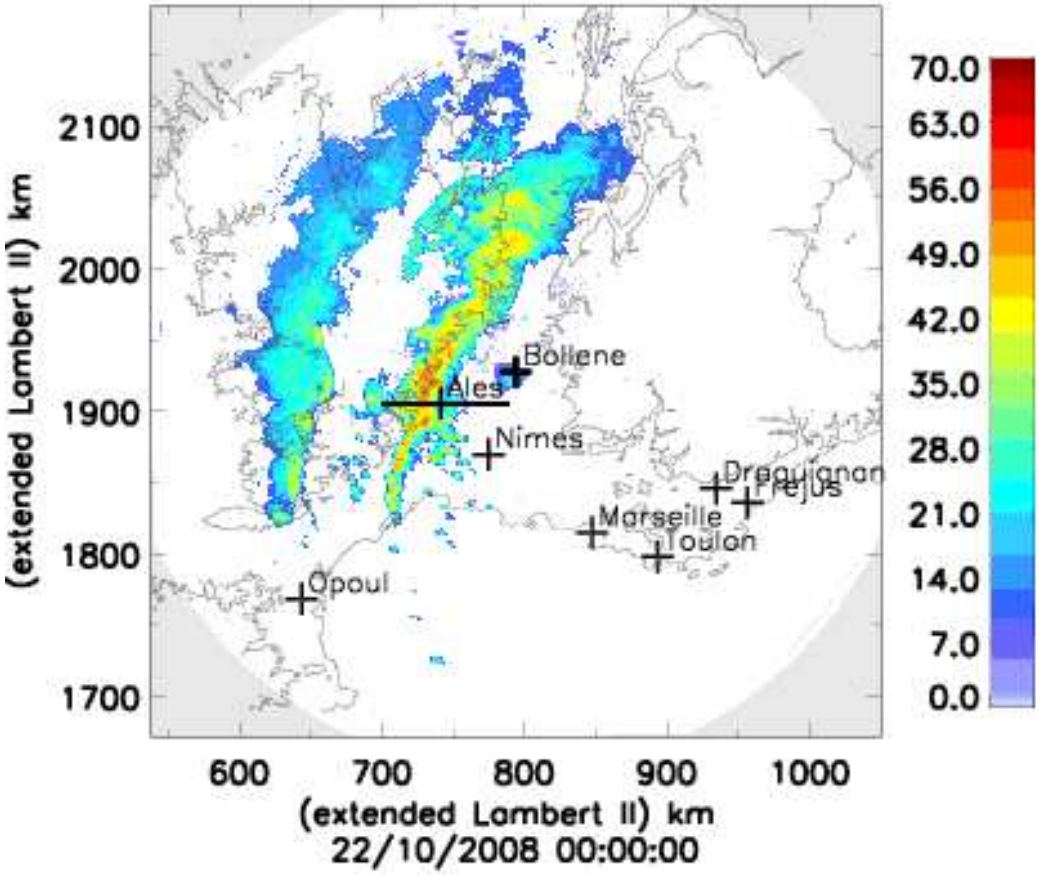

Figure 4.12: Illustration of the position of the East-West vertical cross section.
- The cross section extends to 120 *km* from the East to the West.

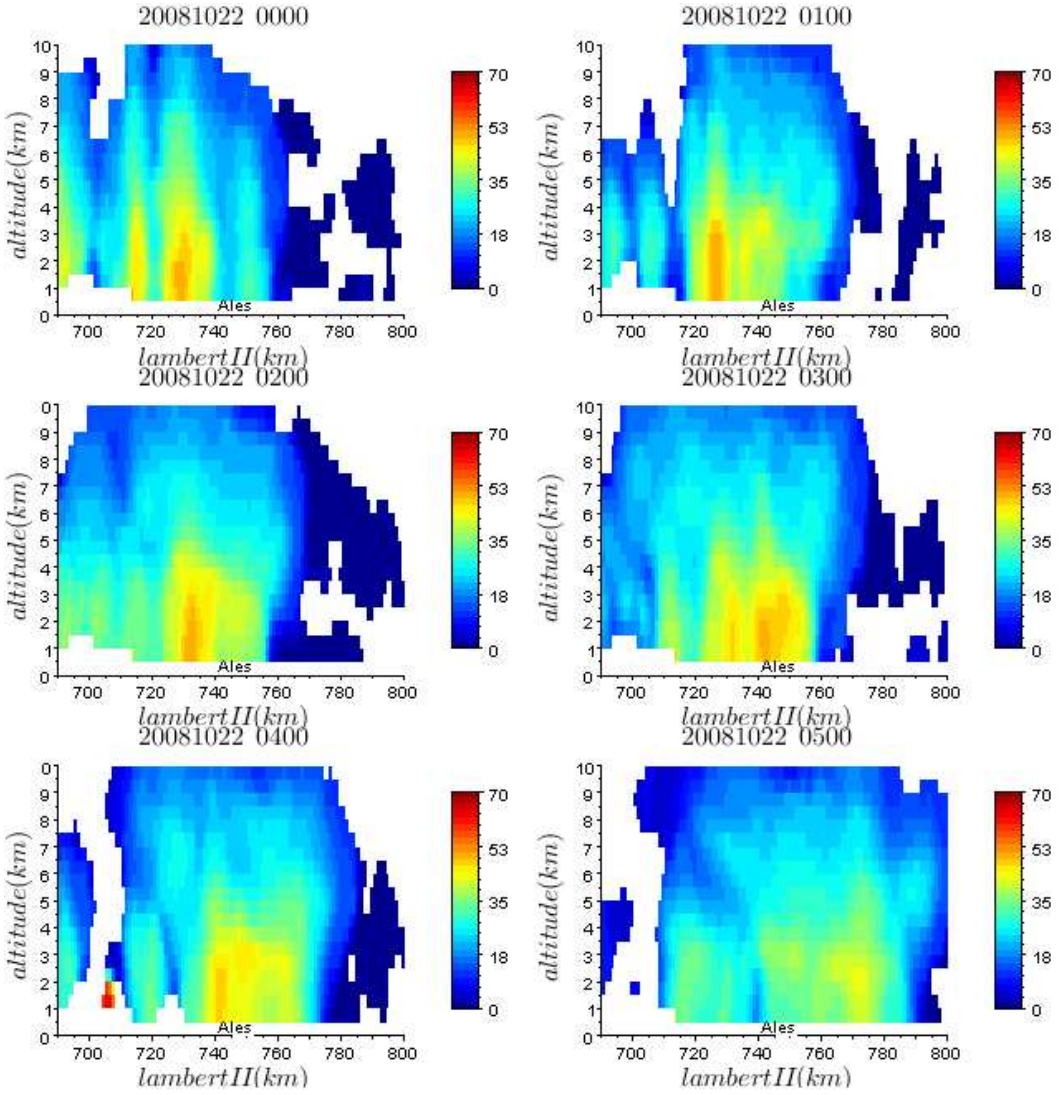

Figure 4.13: Evolution of the vertical cross section of radar reflectivity factor, shown in Fig.4.12, during the convective rain phases 2 and 3. - The figure shows the evolution at 1-hour interval.

km to the west of Alès has developed before midnight (within the phase 1). In fact, as mentioned by Vincendon et al. (2011), the maximum rainfall intensity of this event was found over these mountainous areas. During the second phase, Alès was always at the leading edge of the convective system until the arriving of the cold front driving the convective system to the east. Our disdrometer observed the core of the convective system in the phase 3, and the zone of convection dissipated gradually during its moving. The vertical cross section of reflectivity factor confirms that the increase of the concentration at the end of phase 2 is associated with the arriving of the convective system.

The products of polarimetric radar are under evaluation by Météo-France. The high noise contained in the polarimetric observations is still a challenge for the rainfall estimations. Fig.4.14 shows the differential reflectivity (Zdr) and the correlation coefficient (ρhv) observed by the polarimetric radar at Nîmes. Some high Zdr values, found in the phases 2 and 3, suggest the presence of large raindrops. Phase 5 is characterized by some negative Zdr values at about 2 km altitude. The low reflectivity factors with negative Zdr values suggests the presence of drizzle in this layer. The significant decrease of the correlation coefficient at around 3 km altitude, which is just near the freezing lever, is probably explained by the mixing of the solid and liquid drops. However, due to the noise of the current polarimetric products, the polarimetric observation will not be discussed in detail here. The following study will be focused on the reflectivity factor.

As we have shown in Fig.4.11, the maximum reflectivity factor and the convective system extension in the vertical extension are two important variables apparently linked with the DSD measured at the surface. Fig.4.15 displays the time series of (1) the altitude where the reflectivity factor attains 30 dBZ and (2) the maximum vertical reflectivity factor values. In comparison with the evolution of D_c shown in Fig.4.6, the maximum vertical reflectivity values are well correlated with the characteristic diameters. A high maximum Z-value in the atmospheric column implies a large characteristic diameter measured at the surface. Fig.4.16 shows a plot of maximum vertical reflectivity factor versus the characteristic diameter. The 30 dBZ was found to be an appropriate limitation to separate the DSD spectra into two groups with $D_c > 1$ mm and $D_c < 1$ mm, respectively. For the first group, the maximum vertical reflec-

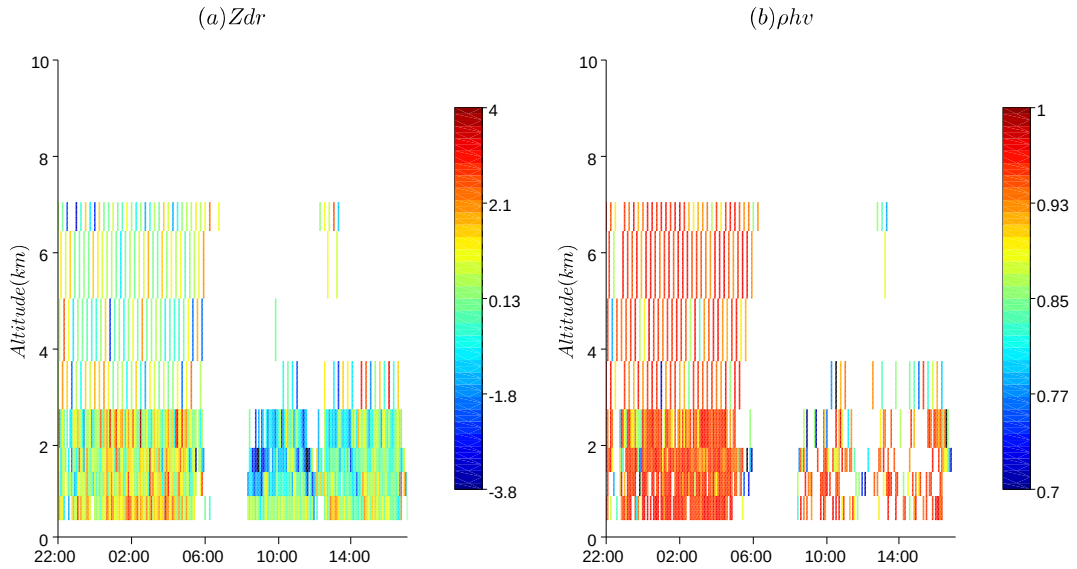

Figure 4.14: Differential reflectivity and correlation coefficient above Alès observed by the polarimetric radar at Nîmes. - High noise is contained in these results.

tivity factors increases simultaneously with D_c, while in the second group, such simple relationship between Z and D_c is not evident.

Regarding the concentration, its signature on the reflectivity factor is complex. The increase of the concentration at the end of the phase 2 is probably linked with the vertical extension of the 30 dBZ-isograms. However, no signal is identified for the fifth drizzle phase with very high drop concentration. In fact, as already stated, the reflectivity factor is not an appropriate variable to represent the tiny raindrop concentration. Fig.4.16b plots the relationship between the altitudes of the 30 dBZ-isograms and the raindrop concentration. A lot of high concentration DSD records with a low radar reflectivity factor (<30 dBZ) can be found in the figure.

To summarize, the detailed analysis of the rain event of 22/10/2008 based on multiple observations showed that: 1) the whole rain event can be segregated into 5 rain phases through the evolutions of the scaling DSD parameters (N_t, D_c and μ); 2) the same shifting-phase signals can be found both in DSD variations and in reflectivity factor profile above Alès. It seems that the maximum value of the reflectivity factor profile is related to the characteristic diameter measured on surface, especially when the

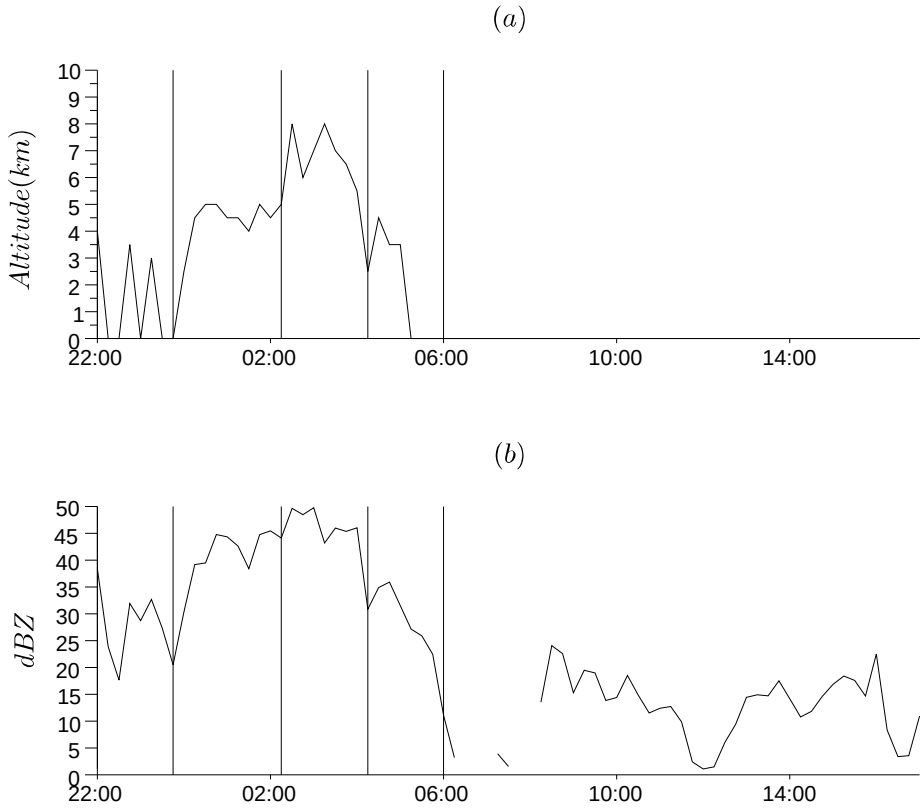

Figure 4.15: Time series of (a) the altitudes where the reflectivity factor attains 30 dBZ; (b) the maximum vertical reflectivity factor values. - The 30 dBZ reflects the vertical extension of the precipitated system, and the maximum Z is an indicator of the convective activity.

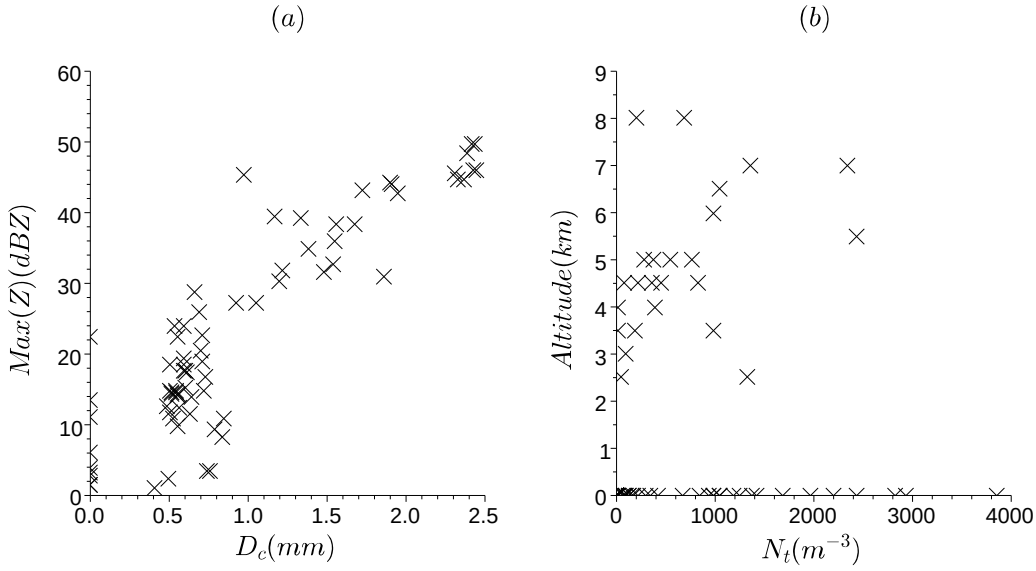

Figure 4.16: Relationships between (a) the maximum vertical reflectivity factor values and the characteristic diameter; (b) the altitudes of the 30 dBZ isograms and the raindrop concentration. - The maximum vertical reflectivity factor value seems to relate to the characteristic diameter.

maximum factor exceeds 30 dBZ. However, the deduction of the DSD concentration from the radar observations is still a challenge to overcome in the future.

4.2 Reconstitution of the DSD by the observed moments

4.2.1 Reconstitution of the DSD

In Section 3.1.2, the climatological DSD formulations scaled by rain rate (R) and radar reflectivity factor (Z) together are obtained. Substituting the estimated parameters values listed in Table.3.1 to the two-moment scaling DSD expression (3.3), the climatological DSD formulation scaled by $M_{3.67}$ and Z can be derived as

$$N(D) = 1511 M_{3.67}^{3} M_6^{-2} \left(\frac{D}{0.831 M_{3.67}^{-0.429} M_6^{0.429}}\right)^{2.439} exp\left(-\frac{7.748 D}{M_{3.67}^{-0.429} M_6^{0.429}}\right). \quad (4.1)$$

In the same manner, substituting the appropriate climatological parameters listed in Table.3.2 to the one-moment scaling DSD expression (3.22), one obtains two DSD

formulations, scaled by the $M_{3.67}$ and Z, respectively, as

$$N(D) = 10600 M_{3.67}^{-1.6} (\frac{D}{0.450 M_{3.67}^{0.19}})^{1.595} exp(-\frac{12.43D}{M_{3.67}^{0.19}}), \tag{4.2}$$

$$N(D) = 85109 M_{6}^{-0.17} (\frac{D}{0.414 M_{6}^{0.167}})^{1.699} exp(-\frac{13.77D}{M_{6}^{0.167}}). \tag{4.3}$$

These expressions suppose that the variation in the DSD is totally controlled by the rain rate and/or radar reflectivity factor. The evaluations have been performed to compare the reconstituted DSDs with observations based on the whole 5-min DSD dataset in the Section 3.1.3 and 3.2.3. A good agreement between the disdrometer observations and reconstituted DSD can be found in the Fig.3.5, Fig.3.13 and Fig.3.14. However, these evaluations were made in the context of a pure DSD studies in which both the Z and R are derived from the DSD as well. Hence, one may question the performance of these DSD models based on the real weather radar and raingauge observations. The next section will be devoted to address this question and illustrate the DSD reconstitutions for the 2008/10/22 rain event.

4.2.2 Application of the DSD reconstitution on a rain event

We recall the good agreements on the reflectivity factor measured by radar and disdrometer, and the rain rate measured by raingauge and disdrometer, shown in Fig.4.2. Four 5-min DSD spectra are preliminary selected to illustrate the DSD reconstitutions by the climatological DSD formulations (4.1) to (4.3). Fig.4.17, Fig.4.18 and Fig.4.19 illustrate the reconstituted DSDs by R-Z, by R and by Z, respectively. The R and/or Z derived from disdrometer, or observed by radar and/or raingauge, are separately applied in the scaling procedure.

In comparison to the disdrometer observations, the second (top-right) and the fourth (bellow-right) DSDs are well reconstituted by the rain intensity and radar reflectivity factor, regardless the multiple-peak distribution exhibited in the fourth DSD. For these two DSDs, there are good agreements among the different instruments (radar, raingauge and disdrometer). A different case is showed in the first DSD (top-left). Using the Z and R derived from the disdrometer leads a good reconstitution of the DSD, while the introduction of the reflectivity factor observed by radar produces a large error due to the discrepancy between the reflectivity observed by radar and derived from disdrometer.

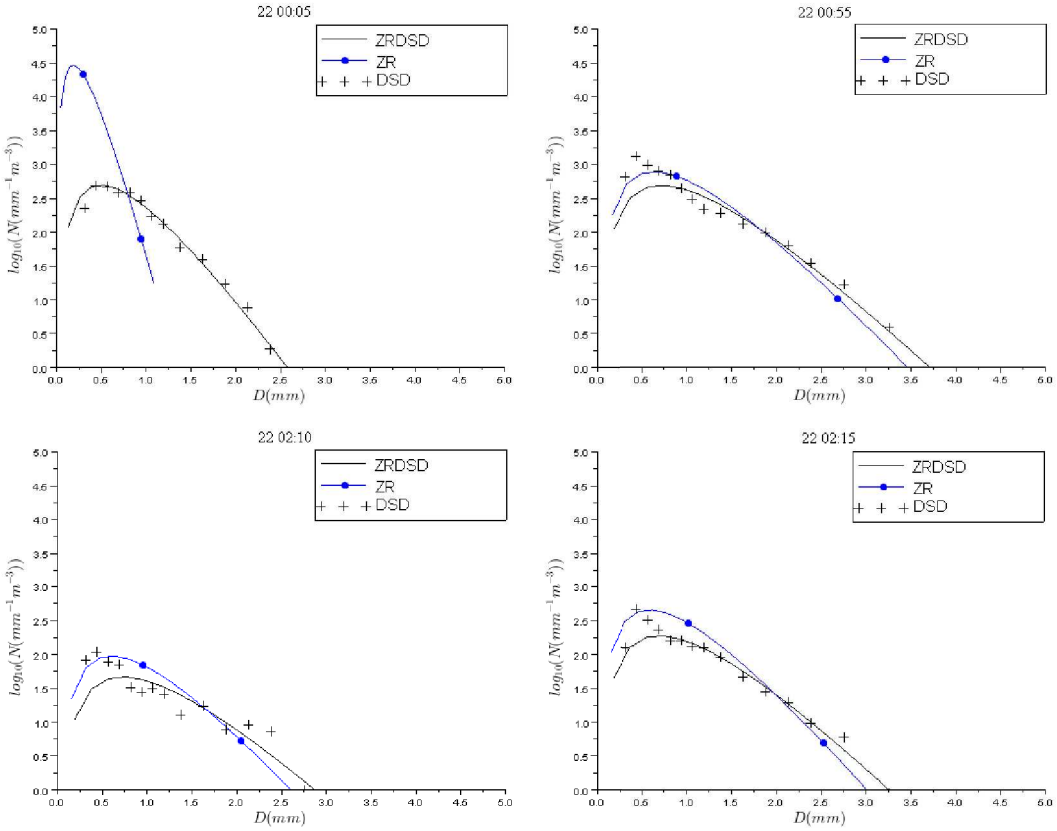

Figure 4.17: Reconstitutions of 4 DSDs by the rain intensity and reflectivity factor. - The rain intensity and reflectivity factor are derived from the disdrometer (black lines) and derived from radar and raingauge observations (blue lines). The crosses represent the DSD observed by the disdrometer.

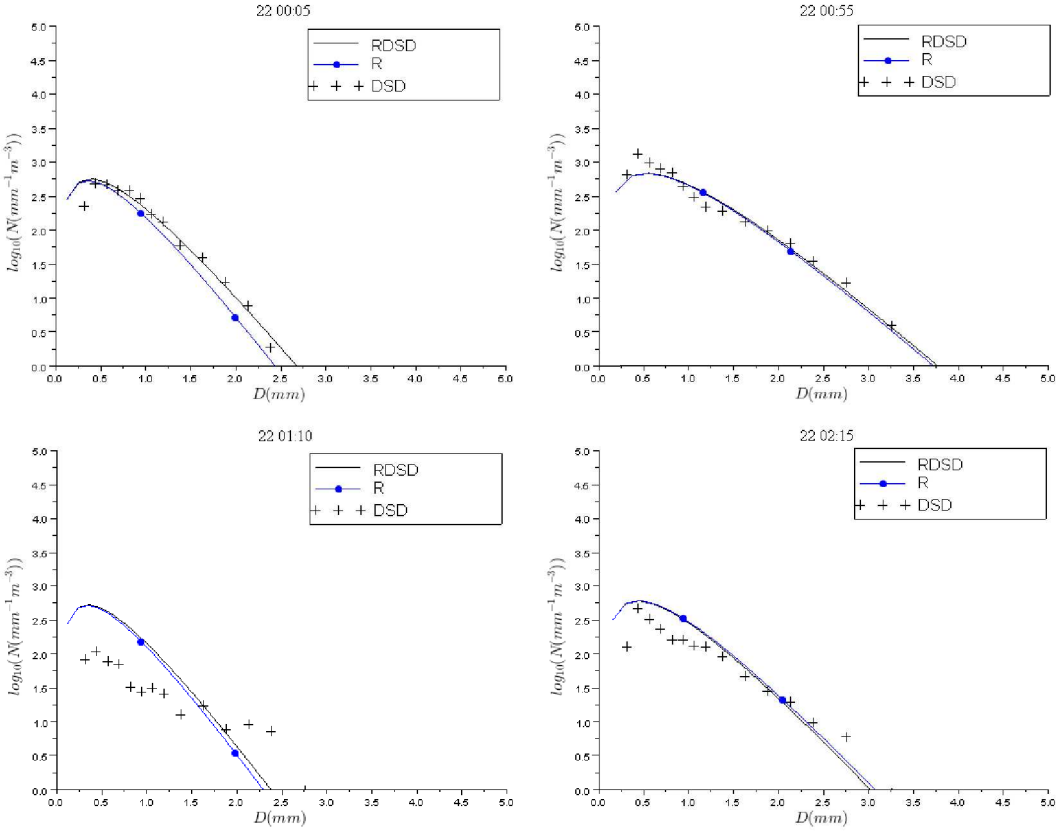

Figure 4.18: Reconstitutions of 4 DSDs by the rain intensity. - The rain intensity are derived from the disdrometer (black lines) and derived from raingauge observations (blue lines). The crosses represent the DSD observed by the disdrometer.

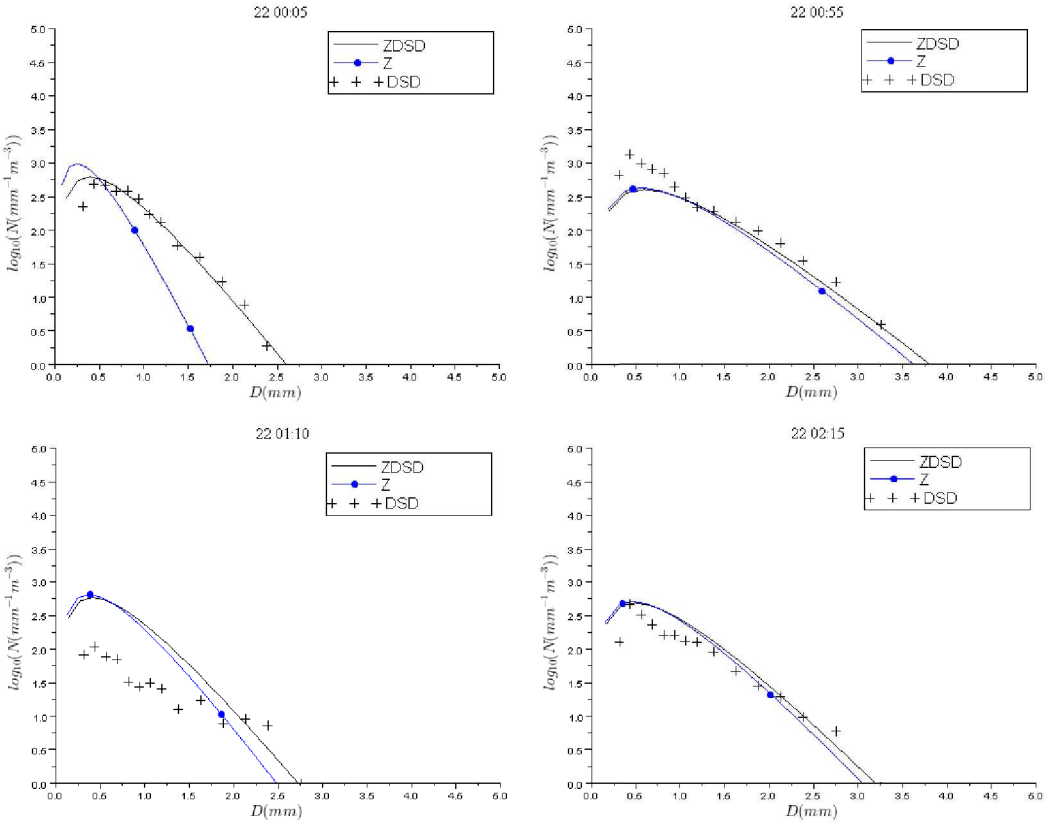

Figure 4.19: Reconstitutions of 4 DSDs by the reflectivity factor. - The reflectivity factor are derived from the disdrometer (black lines) and derived from radar (blue lines). The crosses represent the DSD observed by the disdrometer.

It seems that the sampling error of the radar becomes significant in this case. The third (bellow-left) DSD shows the advantage of the combination of R and Z together. Both the DSDs reconstituted by R or by Z separately overestimate the $N(D)$, while the reconstitution by R and Z together significantly reduces the bias between the DSD model and observation.

The whole event is then reconstituted based on the scaled DSD models (4.1) to (4.3). Four criteria ($Bias$, $Nash$, $RMSD$ and R) are used to evaluate the DSD models as a function of the drop diameter. In order to reduce the influence of the sampling error on the evaluation process, only the 5-min DSD records meeting the constraint that the three instruments detect the rainfall simultaneously are retained to evaluate the performance of the models. The moment(s) derived from the disdrometer and observed by the radar and raingauge are evaluated separately. Fig.4.20 shows the performance of DSD models reconstituted by the moments derived from the disdrometer. Similar to the results shown in Section 3.2.3, the DSD formulation scaled by two moments yields the best performance compared to that scaled by one moment. And the DSD model reconstituted by the reflectivity factor produces a better performance for the raindrops larger than 3 mm compared to the DSD model scaled by the rain intensity.

When the observations of rain gauge and/or radar are applied for the DSD reconstitution, similar behaviors of performance (Fig..4.21) are obtained. Radar reflectivity factor shows again an advantage in the reconstitution of large drops (D >3.5 mm) compared to the rain intensity. It seems that the combination of R and Z improves significantly the correlation between model and observations, but a large bias still exists due to the sampling and model error.

4.3 Estimation of the rainfall erosion energy

4.3.1 Introduction of the soil erosion by rainfall

Soil erosion due to rain is a major issue in the fields of agriculture, environment and water management. All studies on soil erosion have suggested that increased rainfall amounts and intensities will lead to greater rates of erosion e.g. Parry et al. (2007). In particular, rainfall kinetic energy has often been suggested as an indicator of rainfall erosivity (Fornis et al., 2005). Over the past decades, many numerical models of erosion processes have been developed, such as the Water Erosion Predicting Project

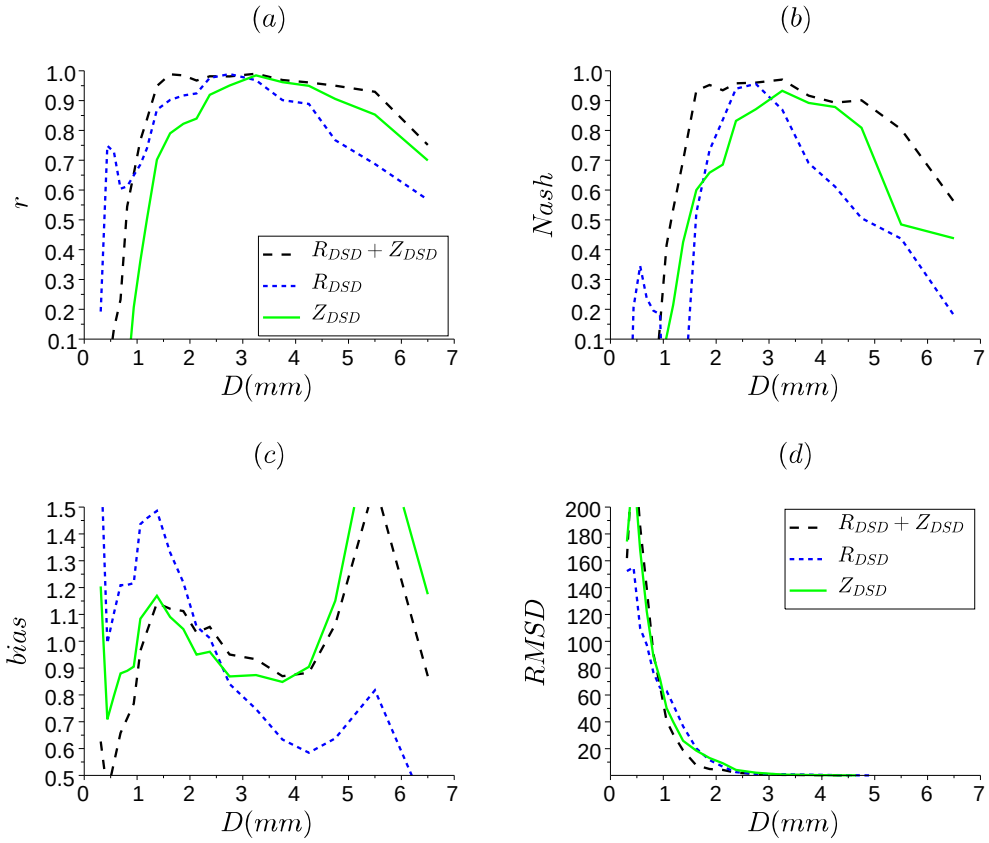

Figure 4.20: Evaluation of the DSD model reconstituted by Z, R and by R and Z together. - Coefficient correlation, $Nash$, $Bias$ and $RMSD$ are used to evaluate the modeled and observed $N(D)$. The Z and R are derived from the disdrometer.

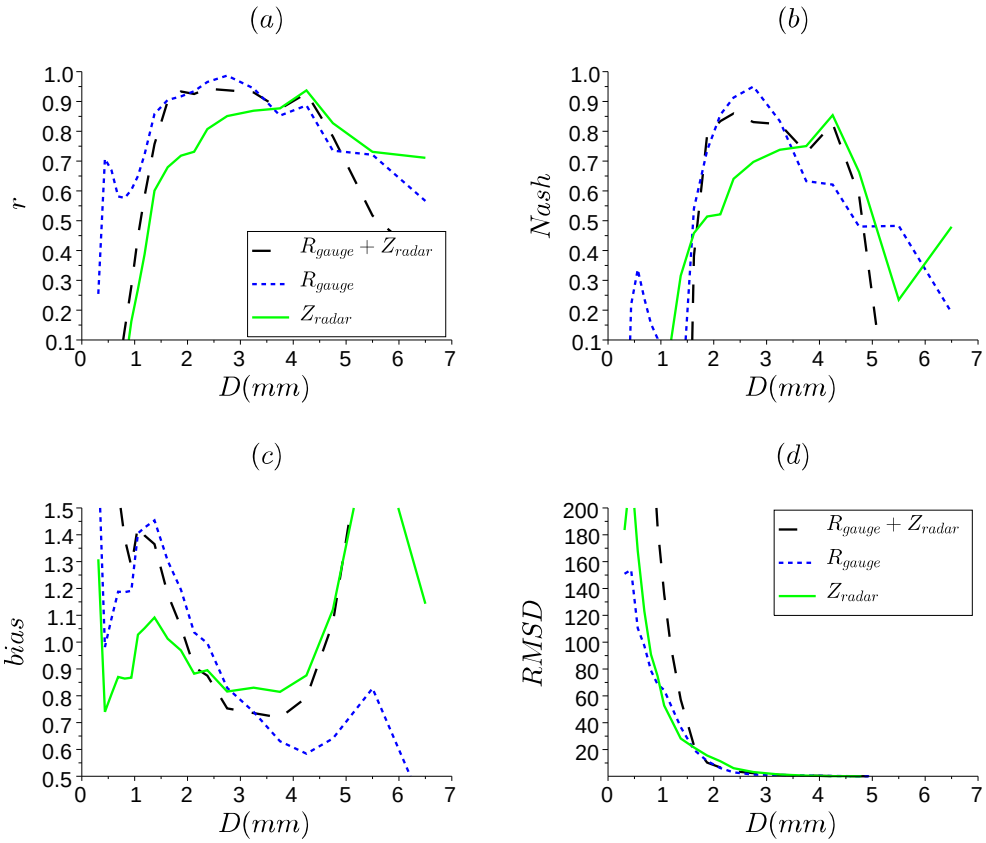

Figure 4.21: Evaluation of the DSD model reconstituted by Z, R and by R and Z together. - Coefficient correlation, $Nash$, $Bias$ and $RMSD$ are used to evaluate the modeled and observed $N(D)$. The Z and R are observed by radar and raingauge, respectively.

model (WEPP, Laflen et al. (1997)) and the European Soil Erosion model (EUROSEM, Morgan et al. (1998)). These models require rainfall time series with moderate to high temporal and spatial resolution (Van Dijk et al., 2005) which is a restriction due to the large rain variability and the limitation of rain gauge observations. The most common approach to estimate rainfall kinetic energy is by means of an empirical relationship between the kinetic energy flux density (KE) and rain intensity (R) (Kinnell, 1973; Mihara, 1951; Sempere Torres et al., 1992). Various mathematical expressions and parameterizations for the KE-R relationship have been presented in the literature. In order to study the physical interpretation behind different KE-R relationships, several mathematical distribution have been introduced to account for the variation in raindrop size distribution. Uijlenhoet and Stricker (1999) developed an approach to link KE to R based on the exponential DSD. Mualem and Assouline (1986) proposed a Weibull distribution with two parameters to derive the KE-R relationship. Their approach shows the advantages in the KE estimations for the light rainfall. In addition, the Weibull distribution conforms to the assumption that the DSD is determined mainly by breakup process rather than the initial DSD (Assouline and Mualem, 1989). Later, Salles et al. (2002) proposed a KE-R relationship based on the one-moment scaling formulation of the DSD. Their work suggested that the varying character of the DSD, which depends on the type of rain (convective or stratiform) and the geographical location, are the main factors explaining the variability of KE-R relationships. Fox (2004) investigated the theoretical KE-R relationships based on the gamma distribution (Ulbrich, 1983) and pointed out that the KE-R relationship is poorly defined unless some assumptions about the parameters of the gamma distribution are made. He also found that the assumption of an exponential DSD leads to an overestimation of the kinetic energy flux density. Additionally, to overcome the limitation of a rain gauge observation network, Steiner and Smith (2000) showed the potential advantage of radar reflectivity factor (Z) for estimating KE, which can provide detailed spatial and temporal information about rain storms.

The purpose of the current study is to investigate the KE-R, KE-Z and the KE-RZ relationships using the one-moment and two-moment scaling DSD formulations presented in the previous chapter. It is hoped that the radar reflectivity factor in combination with the rain rate can improve the estimation of rainfall kinetic energy.

In the literature, there are two raindrop kinetic energy variables proposed. One is the kinetic energy flux density per unit area per unit time, denoted KE hereafter, with units of $Jm^{-2}h^{-1}$, which expressed the rainfall energy on a unit surface during a unit time; the other is the kinetic energy flux density per unit area per unit depth (denoted KE_{mm} hereafter, with units of $Jm^{-2}mm^{-1}$), which is defined as the ratio between KE and the rain intensity R. Although the latter is most widely used in soil erosion studies, Salles et al. (2002) suggested that both from a theoretical and a practical point of view, the KE-R relationship should be used instead of the KE_{mm}-R relationship. They explained the preference for KE_{mm} in past studies by the non-automatic DSD observation techniques. Following Salles et al. (2002), we express the kinetic energy flux density per unit area per unit time (KE, $Jm^{-2}h^{-1}$) as

$$KE = 3 \times 10^{-7} \rho\pi \sum_i X(D_i) D_i^3 v_t^2(D_i), \tag{4.4}$$

where ρ is the water density ($kg\ m^{-3}$) in standard conditions; $X(D_i)$ ($drops\ m^{-2}s^{-1}$) is the number of raindrops of diameter D_i (mm) falling on a unit surface ($1\ m^2$) during a unit time interval ($1\ s$) and $v_t(D_i)$ (ms^{-1}) is the terminal velocity of a raindrop of diameter D_i. Converting the raindrop flux $X(D)$ into the raindrop concentration in a unit volume $N(D)dD$ (m^{-3}, with $N(D)$ in $mm^{-1}m^{-3}$ and dD in mm) through

$$X(D) = N(D) v_t(D) dD \tag{4.5}$$

and integrating over the raindrop diameter range yields

$$KE = 3 \times 10^{-7} \rho\pi \int_0^\infty N(D) D^3 v_t^3(D) dD. \tag{4.6}$$

The power law expression $v = 3.78D^{0.67}$ (1.2) discussed in Chapter 1 is considered in calculating the KE. Replacing the velocity by (1.2) yields a final formulation for the kinetic energy flux density as

$$KE = 5.09 \times 10^{-2} \int_0^\infty N(D) D^{5.01} dD, \tag{4.7}$$

which indicates KE is roughly proportional to the 5^{th} order moment of the DSD. This feature shows the potential advantages of the rain rate, proportional to the 3.67^{th} order moment, and the radar reflectivity factor, equal to the 6^{th} order moment, in estimating the KE separately or in conjunction.

4.3.2 Estimation of the KE based on DSD data

Considering the climatological expressions of moment relationships (3.18), (3.29) and (3.30), we obtain three KE estimators:

$$KE = 0.391R^{0.43}Z^{0.57}, \tag{4.8}$$

$$KE = 10.45R^{1.254}, \tag{4.9}$$

$$KE = 0.0912Z^{0.832}. \tag{4.10}$$

Salles et al. (2002) derived a similar expression as (4.9) and pointed out the range of possible exponents is between 1.0 and 1.4. They suggested the variation in the exponent is linked to the type of rain (convective or stratiform). Steiner and Smith (2000) obtained a climatological KE-Z relationship as $KE = 0.0536Z^{0.909}$ for the Northern Mississippi. It seems that the climatological KE-Z relationship is still related to the local characteristics of different regions.

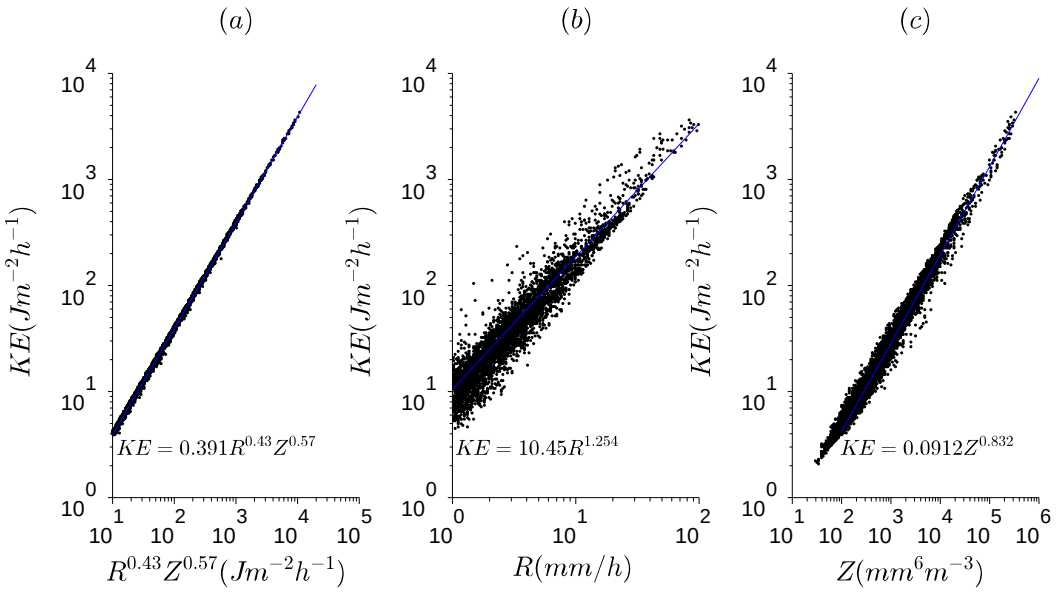

Figure 4.22: Reconstitutions the KE by the radar reflectivity factor and/or rain rate. - The KE, R and Z are derived from the 5-min DSD spectra.

Fig.4.22 displays the relationship between KE and predictor moment(s) (R and/or Z). One can immediately note the improvement in the estimation of KE when R and Z are used jointly. The three estimators (4.8), (4.9) and (4.10) are represented by the blue

lines in Fig.4.22, agreeing well with the observations. We recall that the kinetic energy is proportional to the 5^{th} moment of the DSD. Therefore the statistical evaluations of KE estimators based on the DSD dataset have been shown in the previous chapter in Fig.3.6, 3.16 and 3.15. The detailed criteria are listed in the Table.4.1. Generally, the three criteria exhibit the same trend. The two-moment estimator KE-RZ yields the best estimation of the KE. Concerning single-moment estimation, the radar reflectivity factor Z provides a better estimation than the rain rate R. This is mainly because the kinetic energy flux density is nearly proportional to the 5^{th} order moment, which is closer to the radar reflectivity factor (6^{th} order moment). The near perfect quality of the estimation from R and Z jointly shows the potential advantage of combining two moments that are widely accessible in hydrometeorological observation networks with radars and rain gauge.

Estimators	$Bias$	$RMSD$ $(Jm^{-2}h^{-1})$	$Nash$	r
KE_Z-KE_{DSD}	0.962	39.47	0.974	0.987
KE_R-KE_{DSD}	0.985	70.23	0.917	0.960
KE_{ZR}-KE_{DSD}	1.000	5.49	0.999	1.000

Table 4.1: Evaluation of the KE reconstituted by rain rate and/or radar reflectivity factor. The KE, R and Z are derived from the disdrometer.

Based on the scaled DSD formulations, three robust KE climatological estimators are obtained. However, only the disdrometer data measured by the disdrometer has been considered so far. Both the rain rate and radar reflectivity factor are calculated from the DSD. In order to illustrate a real application of the KE estimators, the following section is devoted to the KE estimation during a real rain event.

4.3.3 Application of the KE estimators on a rain event

Taking all types of errors (instrument error, sampling error, theoretical error, etc.) into account, one may question the performance of the estimated models in the operational application. To answer this question, the heavy rain event described and analyzed in Chapter 2 is selected to test three KE estimators. The disdrometer data, as a reference, serves only to calculate the kinetic energy flux density. The rain gauge and weather radar data are employed to estimate KE through the relationships (4.8), (4.9) and

(4.10). We illustrate the comparisons of estimated and observed KE time series in Fig.4.23. The estimated KEs are in good agreement with the observations.

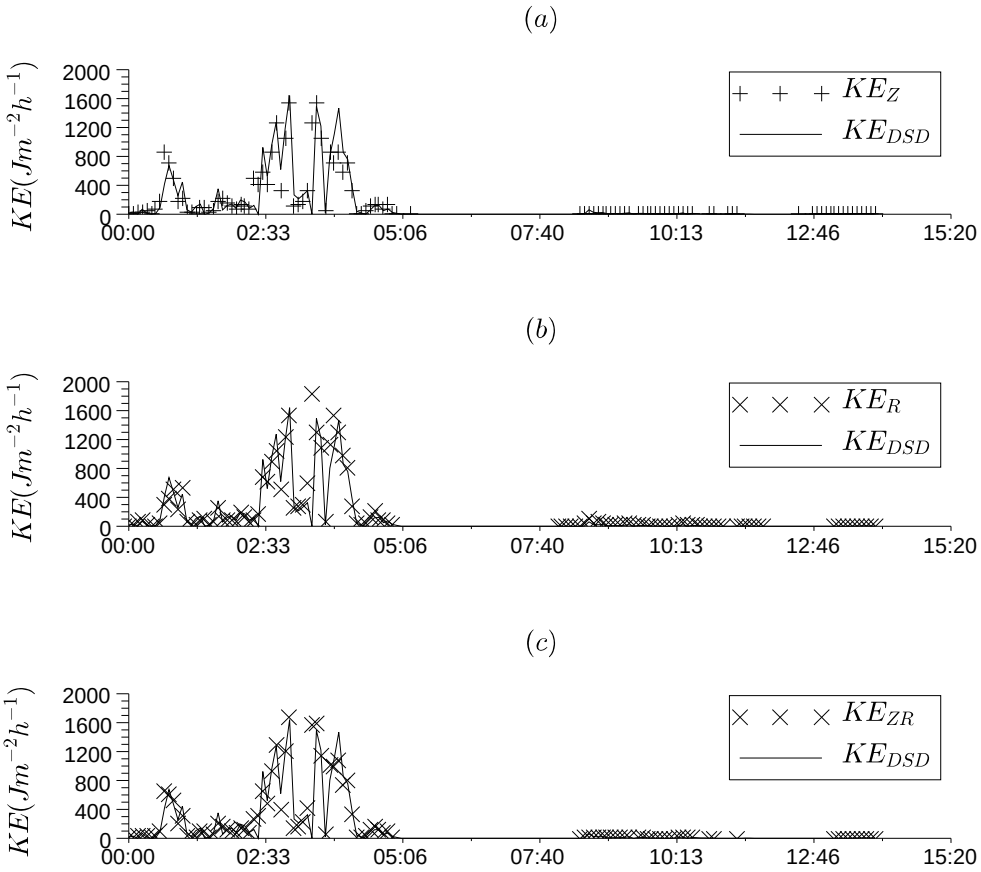

Figure 4.23: Time series of KE estimated by the radar reflectivity factor and/or rain rate. - The KE is derived from the 5-min DSD spectra, R and Z are obtained from the rain gauge and radar observations, respectively.

Detailed statistical comparison has been carried out. Due to different samplings and sensibilities of these instruments, a preliminary analysis focuses on the intermittency of rain intervals. We display a contingency table (Table.4.2), containing frequency counts of time steps in rain and no-rain categories, measured by different instruments. Overall, a good agreement can be found among these three instruments in consideration of the 5-minute time intervals. Because of the different sampling size, the weather radar measures more rain steps than the disdrometer. And the artificial rain steps observed by raingauge should be linked to the defect of interpolation model which constructs a

continue time series of rain intensity with the discrete tipping bucket rain gauge data. In order to simplify the comparison, only the 5-min intervals when all three instruments detect rainfall are taken into account in the following evaluation.

	Rain gauge >0	**Rain gauge =0**
Radar reflectivity >0	106	17
Radar reflectivity =0	23	50
	Disdrometer >0	**Disdrometer =0**
Radar reflectivity >0	104	19
Radar reflectivity =0	14	59
	Disdrometer >0	**Disdrometer =0**
Rain gauge >0	104	25
Rain gauge =0	14	53

Table 4.2: Contingency of time steps in rain and no-rain categories, measured by radar, raingauge and disdrometer.

In order to understand the errors in KE estimators, the DSD moments derived from the disdrometer and observed from the instruments (radar, raingauge) are evaluated in Table.4.3 and Table.4.4 for the rain event of 21-22 October 2008, respectively. The difference of the performance listed between Table.4.1 and Table.4.3 should be explained by the DSD model error. The application of the climatological DSD formulation on a particular intense rain event introduces the model error into the KE estimations. Nevertheless, except for the bias (0.912) when reflectivity factor is used in the estimation, the other criteria listed in Table.4.3 are similar to those listed in Table.4.1, which suggests that the main estimation error may be not caused by the model. From the Table.4.3 to Table.4.4, the sampling error is added in the estimation procedure. In addition, the comparisons of the rain rate provided by disdrometer and raingauge, as well as the reflectivity factor provided by disdrometer and radar, are demonstrated in Table.4.4 as well. Similar to the results presented in 4.3, the radar also yields an underestimation of KE (0.828), compared to that estimated by the rain gauge (1.022). One may note the negative bias (0.903) in the comparison of Z provided by the radar and by the disdrometer. It seems that the bias of the radar reflectivity with respect to the disdrometers reflectivity is amplified by the non-linear KE-Z relationship, while a slightly better agreement is obtained for the KE-R relationships. The improved perfor-

mance of the KE-R relationships may be explained by the proximity and the sampling characteristics of the disdrometer and the rain gauge, while the reflectivity measurements come from two very different sensors and resolution volumes. Nevertheless, in this case again, the KE-ZR relationship yields the better performance evaluated by the r and $Nash$ statistical criteria.

Estimators	$Bias$	$RMSD$ $(Jm^{-2}h^{-1})$	$Nash$	r
KE_Z-KE_{DSD}	0.912	52.95	0.982	0.998
KE_R-KE_{DSD}	0.978	48.17	0.985	0.994
KE_{ZR}-KE_{DSD}	1.002	4.22	1.000	1.000

Table 4.3: Evaluation of the KE reconstituted by rain rate and/or radar reflectivity factor derived from the disdrometer, for the rain event of 21-22 October 2008.

Estimators	$Bias$	$RMSD$ $(Jm^{-2}h^{-1})$	$Nash$	r
KE_Z-KE_{DSD}	0.828	131.10	0.887	0.953
KE_R-KE_{DSD}	1.022	93.97	0.942	0.972
KE_{ZR}-KE_{DSD}	0.933	77.97	0.960	0.981
Z_{DSD}-Z	0.903	7964.70	0.903	0.952
R_{DSD}-R	1.020	2.81	0.956	0.983

Table 4.4: Evaluation of the KE reconstituted by rain rate and/or radar reflectivity factor measured by the raingauge and weather radar, for the rain event of 21-22 October 2008.

4.3.4 Toward the spatialization of rainfall kinetic energy flux density

We have considered in the previous section one of the most intense events out of the 28-month time series which occurred on 22 October 2008. However, only the disdrometer data at one point have been considered so far. Hereafter, (i) we illustrate the potential of weather radar to deliver high resolution KE maps thanks to the radar reflectivity factor fields, (ii) then we compare the statistical distributions of the KE values derived from the three climatological relationships (4.8), (4.9) and (4.10) using weather radar data (Z) and/or the rain rate (R) provided by the 5-min raingauge network.

A direct conversion of the 5-min radar reflectivity available for the 22 October 2008 rain event using (4.10) yields high-resolution images (1 km^2, 5-min) of KE values such as those displayed in Fig.4.24 during the most intense part of this rain event. The large spatial and temporal variability of the kinetic energy are particularly remarkable for this event. Used in conjunction with GIS layers concerning topography, soil properties and land-use, we believe such KE images to have a strong potential for a better understanding of erosion processes.

As part of the available raingauge network supported by the French Flood Forecasting Service SPC-GD, we were able to collect 5-min rain rate time series for the 12 raingauges indicated in Fig.4.24. Not that the KE value derived form each 5-min rain rate value through (4.9) is used to define the color of the raingauge pictogram in accordance with the KE scale. The four selected images in Fig.4.24 show a good overall agreement between the radar- and raingauge-derived KE values, with some exceptions that may be due, among many other reasons, to timing problems and sampling issues for such fine scale comparisons.

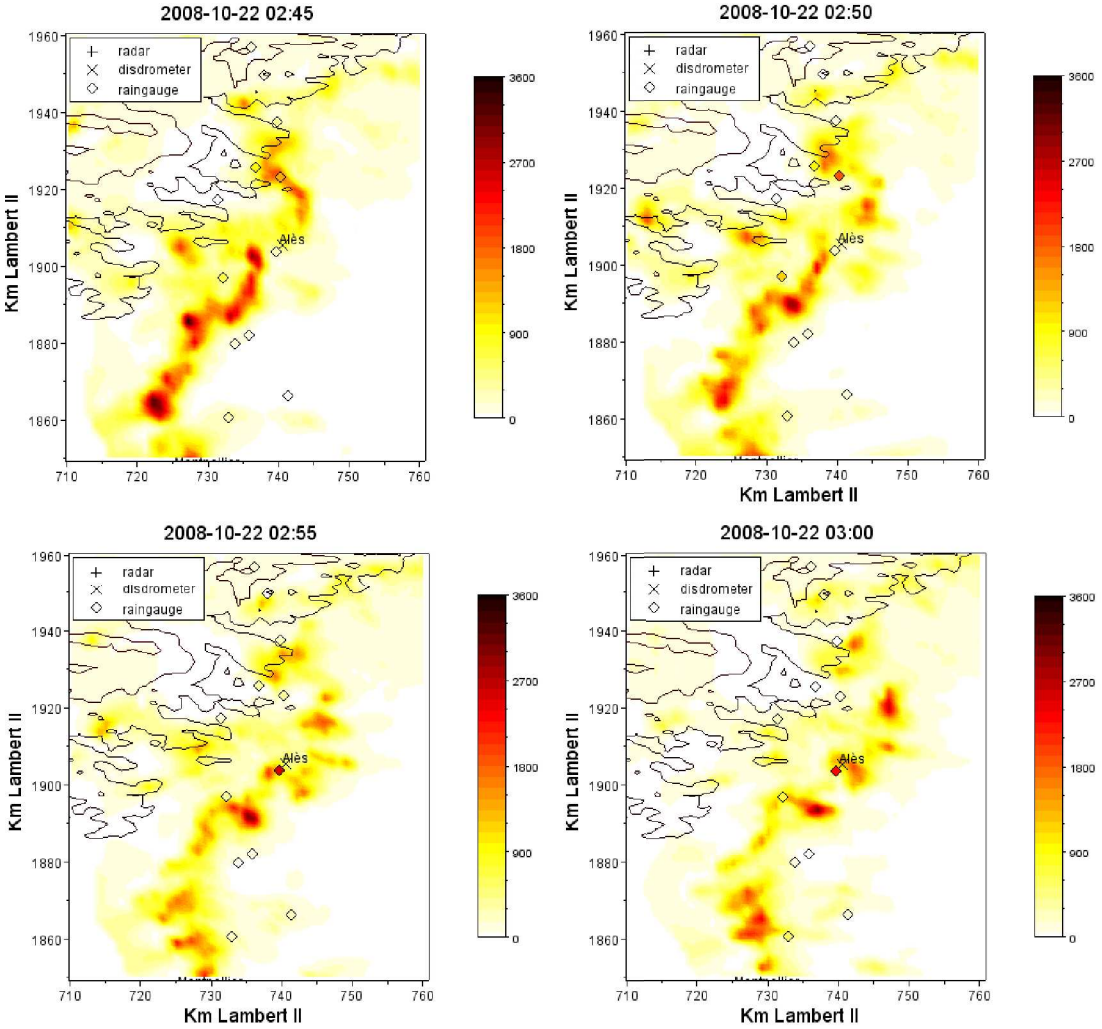

Figure 4.24: Maps of the kinetic energy flux density KE ($Jm^{-2}h^{-1}$) derived from Z in the region of Alès, at 0245UTC, 0250UTC, 0255UTC and 0300UTC, 22/10/2008. - The raingauge pictograms are colored as a function of the KE values derived from the observed rain rate.

Chapter 5

Conclusion and prospective

The DSD is a fundamental descriptor both for the rain microphysical processes and the macroscopic physical properties in order to characterize different precipitation systems and determine the macroscopic rain variables relationships for quantitative rainfall remote sensing. A comprehensive framework for parameterizing the raindrop size distribution has been presented in this PhD thesis. In this chapter, we summarize and comment the main results obtained, before discussing the prospective of this work.

5.1 Investigation of the intra-event variability through the scaling DSD formulation

The principle component analysis (PCA) was preliminarily performed on the log-transformed DSD moments. The results highlighted the need for at least two independent variables to describe the variation of the raindrop size distribution (99.5% of the variance is explained by the first two PCAs). The interpretation of the two first PCAs suggested the importance of the middle and low order moments (such as M_4 and M_0) for the representation of the DSD variability.

Next, the DSD scaling formulation was introduced by considering the DSD as the product of the number concentration N_t times a probability density function, denoted $g(x)$, of the diameter scaled by a characteristic diameter (x=D/D_c). A gamma model with two dimensionless parameters was used to model the so-called general distribution $g(x)$. Choosing a particular characteristic diameter as the ratio of the 4^{th} and 3^{rd} order moments of the DSD results in a self-consistency relationship between the two parameters λ and μ of the gamma *pdf* model. The general distribution is thus practically parameterized by a single dimensionless shape parameter (μ). The parameter estimation was performed by using (1) three appropriate moments M_0, M_3 and M_4, or (2) by using the whole observed moments from M_0 to M_6 (the so-called"all-moments estimator"). The scaling formulation associated with the two parameter estimators was implemented over a 3-year DSD observations corresponding to a large variety of convective types of precipitation (shallow convection forced by orography, thunderstorms, mesoscale convective systems). Note that the the 3-moment estimator can be implemented both for individual spectrum and for a series of DSD spectra

The results showed the DSD scaling model with the gamma *pdf* is in good agreement with the disdrometer observations, both for individual spectrum and for series of spectra. As a refinement, the truncation of the DSDs for minimum and maximum diameters, D_{min} and D_{max}, was studied and did not prove to be a very sensitive matter For series of spectra, the parameters estimated by two estimators are similar to each other. However, the 3-year general distribution exhibit a very large variability which can be partly explained by the shape parameter (μ). This suggests that variation in the DSD shape cannot be reduced by the current scaling technique and that the shape parameter μ may be related to physical processes.

The climatological DSD characteristics of the Cévennes rainfall are revealed by the histograms of three DSD parameters. For most of the 5-min DSD spectra, the number of raindrops is less than 1000 m^{-3} with characteristic diameters ($D_c = M_4/M_3$) between 1.0 and 1.5 mm. Regarding the shape parameter, (1) the distribution of μ is positively skewed, with a mode equal to 2.5, and (2) a limited fraction of negative (5%) and high μ-values (less than 15% for μ >10) is observed.The first point suggests that most of the 5-min scaled DSDs possess the gamma convex shape, rather than an exponential one. In addition, it was found that the number concentration is independent of both the D_c and the μ parameters. This is an important result regarding the DSD scaling formulation as the product of two independent terms (concentration and size distribution).

5.2 Extension of the scaling DSD formulation to include the one- and two-moment parameterization

The scaling DSD formulation based on N_t, D_c and μ was extended to account for the one- and two-moment DSD formulations proposed in a rather "unorganized" way in the literature. This was done by introducing single and dual power-law models between reference (or explanatory) moments (e.g. rain rate and/or radar reflectivity factor) and the explained moments (total concentration, characteristic diameter). In a way analogous to the (N_t, D_c, μ) DSD formulation, two parameter estimators based on 1) regression analyses of single and dual power-law models (the so-called "regression estimator") and 2) multiple DSD moments from the 0^{th} to 6^{th} moments (the so-called "all-moment estimator"). In both procedures, we made the best use of the self-consistency relationships which exist due to the fact that the moments are function of the DSD which is itself parameterized as a function of moments. Compared to the most elaborated DSD formulations presented in the literature, our approach explicitly accounts for the prefactors of the power-law models to produce a uniform and dimensionless scaled distribution, whatever the reference moment(s) considered.

The evaluation performed using the 3-year disdrometer dataset yields the following conclusions. Firstly, the two estimators have similar performance for the two-moment scaling DSD formulation. Regarding the one-moment scaling DSD formulation, the estimator has a significant impact on parameters. The "all-moments" estimator underestimates the shape parameter (μ) in R-scaling DSD formulation, but overestimates it

in the Z-scaling DSD formulation, compared to the "regression" estimator. However, the evaluation indicates that there is no preference to select any estimator to construct a climatological scaling DSD formulation. In this investigation, the "all-moment" estimator and the "regression" estimator were selected for R- and Z-scaling formulation, respectively, because of our interests for high order moments of the DSD. Secondly, the choice of the scaling moment(s) has a direct influence on DSD model performance. The model scaled by radar reflectivity factor yields a good performance for the large drops (3 $mm < D <$5 mm) at the cost of a poor correlation for the small drops ($D <$2 mm), while the model scaled by rain intensity is able to better represent the variation of middle size drops (1 $mm < D <$4 mm). Finally, a significant improvement of the model performance is obtained if two reference moments are considered in the scaling formulation. For the DSD formulation scaled by R and Z jointly, the variation of the raindrops between 1 mm and 5 mm are well represented by the model.

Thanks to the definition and the parameter estimators of the general distribution, our approach provides the possibility to compare the $g(x)$ functions obtained by different moment(s). A rather good agreement was observed whatever the moment(s) used, even in the case of the climatological dataset which, as already mentioned, exhibit a large variability. Applying the methods to more homogeneous DSD spectra proved to be very efficient in terms of convergence of the estimators, whatever the moment(s) used. Obviously, the spectra with large drops seem to be better scaled by the high order moment and the variation in small raindrops is reduced if low order moments are considered in the scaling process.

5.3 Applications of the scaling DSD formulations

The improvement of the two-moment DSD model performance was confirmed by an investigation of a rain event in which weather radar data and raingauge observations were available. This suggests the advantage of using two observations (moments) jointly in DSD studies regardless the different sampling characteristics of different instruments.

The scaling DSD formulation with three parameters (concentration, characteristic diameter and shape parameter) was applied to analyze the intra-event DSD variability of an intense rainfall event which occurred in October 2008. It was found that the variation in the DSD is well linked to the weather processes. The DSD in the edge of the

convective system possessed a different behavior compared to that in the center of the convective area. Hence, the movement of the convective system towards the disdrometer led to different DSD phases recorded in time series. Three typical rain phases were identified during the rain event: 1) a DSD with high concentration (1000 mm^{-3}) and large characteristic diameter (2.0 mm) in the forward edge of convective system; 2) a DSD with higher concentration (1500 mm^{-3}) and larger characteristic diameter (2.0 mm) in the center of convective area; 3) a drizzle precipitation with the highest number concentration (3000 mm^{-3}) but a small D_c (0.5 mm). The scaled distribution exhibits different behaviors in these phases. It seems that the shape parameter decreases with the intensity of the convective activity.

The intra-event variation in DSD is well associated with the weather radar signals. The vertical reflectivity profile, the Doppler vertical velocity are good indicators for the identification of rain phases. In particular, the maximum value of the reflectivity factor as a function of the altitude was found to be approximately linearly related with the characteristic diameter for D_c >1 mm. However, the detailed polarimetric measurement did not prove to be useful for the considered event due to the high noise contained in the signals.

This study presents also the estimation of rainfall kinetic energy flux density (KE) from rain intensity and/or radar reflectivity factor based on climatological DSD scaling formulations. In the case of one-moment estimation, as Z (the 6^{th} order moment) is close to KE (which is proportional to the 5^{th} order moment), Z theoretically yields better estimation than the KE-R relationship. However, for the considered radar-raingauge dataset, due to radar sampling problems and/or calibration problems and the fact that the raingauge is collocated with the disdrometer, the performance of KE-R relationship was better than that of the KE-Z relationship. The performance of the estimation can be improved when rain gauge data are used jointly with radar reflectivities in the estimation. Here again, the KE estimate highlights the advantage of combining two observations to estimate a third DSD moment.

5.4 Prospective

5.4.1 Improving the DSD formulation

The research described in this thesis has shown that the gamma probability function is suitable to parameterize the DSD scaled by the concentration. As already evoked by Lee et al. (2004), a generalized gamma *pdf* distribution (2.12) could provide an increased flexibility for the DSD fitting at the cost of having to estimate an additional shape parameter.

The 0^{th} order moment is known to be measured with quite a large uncertainty due to the instrumental error for the small drops. Two potential solutions are provided for the further research: The concentration could be substituted by the liquid water content per unit air volume LWC (kgm^{-3}) through the moment relationship (2.14), as

$$LWC = \frac{\pi\rho}{6} M_3 = \frac{\pi\rho}{6} \frac{\Gamma(\mu+4)}{\Gamma(\mu+1)} \frac{N_t D_c^3}{\lambda^3}. \tag{5.1}$$

Substituting the expression of N_t derived from (5.1) into the original scaling DSD formulation (2.12) yields

$$N(D) = \left[\frac{6\Gamma(\mu+1)\lambda^3}{\pi\rho\Gamma(\mu+4)} \frac{LWC}{D_c^4}\right] \left[\frac{\lambda^{\mu+1}}{\Gamma(\mu+1)} (D/D_c)^{\mu} exp(-\frac{\lambda D}{D_c})\right] \tag{5.2}$$

Besides the diameter D and the two parameters μ and λ, the DSD depends now on two physical variables, namely the liquid water content LWC and the characteristic diameter D_c, which are related to the 3^{rd} and 4^{th} order moments of the DSD. These two moments are assumed to be better measured by the disdrometer compared to M_0. However, this formulation has one disadvantage: the first term of equation (5.2) contains also the parameter μ, which is somewhat opposite to the concept that the DSD is the product of two independent terms (the concentration and the *pdf* of the scaled diameter). So practically, the M_0 measurement problem would be replaced by an "increased confidence" in the modeling and a possible "built-dependence" between the concentration and the size distribution.

An alternative solution is to change the definition of the raindrop size distribution. Instead of the drop concentration as a function of the diameter, one may consider the distribution of another moment M_i as a function of the diameter (D) and a new general distribution may be defined as

$$M_i(D) = (M_i/D_c) f(D/D_c) \tag{5.3}$$

In fact, $N(D)$ can be considered as a particular case of $M_i(D)$ when i=0. Based on the results shown in Fig.2.18, the gamma function may no longer be able to represent the $f(x)$ function if i >0. It may be interesting to review the current formulation based on $N(D)$ for the $M_i(D)$ case.

5.4.2 Hydrometeorological applications

At the end of this thesis, a large amount of work remains to be done about the establishment of a climatology of the DSD in the Cévennes region and about the subsequent derivation of relationships between the rain intensity and various radar measurables, to be conditioned on the weather regimes. Both the 3D conventional and polarimetric radar data may help in this prospective. Thanks to the physically meaningful parameters used in the scaling DSD formulation, one can expect improved retrieval algorithms for the further DSD research. One of the issues to be addressed will be the "change of scale" problem between the sampling volume of the disdrometer to that of the radar. We hope the scaling formulation to be an efficient approach for this difficult problem. The experiments to be realized in the CVMHO pilot site during the HyMeX enhanced observation period will provide (hopefully) the detailed datasets to progress on these critical issues.

In addition, following the work realized about the kinetic energy, we believe that an interesting work can be done regarding the high-resolution spatial and temporal estimation of KE based on R and Z measurements using geostatistical techniques such as Kriging with external drift. Utilizing such rainfall estimations to force distributed hydro-sedimentary models with a detailed description of the landscapes (topography, lithology, land-use) of the watershed is likely to provide a new impetus to erosion studies. Enhanced validation will be possible in the context of the HyMeX EOP thanks to the high-resolution DSD measurements which will be collected both in the Cévennes and the Alpine regions.

References

Assouline, S. and Y. Mualem, 1989: The similarity of regional rainfall : a dimensionless model of drop size distribution. *Transactions of the ASAE*, **32(4)**, 1216–1222. 119

Atlas, D. and C. W. Ulbrich, 1977: Path- and area- integrated rainfall measurement by microwave attenuation in the 1-3 cm band. *J. Appl. Meteor.*, **16**, 1322–1331. 7, 8

Atlas, D. and C. W. Ulbrich, 2000: An observationally based conceptual model of warm oceanic convective rain in the tropics. *J. Appl. Meteorol.*, **39 (12)**, 2165–2181. 11

Atlas, D., C. W. Ulbrich, F. D. Marks, R. A. Black, E. Amitai, P. T. Willis, and C. E. Samsury, 2000: Partitioning tropical oceanic convective and stratiform rains by draft strength. *J. Geophys. Res., [Atmos.]*, **105**, 2259–2267. 8

Beard, K. V., 1976: Terminal velocity and shape of cloud and precipitation drops aloft. *J. Atmos. Sci.*, **33**, 851–864. 7

Beard, K. V., D. B. Johnson, and D. Baumgardner, 1986: Aircraft observations of large raindrops in warm, shallow, convective clouds. *Geophys. Res. Lett.*, **13**, 991–994. 11

Best, A. C., 1950: Empirical formulea for the terminal velocity of water drops falling through the atmosphere. *Quart. J. Roy. Meteor. Soc.*, **76**, 302–311. 7

Boudevillain, B., G. Delrieu, B. Galabertier, L. Bonnifait, L. Bouilloud, P. E. Kirstetter, and M. L. Mosini, 2011: The Cévennes-Vivarais Mediterranean hydrometeorological observatory database. *Water Resour. Res.*, **47**, W07 701. 23

Bougeault, P. and Coauthors, 2001: The MAP special observing period. *Bull. Amer. Meteor. Soc.*, **82**, 433–462. 12

Brandes, E. A., G. F. Zhang, and J. Vivekanandan, 2003: An evaluation of a drop distribution-based polarimetric radar rainfall estimator. *J. Appl. Meteorol.*, **42 (5)**, 652–660. 9

Bringi, V. N. and V. Chandrasekar, 2001: *Polarimetric Doppler Weather Radar: Principles and Applications*. Cambridge University Press, 636 pp. 27

REFERENCES

Bringi, V. N., G. J. Huang, V. Chandrasekar, and E. Gorgucci, 2002: A methodology for estimating the parameters of a gamma raindrop size distribution model from polarimetric radar data: Application to a squall-line event from the TRMM/Brazil campaign. *J. Atmos. Oceanic Technol.*, **19 (5)**, 633–645. 28

Browne, I. C. and N. P. Robinson, 1952: Cross-polarization of the radar melting-band. *Nature*, **170**, 1078–1079. 10

Cao, Q. and G. F. Zhang, 2009: Errors in estimating raindrop size distribution parameters employing disdrometer and simulated raindrop spectra. *J. Appl. Meteor. Climatol.*, **48**, 406–425. 48

Chandrasekar, V. and V. N. Bringi, 1987: Simulation of radar reflectivity and surface measurements of rainfall. *J. Atmos. Oceanic Technol.*, **4 (3)**, 464–478. 9

Chapon, B., G. Delrieu, M. Gosset, and B. Boudevillain, 2008: Variability of rain drop size distribution and its effect on the Z - R relationship: A case study for intense mediterranean rainfall. *Atmos. Res.*, **87 (1)**, 52–65. 13, 14, 20, 23, 88

Chu, Y. H. and C. L. Su, 2008: An investigation of the slope-shape relation for gamma raindrop size distribution. *J. Appl. Meteor. Climatol.*, **47 (10)**, 2531–2544. 9

Delrieu, G., et al., 2005: The catastrophic flash-flood event of 8-9 september 2002 in the Gard region, France : A first case study for the Cévennes-Vivarais Mediterranean hydrometeorological observatory. *J. Hydrometeor*, **6 (1)**, 34–52. 23, 24

Duffourg, F. and V. Ducrocq, 2011: Origin of the moisture feeding the heavy precipitating systems over southeastern France. *Nat. Hazards Earth Syst. Sci.*, **11**, 1163–1178. 96

Erpul, G., L. D. Norton, and D. Gabriels, 2002: The effect of wind on physical raindrop impact and rainsplash detachment. *Transactions of the ASABE.*, **45(6)**, 51–62. 7

Fabry, F. and I. Zawadzki, 1995: The melting layer of precipitation: radar observations and their interpretation. *J. Atmos. Sci.*, **52**, 828–851. 11

Fornis, R. L., H. R. Vermeulen, and J. D. Nieuwenhuis, 2005: Kinetic energy-rainfall intensity relationship for Central Cebu, Philippines for soil erosion studies. *J. Hydrol.*, **300**, 20–32. 116

Fox, N. I., 2004: The representation of rainfall drop-size distribution and kinetic energy. *Hydrol. Earth Syst. Sci.*, **8 (5)**, 1001–1007. 119

Fujiwara, M. and T. Yanase, 1968: Raindrop Z-R relationships in different altitudes. *Proc. 13th Radar Meteorology Conf. Montreal, QC, Canada*, Amer. Meteor. Soc., 380–383. 21

Gamache, J. F., 1990: Microphysical observations in summer MONEX convective and stratiform clouds. *Mon. Wea. Rev.*, **118(6)**, 1238–1249. 11

Godart, A., S. Anquetin, and E. Leblois, 2009: Rainfall regimes associated with banded convection in the Cévennes-Vivarais area. *Meteorol. Atmos. Phys.*, **103**, 25–34. 3

Gossard, E. E., D. C. Strauch, D. C. Welsh, and S. Y. Matrosov, 1992: Gloud layer, particle identification, and rain rate profiles from Z RVf measurements by clean-air Doppler radar. *J. Atmos. Oceanic Technol.*, **9**, 108–119. 7

Gultepe, I. and J. A. Milbrandt, 2010: Probabilistic parameterizations of visibility using observations of rain precipitation rate, relative humidity, and visibility. *J. Appl. Meteor. Climatol.*, **49 (1)**, 36–46. 23

Gunn, R. and G. R. Kinzer, 1949: The terminal velocity of fall for water drops in stagnant air. *J. Meteorol*, **6**, 243–248. 7

Haddad, Z. S. and D. Rosenfeld, 1997: Optimality of empirical Z-R relations. *Quart. J. Roy. Meteor. Soc.*, **123 (541, Part A)**, 1283–1293. 33

Haddad, Z. S., D. A. Short, S. L. Durden, I. M. Eastwood, S. Hensley, M. B. Grable, and R. A. Black, 1997: A new parametrization of the rain drop size distribution. *IEEE Trans. Geosci. Remote Sens.*, **35 (3)**, 532–539. 33

Handwerker, J. and W. Straub, 2011: Optimal determination of parameters for gamma -type drop size distributions based on moments. *J. Atmos. Oceanic Technol.*, **28**, 513–529. 48

Hazenberg, P., N. Yu, B. Boudevillain, G. Delrieu, and R. Uijlenhoet, 2011: Scaling of raindrop size distributions and classification of radar reflectivity-rain rate relations in intense Mediterranean precipitation. *J. Hydrol.*, **402 (3-4)**, 179–192. 42, 77

Hooper, J. E. N. and A. A. Kippax, 1950: The bright band - a phenomenon associated with radar echoes from falling rain. *Quart. J. Roy. Meteor. Soc.*, **76**, 125–132. 10

Houze, R., 1993: *Cloud Dynamics*, Vol. 53. Academic Press, 573 pp. 10

Hu, Z. and R. C. Srivastava, 1995: Evolution of raindrop size distribution by coalescence, breakup, and evaporation: Theory and observations. *J. Atmos. Sci.*, **52 (10)**, 1761–1783. 21

Huet, P., P. Foin, C. Laurain, and P. Cannard, 2003: *Retour d'expérience des crues de septembre 2002 dans les départements du Gard, de l'Hérault, du Vaucluse, des Bouches-du-Rhône, de l'Ardèche et de la Drôme : rapport consolidé après phase contradictoire.* MEDD-IGE, 233 pp. 3

Illingworth, A. J. and T. M. Blackman, 2002: The need to represent raindrop size spectra as normalized gamma distributions for the interpretation of polarization radar observations. *J. Appl. Meteorol.*, **41 (3)**, 286–297. 9, 22

Jaffrain, J. and A. Berne, 2011: Experimental quantification of the sampling uncertainty associated with measurements from PARSIVEL disdrometers. *J. Hydrometeor.*, **12 (3)**, 352–370. 7, 23

Johnson, D. B., 1982: Raindrop multiplication by drop breakup. *J. Appl. Meteor.*, **21(7)**, 1048–1052. 11

Johnson, D. B., K. V. Beard, and D. Baumgardner, 1986: Airborne observations of raindrop size distribution in Hawaiian cloud. *Conf. on Cloud Physics, Snowmass, CO*, Amer. Meteor. Soc., 48–51. 11

Joss, J. and E. G. Gori, 1978: Shapes of raindrop size distributions. *J. Appl. Meteorol*, **17**, 1054–1061. 8

Joss, J. and A. Waldvogel, 1970: A method to improve the accuracy of radar-measured amounts of precipitation. *Proc. 14th Radar Meteorology Conf., Tucson, AZ.*, Amer. Meteor. Soc., 237–238. 20

Kim, D. S., M. Maki, and D. I. Lee, 2010: Retrieval of three-dimensional raindrop size distribution using X-band polarimetric radar data. *J. Atmos. Oceanic Technol.*, **27(8)**, 1265–1285. 28

Kinnell, P. I. A., 1973: The problem of assessing the erosive power of rainfall from meteorological observations. *Soil Sci. Soc. Am. Proc.*, **37**, 617–621. 119

Laflen, J. M., W. J. Elliot, D. C. Flanagan, C. R. Meyer, and M. A. Nearing, 1997: WEPP predicting water erosion using a process-based model. *J. Soil Water Conserv.*, **52(2)**, 96–102. 119

Lee, G. and I. Zawadzki, 2005: Variability of drop size distributions: Time-scale dependence of the variability and its effects on rain estimation. *J. Appl. Meteorol.*, **44 (2)**, 241–255. 13

Lee, G., I. Zawadzki, W. Szyrmer, D. Sempere Torres, and R. Uijlenhoet, 2004: A general approach to double-moment normalization of drop size distributions. *J. Appl. Meteorol.*, **43 (2)**, 264–281. 9, 32, 33, 40, 67, 85, 134

Li, X., C. H. Sui, and K. M. Lau, 2002: Dominant cloud microphysical processes in a tropical oceanic convective system: a 2D cloud resolving modeling study. *Mon. Wea. Rev.*, **130**, 2481–2491. 11

Liu, Y. G., 1993: Statistical-theory of the Marshall-Palmer distribution of raindrops. *Atmos. Environ. A-GENERAL.*, **27 (1)**, 15–19. 8

Maki, M., T. D. Keenan, Y. Sasaki, and K. Nakamura, 2001: Characteristics of the raindrop size distribution in tropical continental squall lines observed in Darwin, Australia. *J. Appl. Meteorol.*, **40 (8)**, 1393–1412. 11

Marshall, J. S. and W. M. K. Palmer, 1948: The distribution of raindrops with size. *J. Meteor.*, **5**, 165–166. 8, 18

Martner, B. E., S. E. Yuter, A. B. White, S. Y. Matrosov, D. E. Kingsmill, and F. M. Ralph, 2008: Raindrop size distributions and rain characteristics in California coastal rainfall for periods with and without a radar bright band. *J. Hydrometeor*, **9(3)**, 408–425. 11, 20

Mihara, Y., 1951: Raindrops and soil erosion. *Bulletin of the National Institute of Agricultural Sciences, Japan*, **A1**, 48–51. 119

Moisseev, D. N. and V. Chandrasekar, 2007: Examination of the mu-Lambda relation suggested for drop size distribution parameters. *J. Atmos. Oceanic Technol.*, **24 (5)**, 847–855, doi: 10.1175/JTECH2010.1. 9

Mood, A. M., F. A. Graybill, and D. C. Boes, 1974: *Introduction to the Theory of Statistics*. 3d ed., McGraw-Hill Series in Probability and Statistics, McGraw-Hill Companies, New York, 564 pp. 40

Morgan, R. P. C., et al., 1998: The European soil erosion model (EUROSEM) : A dynamic approach for predicting sediment transport from fields and small catchments. *Earth Surf. Process. Landforms*, **23**, 527–544. 119

Morin, E., W. F. Krajewski, D. C. Goodrich, X. Gao, and S. Sorooshian, 2003: Estimating rainfall intensities from weather radar data: the scale - dependency problem. *J. Hydrometeor*, **4**, 782–797. 21

Mualem, Y. and S. Assouline, 1986: Mathematical model for rain drop distribution and rainfall kinetic energy. *Transactions of the ASABE.*, **29(2)**, 494–500. 119

Nuissier, O., V. Ducrocq, D. Ricard, C. Lebeaupin, and S. Anquetin, 2008: A numerical study of three catastrophic precipitating events over Southern France. I: Numerical framework and synoptic ingredients. *Quart. J. Roy. Meteor. Soc.*, **134**, 111–130. 3

Parry, M. L., O. F. Canziani, J. P. Palutikof, P. J. Van Der Linden, and C. E. Hanson, 2007: *Contribution of Working Group II to the Fourth Assessment Report of the Intergovernmental Panel on Climate Change*. Cambridge University Press, UK, 976 pp. 116

Petrocchi, P. J. and K. J. Banis, 1980: Computer analysis of raindrop disdrometers spectral data acquired during the 1979 SESAME project. *19th Radar Meteor. Conf. Boston*, Amer. Meteor. Soc., 490–492. 20

Porrà, J. M., D. Sempere Torres, and J. D. Creutin, 1998: Modeling of drop size distribution and its applications to rainfall measurements from radar. *Stochastic methods in hydrology: Rain, landforms and floods*, V. K. Gupta, O. E. Barndorff-Nielsen, V. Perez-Abreu, and E. Waymire, Eds., World Scientific, Singapore, 73–84. 40

Powell, M., 1964: An efficient method for finding the minimum of a function of several variables without calculating derivatives. *Computer Journal*, **7**, 155–162. 45, 46

Pradier, S., M. Chong, and F. Roux, 2004: Characteristics of some frontal stratiform precipitation events south of the Alpine chain during MAP. *Meteorol. Atmos. Phys.*, **87**, 197–218. 12

Pujol, O., J. F. Georgis, M. Chong, and F. Roux, 2005: Dynamics and microphysics of orographic precipitation during MAP IOP3. *Quart. J. Roy. Meteor. Soc.*, **131(611)**, 2795–2819. 12

Rauber, R. M., K. V. Beard, and B. M. Andrews, 1991: A mechanism for giant raindrop formation in warm, shallow, convective clouds. *J. Atmos. Sci.*, **48**, 1791–1797. 11

Rosenfeld, D. and I. M. Lensky, 1998: Spaceborne sensed insights into precipitation formation processes in continental and maritime clouds. *Bull. Amer. Meteor. Soc.*, **79**, 2457–2476. 12

Rosenfeld, D. and C. W. Ulbrich, 2003: Cloud microphysical properties, processes, and rainfall estimation opportunities. *Meteorological Monographs*, **30**, 237–237. 12, 13, 15, 16

Salles, C., 1995: Analyse microphysical de la pluie au sol: mesures par spectro-pluviometre optique et methods stattistiques d'analyse spectrale et de simulation numerique. Ph.D. thesis, Joseph Fourier University, Grenoble, France. 33

Salles, C. and J. D. Creutin, 2003: Instrumental uncertainties in Z-R relationships and raindrop fall velocities. *J. Appl. Meteorol.*, **42**, 279–290. 7

Salles, C., J. Poesen, and D. Sempere Torres, 2002: Kinetic energy of rain and its functional relationship with intensity. *J. Hydrol.*, **257 (1-4)**, 256–270. 119, 120, 121

Schultz, D. M., et al., 2002: Understanding Utah winter storms: The intermountain precipitation experiment. *Bull. Amer. Meteor. Soc.*, **83(2)**, 189–210. 12

Schumacher, C. and R. A. Houze, 2003: Stratiform rain in the tropics as seen by the TRMM precipitation radar. *J. Climate*, **16(11)**, 1739–1756. 20

Sekhon, R. S. and R. C. Srivastava, 1970: Snow size spectra and radar reflectivity. *J. Atmos. Sci.*, **27**, 299–307. 9, 44

Sempere Torres, D., J. M. Porrà, and J. D. Creutin, 1994: A general formulation for raindrop size distribution. *J. Appl. Meteorol.*, **33 (12)**, 1494–1502. 9, 40

Sempere Torres, D., J. M. Porrà, and J. D. Creutin, 1998: Experimental evidence of a general description for raindrop size distribution properties. *J. Geophys. Res., [Atmos.]*, **103 (D2)**, 1785–1797. 9, 76

Sempere Torres, D., C. Salles, J. D. Creutin, and G. Delrieu, 1992: Quantification of soil detachment by raindrop impact : performance of classical formulae of kinetic energy in Mediterranean storms. *Erosion and sediment transport monitoring programs in river basin, IASH Publ.*, **210**, 115–124. 119

Sharma, S., M. Konwar, D. K. Sarma, M. C. R. Kalapureddy, and A. R. Jain, 2009: Characteristics of rain integral parameters during tropical convective, transition, and stratiform rain at Gadanki and its application in rain retrieval. *J. Appl. Meteor. Climatol.*, **48**, 1245–1266. 20

Smith, J. A., E. Hui, M. Steiner, M. L. Baeck, W. F. Krajewski, and A. A. Ntelekos, 2009: Variability of rainfall rate and raindrop size distributions in heavy rain. *Water Resour. Res.*, **45 (4)**, W04 430. 48

Smith, P. L., 2009: Comments on "an investigation of the slope-shape relation for gamma raindrop size distribution". *J. Appl. Meteor. Climatol.*, **48 (9)**, 1994–1995, doi:10.1175/2009JAMC2157.1. 9

Smith, R. B., 1979: The influence of mountains on the atmosphere. *Adv. Geophys.*, **21**, 87–230. 3, 12

Steiner, M. and J. A. Smith, 2000: Reflectivity, rain rate, and kinetic energy flux relationships based on raindrop spectra. *J. Appl. Meteorol.*, **39 (11)**, 1923–1940. 119, 121

Steiner, M., J. A. Smith, and R. Uijlenhoet, 2004: A microphysical interpretation of radar reflectivity-rain rate relationships. *J. Atmos. Sci.*, **61 (10)**, 1114–1131. 18

Testud, J., S. Oury, R. A. Black, P. Amayenc, and X. K. Dou, 2001: The concept of "normalized" distribution to describe raindrop spectra: A tool for cloud physics and cloud remote sensing. *J. Appl. Meteorol.*, **40 (6)**, 1118–1140. 9, 22, 40, 42

Tokay, A. and D. A. Short, 1996: Evidence from tropical raindrop spectra of the origin of rain from stratiform versus convective clouds. *J. Appl. Meteorol.*, **35 (3)**, 355–371. 8, 11, 20

Tokay, A., R. Wolff, P. Bashor, and O. Dursun, 2003: On the measurement errors of the Joss-Waldvogel disdrometer. *31st Int. Conf. on Radar Meteorology*, Seattle, WA, Amer. Meteor. Soc., 437–440. 7

Uijlenhoet, R., J. A. Smith, and M. Steiner, 2003a: The microphysical structure of extreme precipitation as inferred from ground-based raindrop spectra. *J. Atmos. Sci.*, **60 (10)**, 1220–1238. 22, 40, 60

Uijlenhoet, R., M. Steiner, and J. A. Smith, 2003b: Variability of raindrop size distributions in a squall line and implications for radar rainfall estimation. *J. Hydrometeor.*, **4 (1)**, 43–61. 12, 40

Uijlenhoet, R. and J. N. M. Stricker, 1999: A consistent rainfall parameterization based on the exponential raindrop size distribution. *J. Hydrol.*, **218 (3-4)**, 101–127. 119

Ulbrich, C., 1983: Natural variations in the analytical form of the raindrop size distribution. *J. Climate Appl. Meteor.*, **22 (10)**, 1764–1775. 8, 9, 62, 119

Ulbrich, C. W., 1985: The effects of drop size distribution truncation on rainfall integral parameters and empirical relations. *J. Climate Appl. Meteor.*, **24 (6)**, 580–590. 44

Ulbrich, C. W., 1992: Effects of drop-size-distribution truncation on computer-simulations of dual-measurement radar methods. *J. Appl. Meteorol.*, **31 (7)**, 689–699. 44

Ulbrich, C. W., 1999: Radar properties of tropical rain found from disdrometer data at Arecibo, Puerto Rico. *The 29th Conference on Radar Meteorology*, Amer. Meteor. Soc., P4.15. 20

Van Dijk, A. I. J. M., A. G. C. A. Meesters, J. Schellekens, and L. A. Bruijnzeel, 2005: A two-parameter exponential rainfall depth-intensity distribution applied to runoff and erosion modelling. *J. Hydrol.*, **300**, 155–171. 119

Vié, B., O. Nuissier, and D. V., 2011: Cloud-resolving ensemble simulations of heavy precipitating events : uncertainty on initial conditions and lateral boundary conditions. *Mon. Wea. Rev.*, **139**, 403–423. 96

Vincendon, B., V. Ducrocq, O. Nuissier, and B. Vié, 2011: Perturbation of convection-permitting NWP forecasts for flash-flood ensemble forecasting. *Nat. Hazards Earth Syst. Sci.*, **11**, 1529–1544. 92, 108

Wakimoto, R. M. and V. N. Bringi, 1988: Dual-polarization observations of microbursts associated with intense convection: The 20 july storm during mist project. *Mon. Wea. Rev.*, **116**, 1521–1539. 27

Waldvogel, A., 1974: The No jump of raindrop spectra. *J. Atmos. Sci.*, **31**, 1067–1078. 8, 11, 20

Waldvogel, A., W. Henrich, and L. Mosimann, 1993: New insight into the coupling between snow spectra and raindrop size distributions. *26th Int. Conference on Radar Meteorology, Norman, OK, Am.*, Meteorolo. Soc., 602–604. 11

Willis, P. T., 1984: Functional fits to some observed drop size distributions and parameterization of rain. *J. Atmos. Sci.*, **41**, 1648–1661. 9, 11

Willis, P. T. and P. Tattelman, 1989: Drop-size distributions associated with intense rainfall. *J. Appl. Meteorol.*, **28 (1)**, 3–15. 11

Yuter, S. E., D. E. Kingsmill, L. B. Nance, and M. Loeffler Mang, 2006: Observations of precipitation size and fall speed characteristics within coexisting rain and wet snow. *J. Appl. Meteor. Climatol.*, **45 (10)**, 1450–1464. 23

Zawadzki, I. and M. De Agostinho Antonio, 1988: Equilibrium raindrop size distributions in tropical rain. *J. Atmos. Sci.*, **45**, 3452–3459. 18

Zhang, G. F., J. Vivekanandan, E. A. Brandes, R. Meneghini, and T. Kozu, 2003: The shape-slope relation in observed gamma raindrop size distributions: Statistical error or useful information? *J. Atmos. Oceanic Technol.*, **20 (8)**, 1106–1119. 9